Numerical modeling of exhumation-induced grain-boundary opening in quartz grain aggregates

Dissertation zur Erlangung des Doktorgrades an der Fakultät für Geowissenschaften der Ludwig-Maximilians-Universität München

vorgelegt von

Elnaz Raghami

München, 10.02.2021

Betreuer:	Prof. Dr. Wolfgang W. Schmahl
1. Gutachter:	Prof. Dr. Wolfgang W. Schmahl
2. Gutachter:	Dr. Christoph Schrank (externer Gutachter)

Tag der mündlichen Prüfung: 26.05.2021

To my beloved husband Pedram,

who has always been there for me

with his unconditional love and support

Abstract

Exhumation of rocks and corresponding temperature and pressure changes result in heterogeneous contact interactions at the grain-scale due to anisotropic volume expansion/reduction of adjacent minerals with different thermoelastic properties. The resulting heterogeneous contact interactions give rise thermal-elastic internal stresses at the grain-scale, which in turn produce primarily micro-cracks along grain and phase boundaries. Crucial characteristics of thermal-stress microcracks are their effect on the physical properties of rocks and their development in response to stress and temperature, which provide information about the thermal and deformation history of rocks.

In this study, I employed contact mechanics combined with the finite-element method to simulate the quartz grain-boundary openings in 3D, during exhumation of quartzite accompanied by cooling from 300 ° to 25 °C, and decompression from 300 to 22 MPa. To solve all 3D numerical simulations, Abaqus Standard (Hibbitt, Karlsson and Sorensen Inc.©, 2009) as a finite-element analyzer is used. Model grains have anisotropic linear-elastic rheology as well as thermal expansion tensor. Grain boundaries are simulated as contact surfaces, where their damage evolutions are modeled with a Mohr-Coulomb rheology in shear and two alternative elastoplastic damage approaches in tension: stress-displacement approach and fracture-energy criterion. Accordingly, the following fundamental research problems and questions are addressed:

1) After which typical temperature and pressure decreases do grain-boundary cracks begin to form?
2) How do grain-boundary openings evolve in terms of their geometry (width, length, from vertices over triple lines to grain faces)?
3) How much of the proportion of grain boundaries crack along the exhumation path?
4) How can we best model grain-boundary cracks numerically for 3D anisotropic microfabrics in terms of their grain-boundary mechanical properties?
5) What are the relevant mechanical properties of quartz grain boundaries?
6) How does grain size affect the required differential temperature and pressure for grain-boundary cracking and the proportion of cracked grain boundaries?

Modeling results demonstrate that grain-boundary fractures nucleate at grain vertices and triple grain junction lines, which is consistent with natural and experimental observations. Implementation of stress-displacement approach and a comparison with grain-boundary opening data from natural quartzite indicate that the tensile yield strength (σ_y) of quartz grain boundaries has an upper bound of 75 MPa, with best-fit results for σ_y = 25 MPa in a specific microstructure (i.e. grain sizes ranging from 3 to 5 mm). Moreover, the best-fit model implies that quartz grain-

boundary opening initiates after a temperature and pressure decrease of around 80 °C and 80 MPa and more than 55 % of grain boundaries are open after temperature and pressure drops of 275 °C and 278 MPa, respectively.

However, studying the grain-boundary cracking with stress-displacement approach shows some singularities in the computation of stresses and strains near crack tips and during crack growth owing to elastic snapback, which lead to unreliable modeled stresses and strains near these points. This problem is solved by proposing an alternative approach which uses the fracture-energy dissipated during crack opening and relates directly to mode-I fracture toughness (K_{IC}). Proposing the fracture-energy criterion is successful to estimate ranges of yield strength and fracture-energy relevant to the quartz grain boundaries with grain sizes comparable to natural quartzite samples (i.e. ca. 200 to 600 μm). The yield strength of quartz grain boundaries in the studied example varies between ca. 10 to 15 MPa, fracture-energy and fracture toughness range from ca. 0.3 to 0.9 Jm^{-2} and 0.24 to 0.45 MPa $m^{0.5}$.

In addition to the above-mentioned findings, investigation of the geometric effect of eight different average grain sizes (μm): [10, 36, 100, 361, 1000, 1500, 2500, 3619] on the grain-boundary fracturing reveal that yield strength of grain boundaries is inversely related to the average grain size with an exponent between 0.5 to 1. Besides, the temperature and pressure differentials of cracking strongly decrease non-linearly up to a grain size of 1.5 mm and then remain constant. A larger average grain size compared to a smaller one leads to larger tensile stresses in the model and thus a higher proportion of cracked grain boundaries as well as wider open cracks.

The framework developed can be further used to analyze the impact of exhumation of rocks other than quartzite because nearly all rock-forming minerals, depending on mineral composition and cooling- decompression history, also exhibit open grain and phase boundaries. Moreover, the knowledge of microcracks formation during exhumation would clearly be of value in development of a reliable strategy for many engineering applications such as the resource extraction (e.g. mining, quarrying and drilling), nuclear waste disposal, and reservoir stimulation.

Zusammenfassung

Die Exhumierung von Gesteinen und entsprechende Temperatur- und Druckänderungen führen aufgrund der anisotropen Volumenexpansion / -reduktion benachbarter Mineralien mit unterschiedlichen thermoelastischen Eigenschaften zu heterogenen Kontaktwechselwirkungen im Kornmaßstab. Diese führen zu thermisch-elastischen inneren Spannungen im Kornmaßstab, die wiederum hauptsächlich Mikrorisse entlang der Korn- und Phasengrenzen erzeugen. Entscheidende Eigenschaften von Mikrorissen mit thermischer Beanspruchung sind ihre Auswirkung auf die physikalischen Eigenschaften von Gesteinen und ihre Entwicklung als Reaktion auf Beanspruchung und Temperatur, die Informationen über die Wärme- und Verformungsgeschichte von Gesteinen liefern.

In dieser Studie verwendete ich Kontaktmechanik in Kombination mit der Finite-Elemente-Methode, um die Quarzkorngrenzenöffnungen in 3D während der Exhumierung von Quarzit bei gleichzeitiger Abkühlung von 300 auf 25 °C und Dekompression von 300 auf 22 MPa zu simulieren. Zur Lösung aller numerischen 3D-Simulationen wird Abaqus Standard (Hibbitt, Karlsson und Sorensen Inc. ©, 2009) als Finite-Elemente-Analysator verwendet. Modellkörner haben eine anisotrope linear-elastische Rheologie sowie einen Wärmeausdehnungstensor. Korngrenzen werden als Kontaktflächen simuliert, wobei ihre Schadensentwicklungen mit einer Mohr-Coulomb-Rheologie in Scherung und zwei alternativen elastoplastischen Schadensansätzen unter Spannung modelliert werden: Spannungs-Verschiebungs-Ansatz und Bruchenergie-Kriterium. Dementsprechend werden folgende grundlegende Forschungsprobleme und -fragen angesprochen:

1) Nach welcher typischen Temperatur- und Druckabnahme beginnen sich Korngrenzenrisse zu bilden?
2) Wie entwickeln sich Korngrenzenöffnungen in Bezug auf ihre Geometrie (Breite, Länge, von Eckpunkten über Dreifachlinien zu Kornflächen)?
3) Wie groß ist der Anteil der Korngrenzen, die entlang der Exhumierung wegknacken?
4) Wie können wir Korngrenzenrisse für anisotrope 3D-Mikrofabriken hinsichtlich ihrer mechanischen Eigenschaften an den Korngrenzen am besten numerisch modellieren?
5) Was sind die relevanten mechanischen Eigenschaften von Quarzkorngrenzen?
6) Wie wirkt sich die Korngröße auf die erforderliche Differenztemperatur und den Druck für das Reißen der Korngrenzen und den Anteil der gerissenen Korngrenzen aus?

Die Modellierungsergebnisse zeigen, dass Korngrenzenbrüche an Kornscheitelpunkten und Dreifachkornübergangslinien entstehen, was mit natürlichen und experimentellen Beobachtungen übereinstimmt. Die Implementierung des Spannungs-Verschiebungs-Ansatzes und ein Vergleich

mit Korngrenzenöffnungsdaten aus natürlichem Quarzit zeigen, dass die Streckgrenze (σ_y) der Quarzkorngrenzen eine Obergrenze von 75 MPa aufweist, wobei die besten Anpassungsergebnisse für σ_y = 25 MPa für eine spezifische Mikrostruktur (d.h. Korngrößen im Bereich von 3 bis 5 mm) vorliegen. Darüber hinaus impliziert das Best-Fit-Modell, dass die Öffnung der Quarzkorngrenzen nach einem Temperatur- und Druckabfall von etwa 80 °C und 80 MPa beginnt, und mehr als 55% der Korngrenzen nach Temperatur- und Druckabfällen von 275 °C und 278 MPa offen sind.

Die Untersuchung der Korngrenzenrisse mit dem Spannungsverschiebungsansatz zeigt jedoch einige Singularitäten bei der Berechnung von Spannungen und Dehnungen in der Nähe von Rissspitzen und während des Risswachstums aufgrund von elastischem Snapback, was zu unzuverlässigen modellierten Spannungen und Dehnungen in der Nähe dieser Punkte führt. Dieses Problem wird gelöst, indem ein alternativer Ansatz vorgeschlagen wird, der die beim Öffnen des Risses verbrauchte Bruchenergie verwendet und sich direkt auf die Modenbruchzähigkeit (K_{IC}) bezieht. Das Vorschlagen des Bruchenergiekriteriums ist erfolgreich, um Bereiche der Streckgrenze und Bruchenergie abzuschätzen, die für die Quarzkorngrenzen relevant sind, mit Korngrößen, die mit natürlichen Quarzitproben vergleichbar sind (d.h. ca. 200 bis 600 μm). Die Streckgrenze der Quarzkorngrenzen im untersuchten Beispiel variiert zwischen ca. 10 bis 15 MPa, Bruchenergie und Bruchzähigkeit reichen von ca. 0.3 bis 0.9 Jm^{-2} bzw. 0.24 bis 0.45 MPa $m^{0.5}$.

Zusätzlich zu den oben genannten Befunden zeigt die Untersuchung des geometrischen Effekts von acht verschiedenen durchschnittlichen Korngrößen (μm): [10, 36, 100, 361, 1000, 1500, 2500, 3619] auf den Korngrenzenbruch, dass die Streckgrenze der Korngrenzen mit zunehmender durchschnittlicher Korngröße fällt, mit einer Potenz zwischen -0.5 und -1. Außerdem nehmen die Temperatur- und Druckunterschiede beim Aufbrechen der Korngrenze nichtlinear bis zu einer Korngröße von 1.5 mm stark ab und bleiben dann konstant. Eine größere durchschnittliche Korngröße im Vergleich zu einer kleineren führt zu größeren Zugspannungen im Modell und damit zu einem höheren Anteil an gerissenen Korngrenzen sowie zu breiteren offenen Rissen.

Das entwickelte Gerüst kann weiter verwendet werden, um die Auswirkungen der Exhumierung anderer Gesteine als Quarzit zu analysieren, da nahezu alle Gesteine, abhängig von der Mineralzusammensetzung und der Geschichte der Abkühlung und Dekompression, auch offene Korn- und Phasengrenzen aufweisen. Darüber hinaus wäre das Wissen über die Bildung von Mikrorissen während der Exhumierung eindeutig von großem Wert für die Entwicklung einer zuverlässigen Strategie für viele technische Anwendungen wie die Rohstoffgewinnung (z. B. Bergbau, Steinbruch und Bohrungen), die Entsorgung nuklearer Abfälle und die Stimulation von Lagerstätten.

Table of Contents

Page

Chapter 1

Introduction

1.1 Research Background and previous studies

In this thesis, I employ mathematical 3D grain-scale models to examine grain-boundary cracking during the exhumation of quarzitic rock. Almost all rocks exposed at the surface of Earth have been exhumed from some depth within the lithosphere (Bruner, 1984). During this process, they undergo cooling and hence thermal contraction but also coeval depressurization, leading to the competing process of elastic expansion. It has been recognized more than four decades ago (Bruner, 1984; Heard and Page, 1982; Nur and Simmons, 1970; Rosenfeld et al., 1961; Walsh, 1973) that typical crustal rocks most likely form abundant thermal-elastic micro-cracks during exhumation. This is because rocks are generally composed of mineral grains with different and/or anisotropic thermal expansion as well as elastic properties (Bass, 1995; Skinner, 1966). Therefore, when rocks are subjected to temperature changes and/or external stress changes, the differences in thermal-expansion coefficients and elastic moduli across grain interfaces produce a geometric mismatch between adjacent grains and thus cause heterogeneous contact stresses (Fredrich and Wong, 1986; Johnson et al., 1978; Kranz, 1983). These thermal-elastic contact stresses can lead to the growth of microcracks (Heard and Page, 1982; Nasseri et al., 2007, 2009a, 2009b; Richter and Simmons, 1974; Schrank et al., 2012). At the tectonic scale, thermal-elastic stresses can also matter because the lithosphere consists of layers with differing thermal-elastic properties and temperature and stress gradients across and along the lithosphere can be large. Indeed, thermal-elastic stress has a significant impact on the state of stress in the lithosphere (Bruner, 1979, 1984; Haxby and Turcotte, 1976; Korenaga, 2007; Turcotte and Oxburgh, 1976). This thesis focuses on grain-scale, so-called “internal” thermal-elastic stresses and their potential to induce fractures along the interfaces of thermal-elastically mismatched grain neighbours.

Experimental studies have revealed that thermal-elastic internal stresses induced by cooling or heating of rocks primarily produce microcracks along grain and phase boundaries because grain interfaces are the predominant loci of stress concentrations and often mechanically weaker than the solid grains (Fredrich and Wong, 1986; Simmons and Richter, 1976). Secondary fracturing is observed between cleavage planes or along pre-existing pores and cracks (Brace et al., 1972; Bombolakis, 1973; Kranz, 1979; Heard and Page, 1982; Nasseri et al., 2007, 2009a, 2009b; Richter and Simmons, 1974; Schrank et al., 2012; Tapponier and Brace, 1976). A crucial characteristic of thermal-stress microcracks is their effect on the rheological and petrophysical properties of rocks. They can increase porosity and thus permeability (Giger et al., 2007; Hamdi

et al., 2015; Houseknecht, 1984; Kruhl et al., 2013; Nasseri et al., 2009b; Pimienta et al., 2018), elasticity (Darling et al., 2013; Fan et al., 2017; Nasseri et al., 2007; Rong et al., 2018), and decrease thermal conductivity (Watkins et al., 2012; Pimienta et al., 2018) as well as elastic wave velocities (Fan et al., 2017, 2018; Nasseri et al., 2007; Weng et al., 2019), fracture toughness and strength (Feng et al., 2019; Nasseri et al., 2009a, 2009b; Nasseri and Mohanty, 2008; Nicksiar and Martin, 2014; Wu et al., 2019). Moreover, these microcracks along grain and phase boundaries develop in response to stress and temperature and therefore provide information about the thermal and deformation history of rocks (Vernon, 2004, p. 295).

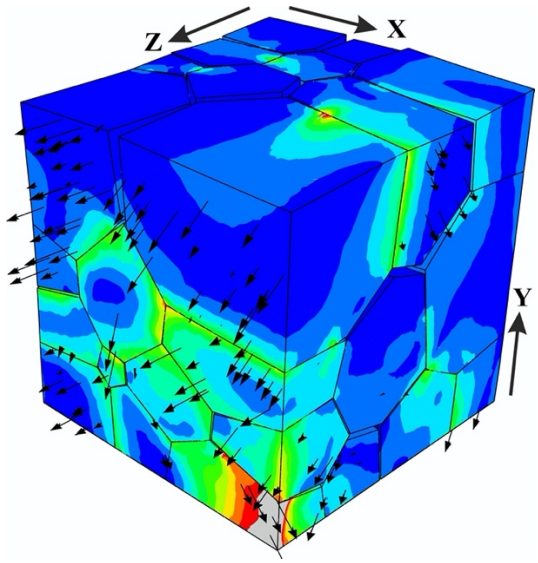

Figure 1.1 Contoured color plots of von Mises stress (MPa) after cooling from 300 to 25 °C and decompression from 300 to 22 MPa. Blue contours indicate low values of von Mises stress and red ones show the high values. The black arrows denote the *c*-axis orientation relative to each grain. This model exhibits open grain boundaries extending across three grain faces with lower values of von Mises stress (blue colors).

Our understanding of thermal-elastic micro-cracks stems from three main sources: micro- and nano-structural investigations of natural rocks (e.g. Brace, 1972; Behrmann, 1985; Bruner, 1984; Hiraga et al., 1999; Kruhl et al., 2013; White and White, 1981; Wirth et al., 2020), rock-mechanical laboratory experiments (e.g. Fredrich and Wong, 1986; Griffith et al., 2018; Johnson et al., 1978; Meredith et al., 2001; Wang et al., 1989), and mathematical modeling (e.g. Li et al., 2019; Tang et al., 2016; Schrank et al., 2012; Yu et al., 2015). Micro- and nano- structural analysis of natural rocks provides invaluable insight into the geometry (length, width), spatial distribution and context (density, spacing, connectivity, crack proportion, phases with most micro-cracks, etc.), mode of propagation (extension and shear), and relative timing of micro-cracks (e.g. Brace, 1972; Behrmann, 1985; Bruner, 1984; Hiraga et al., 1999; Kruhl et al., 2013; White and White, 1981; Wirth et al., 2020). For example, transmission electron microscopy (TEM) measurements of natural samples from various conditions of metamorphism exhibit voids along grain and phase boundaries and commonly at triple-point junctions (Behrmann, 1985; Bons et al., 1990; Hiraga

et al., 1999, 2001; Mancktelow and Pennacchioni, 2004; Shewmon and Anderson, 1998; White and White, 1981). More recent TEM measurements, based on Focused Ion beam (FIB) prepared samples of quartzite, demonstrated that a large number of grain and phase boundaries are partially or totally open with crack widths of up to several hundred nanometers, and that these cracks may form a connected network of open grain and phase boundaries, which allows pervasive fluid flows (Kruhl et al., 2013, Wirth et al., 2020). Based on correlations between grain sizes and widths of open boundaries, Kruhl et al. (2013) proposed that the opening is produced by a combination of anisotropic cooling contraction and of decompression expansion below ca. 300 °C, a temperature that is nearly equivalent to the recrystallization temperature of quartz (Stipp et al., 2002; Stöckhert et al., 1999; Voll, 1976), and below where dislocation creep is negligible while brittle deformation dominates ("brittle-ductile transition"; Nicolas and Poirier, 1976). About four decades Bruner (1979; 1984), who modeled fracturing induced during the cooling and stress relaxation associated with unroofing of rocks, suggested that crack growth results from internal stresses produce due to anisotropic thermal expansion of minerals. However, as always, real rock specimens give a static picture of potentially complex, polyphase geological processes. It is often difficult or even impossible to determine which driving forces led to micro-crack formation, how micro-cracks evolved geometrically through time, and under which pressure and temperature conditions they formed.

Laboratory experiments on natural rocks allow us to analyze how pressure-temperature conditions affect micro-crack formation and how they affect mechanical and transport properties. The outcome of these laboratory analyses illustrates that an enhancement in the microcrack intensity decreases elastic wave speeds, stiffness, yield strength, thermal conductivity (Durham and Abey, 1981; Hamdi et al., 2015; Jin et al., 2019; Rosengren and Jaeger, 1968; Sayers and Kachanov, 1995; Zimmerman, 1985) and increases porosity and permeability (Hamdi et al., 2015; Johnson et al., 1978; Simmons and Cooper, 1978). However, typical rock mechanics set-ups provide no direct observation of microcrack and are limited to post-mortem microstructural studies or the use of proxies such as measurements of acoustic emissions (Baud et al., 2004; Hall et al., 2006; Hall and Bodnar, 1989; Jansen et al., 1993; Nasseri et al., 2006; Stanchits et al., 2006; Thompson et al., 2009). In recent years, 3D micro-tomography has emerged as a useful tool for the in-situ monitoring of growing cracks (Desrues and Viggiani, 2004; Fusseis et al., 2012; Schrank et al., 2012). This method also encounters some limitations. The detectability of cracks with widths in the nm-range and the onset of cracking is difficult or impossible because the spatial resolution is limited to $\geq$ 1 µm. Additionally, the temporal resolution is restricted to tens of seconds. Hence, cracks may grow too quickly to detect their propagation. Further drawback of the experimental examinations is their inability to evaluate the temperature interval for the crack initiation during cooling-induced cracking in spite of extensive cooling and/or depressurization tests (Fan et al., 2018; Isaka et al., 2018; Jin et al., 2019; Kumari et al., 2017; Wang et al., 1989;

Wu et al., 2019). A main reason is that for studying cooling-induced cracking in the laboratory, samples have to be heated first and then cooled. Therefore, the resulting cracks are from both heating and cooling cycles and the reported temperature for the onset of cracking only considers the heating cycles. Finally, laboratory experiments cannot be conducted at geological time and length scales, and it remains a matter of debate if and how such experiments can be extrapolated to nature (Paterson, 2001). Consequently, the details of crack initiation, growth and propagation are still subject to further work.

Mathematical models provide full insight into the dynamics of micro-cracking processes and can simulate geological time scales easily (Abdelaziz et al., 2018; Kolo et al., 2016; Müller et al., 2018; Tomac and Gutierrez, 2017; Weiss et al., 2003). Recent advancements in computational techniques have made it possible to apply numerical simulation to inspect the microcracking process at the grain scale and to solve rock mechanic problems, which are the scope of the present study. Several numerical techniques have been employed to simulate rock deformation and failure behaviour (Abdelaziz et al., 2018; Bruner, 1984; Becker, 1995; Canova et al., 1992; Gao et al., 2016; Hofmann et al., 2015; Saadat and Taheri, 2019; Schrank et al., 2012). In these studies, rock samples are often under different ranges of confining pressures at constant temperature or experience only temperature changes at specific pressure or heating and compression. Bruner, (1984) simulated microcracking arises from only cooling in models including isotropic-elastic grains with anisotropic thermal expansion. Becker, (1995) considered only the effect of heating on the micro-crack formation. Schrank et al. (2012) placed emphasize on the micro-crack generation during heating and a lithostatic confining pressure. The rest of research examined only the micro-cracking during confining pressure. Owing to the complex microstructure of rocks, these models and techniques mainly focus on crack formation in 2D. Besides, there are few studies, which model microcrack formation in rocks with anisotropic thermal-elastic material properties in 3D (Ghazvinian et al., 2014; Gulizzi et al., 2018; Lan et al., 2013; Li et al., 2017; Ronchin et al., 2013). However, most approaches for the mentioned 2D and 3D models of microcrack simulate uniaxial compression or tensile strain combined with or without heating cycle, and to the best knowledge of the researcher, there is no 3D modeling study focusing on the exhumation-induced microcracking so far. Consequently, there is a need to develop 3D grain-scale models to examine microfracture formation in rocks during exhumation. 3D models allow better understanding of inherently 3D complex microstructural phenomena e.g. the influence of the geometry on the microcracking evolution, and the deformation of the individual grains, etc.

A principal reason for the assessment of exhumation-induced cracking is that almost all rocks available in the Earth's continental crust experienced exhumation process. As already noted by Bruner, (1984), most crustal rock types can be expected to contain a significant amount of thermal-elastically induced micro-cracks, which in turn are predicted to have a large impact on petrophysical rock properties and the state of stress in the shallow crust where all of our

engineering activities take place. Therefore, an understanding of microcrack formation during exhumation would clearly be of value in development of a reliable strategy for many engineering applications such as resource extraction (e.g. mining, quarrying and drilling), nuclear waste disposal, and reservoir stimulation (Heard and Page, 1982; Nasseri et al., 2007; Wang et al., 1981). In the present study, I focus on quartz because it is one of the most abundant rock-forming minerals in the Earth's continental crust (ca. 12.6 wt %) (Götze, 2018) and, like nearly all rock-forming minerals, exhibits anisotropic thermal and elastic behavior during temperature and pressure gradients. Bruner, (1984) already demonstrated that the thermal-elastic anisotropy of quartz is of the same order as that of many other rock-forming minerals as well as the thermal-elastic mismatch to other phases. Therefore, it can be expected that the general findings of this research have broad applicability for the impact of exhumation on the physical properties of other rock types, including polyphase ones.

1.2 Research problems and questions

The purpose of this study is to examine the grain-boundary cracking of quartzite while travelling along a typical exhumation P-T pathway through the continental crust, from the base of the brittle crust up to the surface. This is achieved with 3D grain-scale numerical modeling. The following main research questions are addressed:

[1] After which typical temperature and pressure decreases do grain-boundary cracks begin to form?

Rationale: As mentioned above, exhumed natural quartzites, and many other crustal rocks, display abundant grain-boundary cracks (Bruner, 1984; Heard and Page, 1982; Nur and Simmons, 1970; Rosenfeld et al., 1961; Walsh, 1973). However, it is not known where along the exhumation path (in terms of P and T) these cracks started to form. Heating experiments on granitic rocks demonstrate that thermal-elastic micro-cracking commonly starts after a $\Delta T \sim 80$ °C. Is this a temperature change that is relevant for the exhumation process?

[2] How do grain-boundary openings evolve in terms of their geometry (width, length, from vertices over triple lines to grain faces)?

Rationale: According to natural observations (Mancktelow and Pennacchioni, 2004) and experiments (Fredrich and Wong, 1986; Isaka et al., 2018; Kumari et al., 2017), grain-boundary cracks occur first at grain vertices and triple junctions. It would be interesting to investigate that how is the geometric evolution of 3D grain-boundary cracks? Is it consistent with natural and experimental observations?

[3] How much of the proportion of grain boundaries crack along the exhumation path?

Rationale: As a first-order approximation, the effect of micro-cracks on rock mechanical and transport properties is related to porosity (i.e., crack proportion relative to solid phase) (Giger et

al., 2007; Hamdi et al., 2015; Houseknecht, 1984; Kruhl et al., 2013; Nasseri et al., 2009b; Pimienta et al., 2018). Therefore, it is interesting to determine how the proportion of cracked grain-boundary evolves along the exhumation path. This quantity can again not be determined from exhumed natural samples or in laboratory experiments. The latter cannot model cooling and decompression of an intact rock, and micro-cracks with widths below micrometers cannot be observed with in-situ monitoring techniques. However, these widths are very common in natural rocks (Kruhl et al., 2013, Wirth et al., 2020).

[4] How can we best model grain-boundary cracks numerically for 3D anisotropic microfabrics in terms of their grain-boundary mechanical properties?

Rationale: Hitherto, there are few studies to model crack initiation and propagation in rocks with anisotropic thermal-elastic material properties in 3D (Ghazvinian et al., 2014; Gulizzi et al., 2018; Lan et al., 2013; Li et al., 2017). In these studies, boundaries are modelled as strain-softening elastoplastic cohesive interfaces with contact mechanics, which separate when subjected to sufficient internal stresses. In spite the cohesive rheology generally simulates the crack growth procedure without difficulty, it indicates convergence problems often at the point where the crack first nucleates due to elastic snap-back instability (Gao and Bower, 2004; Yu et al., 2016). A number of techniques (Gu et al., 2015; Liu and Zheng, 2010; Riks, 1979) were employed to resolve this issue. However, these schemes generally require some effort to implement and thus lead to physically meaningful predictions. Hence, it is crucial to explore a damage model to simulate faithfully the failure behavior of grain boundaries in terms of their mechanical properties.

[5] What are the relevant mechanical properties of quartz grain boundaries?

Rationale: In the context of fracturing in rocks, mechanical properties such as strength, fracture toughness, etc. are key factors, which need to consider in crack growth (Dutler et al., 2018). Lab experiments displayed that these two parameters relate empirically through a linear relationship (Zhang, 2002), which is valid for almost all rocks. However, this relation was made from measuring the mechanical properties of bulk-samples. Is this relation valid for the microscopic yield strength and mode-I fracture toughness of single grain boundaries?

[6] How does grain size affect the required differential temperature and pressure for grain-boundary cracking and the proportion of cracked grain boundaries?

Rationale: Experimental observations on the thermally induced micro-cracks revealed that a higher temperature is required for an aggregate of smaller grain size to attain the critical stress intensity factor necessary for cracking (Cordero et al., 2016; Fredrich and Wong, 1986; Fredrich et al., 1990; Hatzor and Palchik, 1997). Moreover, other experimental studies also indicated that porosity increases when grain size decreases (e.g. Karaka, 2015; Ogolo et al., 2015). However, the effect of grain size on porosity and onset temperature and pressure of cracking at grain-scale cannot be examined specifically for exhumed samples in laboratory experiments. Consequently,

it is interesting to determine how the grain size influence the proportion of cracked grain-boundary and the differential temperature and pressure of crack initiation along the exhumation path.

To achieve these goals, I combine contact mechanics with finite-element method (FEM) to simulate in 3D the grain-boundary fracturing in monophase, thermal-elastically anisotropic quartz resulting from exhumation-related cooling and decompression. The simulated exhumation-related temperature and pressure intervals approximately corresponds to that of quartzite samples from the base of the brittle crust to the surface, as given in Kruhl et al. (2013): Both the temperature and pressure simultaneously decrease from 300 °C (roughly the recrystallization temperature of quartz; Voll, 1976; Stipp et al., 2002) to 25 °C and from 300 MPa to 22 MPa. These pressure and temperature intervals are equivalent to exhumation from a depth of ca. 11 km to about 1 km along a typical continental geothermal gradient of ca. 27 °C km^{-1}. In all models, quartz grains have anisotropic elastic and thermal properties, while their boundaries can fail in tension and shear according to a strain-softening rheology.

1.3 Thesis structure

This dissertation contains three core chapters. The key content of each chapter is briefly described below:

The first of these chapter has been published in the Journal Tectonophysics as article "*3D modeling of the effect of thermal-elastic stress on grain-boundary opening in quartz grain aggregates"*. A displacement-dependent elastoplastic damage rheology is used for grain boundaries to estimate the probable range of the yield strength of quartz grain boundaries as well as the onset temperature and pressure of cracking for a quartzite sample. In addition, the geometric evolution of 3D grain boundary cracks is explored.

The second chapter is currently under review in Journal Computers and Geotechnics as article "*An alternative approach to studying exhumation-induced grain-boundary openings in quartz grain aggregates: 3D modeling"*, with the aim of maintaining greater stability in the numerical simulation and providing better estimation of the parameters investigated in second chapter, the damage rheology is refined by using the fracture-energy criterion (i.e. energy dissipated during cracking) which relates directly to mode-I fracture toughness (K_{IC}), a parameter that can be commonly measured in the laboratory for a wide range of rocks. Then, it is followed by a parametric study of exhumation-induced grain-boundary cracking to examine the impact of the tensile grain-boundary strength and the fracture-energy. Finally, a synthetic microstructure, which resembles a natural quartzite sample is used to invert for ranges of tensile grain-boundary strength and fracture toughness that is in turn are compared to laboratory data.

In the third chapter, the influence of grain size on the quartz grain-boundary crack initiation and evolution is assessed using the numerical approach explored in chapter 3.

The last chapter of this study includes a summary of the findings, concluding remarks, implications of the study and suggestions for further research.

Chapter 2

3D modeling of the effect of thermal-elastic stress on grain-boundary opening in quartz grain aggregates

Published in journal of Tectonophysics: Elnaz Raghami, Christoph Schrank, Jörn H. Kruhl, 2020: 3D modeling of the effect of thermal-elastic stress on grain-boundary opening in quartz grain aggregates. Tectonophysics (2020), 774, pp 228242. DOI: 10.1016/j.tecto.2019.228242.

The underlying research was designed by Elnaz Raghami, Christoph Schrank, Jörn H. Kruhl. Elnaz Raghami performed the numerical modeling at Queensland University of Technology in Australia and wrote the manuscript. She brought it into its final shape, with comments from the coauthors.

2.1 Abstract

During the exhumation of rocks and the associated temperature and pressure decrease, the anisotropic thermoelastic properties of minerals lead to internal stresses on the grain scale, which in turn cause fracturing and opening of grain and phase boundaries. To gain deeper insight into the onset of grain-boundary cracking and the subsequent evolution of grain-boundary fracture networks after crack initiation, 3D grain-scale numerical modeling has been performed. In detail, the fracturing and opening of quartz grain boundaries during exhumation of quartzite with millimetre-scale grains and randomly oriented crystallographic axes, accompanied by cooling from 300 to 25 °C and decompression from 300 to 22 MPa, have been modelled with contact mechanics and the finite-element method. Model grains have an anisotropic linear-elastic rheology and an anisotropic thermal-expansion tensor. Grain boundaries are modelled as contact surfaces with a non-linear strain-softening rheology in tension and a Mohr-Coulomb rheology in shear. Grain-boundary fractures nucleate at grain vertices and triple lines, in agreement with observations in nature and experiment. Comparison with grain- boundary opening data from natural quartzite indicates that the tensile yield strength (σ_y) of quartz grain boundaries has an upper bound of 75 MPa, with best-fit results for σ_y = 25 MPa. Moreover, the best-fit model implies that quartz grain-boundary opening initiates after a temperature and pressure decrease of around 80 °C and 80 MPa.

Keywords: grain boundary**,** tensile yield strength**,** thermal cracking**,** internal stress anisotropic thermoelastic properties

2.2 Introduction

Crystalline solids generally consist of minerals with different and/or anisotropic thermal-expansion and elastic properties (Bass, 1995; Skinner, 1966). Therefore, changes in temperature and pressure lead to heterogeneous contact interactions at the grain-scale, due to differing volume changes of adjacent minerals with different thermoelastic properties, which in turn cause internal stresses (Fredrich and Wong, 1986). Thermal-elastic internal stresses induced by cooling or heating of rocks lead to the growth of microcracks (Heard and Page, 1982; Nasseri et al., 2007, 2009a, 2009b; Richter and Simmons, 1974; Schrank et al., 2012) and have a great impact on the state of stress in the lithosphere (Bruner, 1979, 1984; Haxby and Turcotte, 1976; Korenaga, 2007; Turcotte and Oxburgh, 1976). The opening of micro- cracks driven by internal stresses occurs preferentially at sites of low strength, such as grain and phase boundaries, cleavage planes, or pre-existing pores and cracks. The importance of thermally induced microcracks in rocks has been examined by laboratory deformation experiments and by mathematical modeling. Particular emphasis was dedicated to the related changes of the physical properties of rocks, such as porosity

and permeability (Giger et al., 2007; Hamdi et al., 2015; Houseknecht, 1984; Kruhl et al., 2013; Nasseri et al., 2009b; Pimienta et al., 2018), elasticity (Darling et al., 2013; Fan et al., 2017; Nasseri et al., 2007; Rong et al., 2018), thermal conductivity (Watkins et al., 2012; Pimienta et al., 2018), and strength (shear, compressional, extensional) (Feng et al., 2019; Nasseri et al., 2009a; Nicksiar and Martin, 2014; Wu et al., 2019).

Previous high-resolution TEM investigations on natural samples from various conditions of metamorphism show voids along grain and phase boundaries and preferentially at triple-point junctions (Behrmann, 1985; Bons et al., 1990; Hiraga et al., 1999, 2001; Mancktelow and Pennacchioni, 2004; White and White, 1981). In addition, more recent FIB/TEM-based observations on quartzite reveal that a large number of grain and phase boundaries are partially or to- tally open with crack widths of up to several hundred nanometres (Kruhl et al., 2013). These boundaries form a connected network that generates permeability for fluid transport. Based on correlations be- tween grain sizes and widths of open boundaries, Kruhl et al. (2013) suggest that opening is related to decompression and to cooling below the temperature, at which dislocation creep is negligible and brittle deformation dominates (″brittle-ductile transition″; Nicolas and Poirier, 1976). This temperature is roughly equivalent to the recrystallization temperature of quartz – ca. 300 °C (Stipp et al., 2002; Stöckhert et al., 1999; Voll, 1976). Nevertheless, clear indications of the onset temperature and pressure differentials of grain-boundary opening are still lacking.

Laboratory experiments focused on the effect of microcracks on bulk physical properties of rocks. An increase in microcrack proportion causes decreasing elastic wave speeds, stiffness, yield strength, thermal conductivity (Durham and Abey, 1981; Hamdi et al., 2015; Jin et al., 2019; Rosengren and Jaeger, 1968; Sayers and Kachanov, 1995; Zimmerman, 1985) but higher porosity and permeability (Hamdi et al., 2015; Johnson et al., 1978; Simmons and Cooper, 1978). Properties of the dynamically evolving microcrack network, such as crack geometry, width, extension, orientation, and arrangement within the network, play a major role in these processes. However, typical rock mechanics set-ups do not allow direct observations of microcrack evolution and are restricted to post-mortem microstructural studies or the use of proxies such as measurements of acoustic emissions (Baud et al., 2004; Hall et al., 2006; Hall and Bodnar, 1989; Jansen et al., 1993; Nasseri et al., 2006; Stanchits et al., 2006; Thompson et al., 2009). Over the last two to three decades, 3D micro-tomography has been established as a valuable tool for the in-situ monitoring of growing cracks (Desrues and Viggiani, 2004; Fusseis et al., 2012; Schrank et al., 2012). However, the samples are small, and the spatial resolution is limited to $\geq 1\ \mu m$. This makes the detection of cracks with widths in the nm-range and the onset of cracking difficult if not impossible. Moreover, the temporal resolution is limited to tens of seconds. Hence, cracks may grow too quickly to see their propagation. Therefore, the details of crack initiation, growth and propagation are still subject to further work.

Mathematical forward models of cracking can overcome some of these limitations. Many approaches have been used to model the crack evolution in polycrystalline materials (Abdelaziz et al., 2018; Becker, 1995; Canova et al., 1992; Gao et al., 2016; Gulizzi et al., 2018; Schrank et al., 2012). However, due to the complex microstructure of rocks in 3D and the associated computational burden, most studies only con- sider crack formation in 2D. Only a small number of studies model microcrack formation in rocks with anisotropic thermal-elastic material properties in 3D, with a focus on the establishment of the numerical method (Ghazvinian et al., 2014; Lan et al., 2013; Li et al., 2017; Ronchin et al., 2013). The main objective of this work is to examine a specific physical process: the grain-boundary fracturing in monophase, thermal-elastically anisotropic quartzite induced by exhumation-related cooling and decompression. Specifically, we aim to narrow down the probable range of the poorly constrained tensile yield strength of quartz grain boundaries and thus estimate the required temperature and pressure differential for the onset of cracking. Moreover, our models provide insights into the geometric evolution of 3D grain boundary cracks.

To achieve these goals, we combine contact mechanics with the finite-element method to simulate in 3D the grain-scale thermal-elastic cracking of grain boundaries during the exhumation of pure quartzite with foam structure and random orientation of crystallographic axes over a temperature interval of 275 °C, i.e. from 300 to 25 °C, and pressure interval of ca. 278 MPa, i.e. from 300 to 22 MPa. In all models, quartz grains have anisotropic elastic and thermal properties while their boundaries can fail in tension and shear according to an empirical damage-mechanics model (Schrank et al., 2012) inspired by Morse-type atomic bonding models (Tromans and Meech, 2004). We only focus on quartz in this study, although nearly all rock-forming minerals also exhibit thermal and elastic anisotropy (Bass, 1995; Fei, 1995). There- fore, it can be expected that our general findings have broad applicability for the impact of exhumation on the physical properties of other rock types.

2.3 3D modeling of exhumation-induced grain-boundary opening: methods

In all of our 3D numerical simulations, we employ a foam micro-structure for a centimetric model cube composed of pure quartzite (Fig. 2.1). The simulated exhumation-related temperature and pressure interval roughly corresponds to that of quartzite samples in Kruhl et al. (2013): The models are cooled linearly from 300 °C (roughly the ″re- crystallization temperature″ of quartz; Voll, 1976; Stipp et al., 2002) to 25 °C while the confining pressure is reduced from 300 MPa to 22 MPa. These pressure and temperature intervals are time-independent and equivalent to exhumation from a depth of ca. 11 km to about 1 km along a typical continental geothermal gradient of ca. 25 °C km^{-1}. It is not necessary to consider rates of cooling and decompression in the model for two reasons. First, the chosen model rheology is time-in- dependent. This choice is

inspired by the notion that quartz does not deform by time-dependent viscoplastic flow under the studied conditions, as discussed further below. Second, the model size is on the order of centimetres. Therefore, the thermal equilibration time scale of the small model cube is much smaller than the cooling time scale in nature. Hence, transient heat transfer is physically irrelevant for the problem at hand.

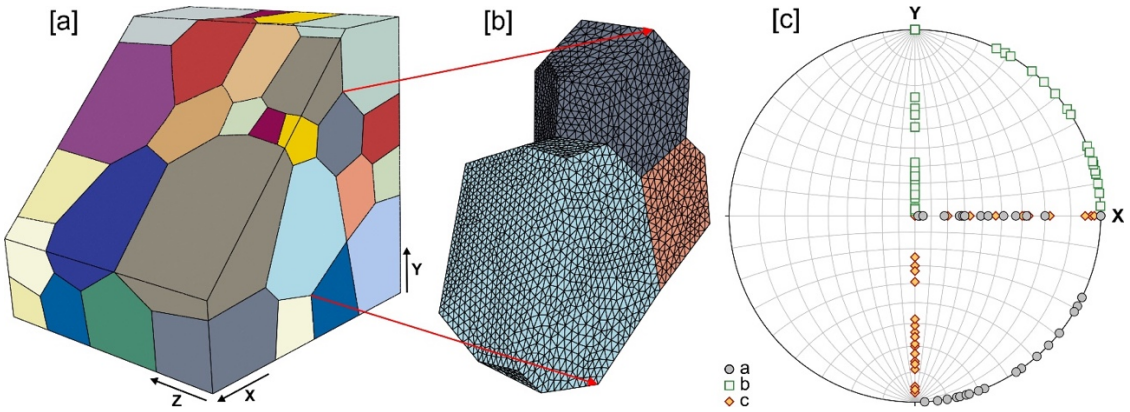

Figure 2.1. (a) Foam microstructure in the 50-grain model with 214 grain boundaries generated in a cubic domain (15 mm-edge length). The YZ-plane is cut obliquely to reveal part of the model interior. All of our models are generated with Neper (Quey et al., 2011). The average grain size ranges from 3 to 5 mm. Colors mark individual grains. (b) Detailed view of three grains with the high-resolution mesh composed of tetrahedral elements. On average, the elements shown here are ca. 15% smaller than those used for the standard models (see text for details). (c) Orientation of model a-, b- and c-axes relative to the XY-plane shown in a Wulff net. This plot was generated with OSXStereonet 2.4 (Cardozo and Allmendinger, 2013).

2.3.1 3D model generation and meshing

For the generation of the foam microstructure, the grain growth morphological approach implemented in Neper is used (Quey et al., 2011). From a physical point of view, this approach corresponds to a process of crystallization where grains nucleate from randomly distributed points at the same time and grow isotropically at the same rate. The resulting 3D grains have polyhedral shapes with straight triple lines, flat grain boundaries and high sphericities (Fig. 2.1a), similar enough to the microstructure of natural quartzite. The assumed domain boundary in all models is a cube with 15 mm edge length. The model cube contains 50 discrete deformable grains, resulting in an average grain diameter approximately between 3 to 5 mm. This model contains a total of 214 grain boundaries. To create an approximately random crystallographic orientation, the crystallographic axes of each grain are rotated relative to the global Cartesian coordinate system XYZ (Fig. 2.1a) in the following way: first, one of the three coordinate axes is chosen randomly as rotation axis; second, the crystallographic axes are rotated around this given rotation axis by an angle chosen randomly from the interval [0; 90]° (Fig. 2.1c). The standard models contain 823,996 4-node linear displacement and temperature tetrahedral elements (C3D4T) (Fig. 2.1b).

The mean size of the mesh elements is defined as 10 % of the average grain size. Mesh density is approximately constant within the grains and grain boundaries. Characteristic element length

is ca. 423 μm. In our high-resolution model, 1,611,594 elements are used with a characteristic size of ca. 358 μm. Each grain boundary in the finite element (FE) mesh acts as a contact surface with an initial separation distance of zero. Each set of neighbouring grain boundaries has the same number of nodes occupying the same position at the beginning of the experiment.

2.3.2 Governing equations

To solve the governing equations, Abaqus Standard is used (Hibbitt, Karlsson and Sorensen Inc.©, 2009). This finite-element analyser is a Lagrangian code, which employs an implicit integration scheme with adaptive time stepping. Problems with simultaneous temperature and displacement fields are solved by coupled temperature-displacement analysis and the large-displacement formulation, which has additive strain-rate decomposition and uses Jaumann's stress rate (Jaumann, 1911). Conservation of energy (Eq. (1)) is given by (Regenauer-Lieb and Yuen, 2003):

$$\rho c_p \frac{DT}{Dt} - \nabla(k\nabla T) = 0, \quad (1)$$

where ρ is density; c_p is specific heat capacity; T is temperature; $\frac{D(.)}{D(.)}$ is the material derivative; t is time; and k is thermal conductivity. The conservation of mass for any deformable solid is:

$$\frac{D\rho}{Dt} + \rho\nabla v = 0, \quad (2)$$

with v denoting the velocity vector. Inertia terms are neglected in Eq. (2). Hence, the conservation of linear momentum in terms of Cauchy stress tensor $\boldsymbol{\sigma}$ and body force vector f is:

$$\nabla . \boldsymbol{\sigma} + \rho \mathrm{f} = 0, \quad (3)$$

To have the conservation of angular momentum for a continuum, the Cauchy stress must be a symmetric tensor in Eq. (3).

2.3.3 Rheological properties

Grains

Since we consider a temperature interval below the recrystallization temperature for quartz (i.e., for α-quartz), intracrystalline plasticity is neglected, based on the assumption that crystal-plastic deformation by motion of dislocations or vacancies is ineffective at temperatures below 300 °C in quartz (e.g. Stöckhert et al., 1999). The model grains have a fully anisotropic linear-elastic rheology. The general form of Hooke's law, for thermoelastic solid materials is (Wang et al., 2018):

$$\boldsymbol{\sigma} = \boldsymbol{C} : \left(\boldsymbol{\varepsilon} - \boldsymbol{\varepsilon}^{\theta}\right), \quad (4)$$

where $\boldsymbol{\sigma}$ is the Cauchy stress tensor, $\boldsymbol{C}$ is the fourth-order stiffness tensor, $\boldsymbol{\varepsilon}$ is the second-order total strain tensor and $\boldsymbol{\varepsilon}^{\theta}$ is the thermal strain defined as:

$$\boldsymbol{\varepsilon}^{\theta}=\boldsymbol{\beta}\,(T-T_0), \tag{5}$$

T_0 is the reference temperature, and $\boldsymbol{\beta}$ is the thermal expansion tensor (Eq. (5)). In the case of trigonal symmetry of quartz, the stiffness tensor in Eq. (4) can be written based on six independent elastic-stiffness coefficients (C_{11}, C_{12}, C_{13}, C_{14}, C_{33}, C_{44}). Since Eq. (4) is a function of both temperature and pressure, thermal expansion and decompression both have an effect on the stress.

Grain boundaries

In all constructed models, grain boundaries are the interfaces be- tween adjacent grains, or crystallites in a polycrystalline material, and they are planar and flat. They are modelled as contact surfaces with identical contact properties and zero separation at the beginning of the experiment. To analyze the contact interactions between a pair of sur- faces, the node-to-surface contact method with a master-slave approach and the small-sliding approximation is used (Hibbitt, Karlsson and Sorensen Inc.©, 2009). In compression, stresses across model grain boundaries are linear-elastic and controlled by the geometry of the interface and the material properties of the contacting grains. In tension and shear, stresses acting on grain boundaries are modelled with an elastoplastic damage rheology where the stress is a function of relative displacement (Fig. 2.2a):

$$\sigma(d)=\begin{cases} d \le d_{crit} \rightarrow \sigma(d)=K_n\,d \\ d > d_{crit} \rightarrow \sigma(d)=\sigma_y(1-D(d)) \end{cases} \tag{6}$$

where σ is tensile/shear traction; σ_y is tensile/shear yield stress; d is extensional/shear displacement perpendicular/parallel to the grain- boundary segment under consideration; K_n is an elastic modulus with unit Pa/m; and D is a damage parameter assuming values between 0 and 1. Below a critical displacement (d_{crit}), the surface behaves linear- elastically (Eq. (6)). If displacement exceeds (d_{crit}), the critical yield stress σ_y is reached, and irreversible grain-boundary damage occurs. With ongoing displacement, tractions on the grain boundary and normal stress decay exponentially (Eq. (7)) to zero until a maximum displacement (d_{max}), beyond which no tensile or shear tractions are transmitted (Fig. 2.2a). At this point, the grain-boundary segment is completely cracked and cohesionless. The exponential decay is modelled via the damage parameter D (Hibbitt, Karlsson and Sorensen Inc.©, 2009):

$$D(d)=1-\frac{d_{crit}}{d}\left(1-\frac{1-\exp\left(\frac{-a(d-d_{crit})}{d_{max}-d_{crit}}\right)}{1-\exp(-a)}\right), \tag{7}$$

where a is a shape parameter. The relevant material parameters are displayed in Table 2.1. The use of this specific grain-boundary rheology is inspired by the tensile stress evolution predicted from Morse-type bonding laws for intact quartz crystals in Tromans and Meech (2004) (Fig. 2.2b).

It is reasonable to assume that the general shape of the stress evolution should be similar across a cohesive grain boundary albeit with significantly lower yield stress. Healing of cracked grain boundaries was not considered. However, if cracked grain boundaries come in contact again at a later stage compressive stresses are transmitted in contraction. If they slide past one another, a static linear isotropic friction model with constant friction coefficient μ and zero cohesion determines the relation between shear and normal stress.

Table 2.1. Quartz grain-boundary properties

σ_y (MPa)	d_{crit} (nm)	d_{max} (nm)	ζ ($Wm^{-2}K^{-4}$)	a	e_A, e_B	K ($JK^{-1}m^{-2}s^{-1}$)	F	K_n ($m^{-1}MPa$)	η
25, 50, 75, 100	0.5	1.5	5.67×10^{-8}	1	0.8	3000	1	5×10^{16}	25, 50, 75, 100

The model rheology of the grain boundaries exhibits strong strain softening and, as a result, the sudden opening of multiple contact sur- faces can lead to convergence problems in the implicit integration due to elastic snap-back (Gao and Bower 2004; Hibbitt, Karlsson and Sorensen Inc.©, 2009; Yu et al., 2016). To solve this problem, viscous regularization is employed (Gao and Bower 2004). This method introduces an arbitrary linear rate dependence in the separation law, which modifies the interface stress through viscous damping. This artificial linear-viscous energy sink stabilizes crack growth and opening. For an insightful discussion on the numerical implementation and effects of viscous regularization, the reader is referred to the work of Gao and Bower (2004) and Yu et al. (2016). We use this method here as implemented in Abaqus Standard (Hibbitt, Karlsson and Sorensen Inc.©, 2009) to improve convergence and study the effect of the damping viscosity coefficient, which is a relaxation time, empirically. For simplicity, this coefficient is referred to as damping viscosity in the following.

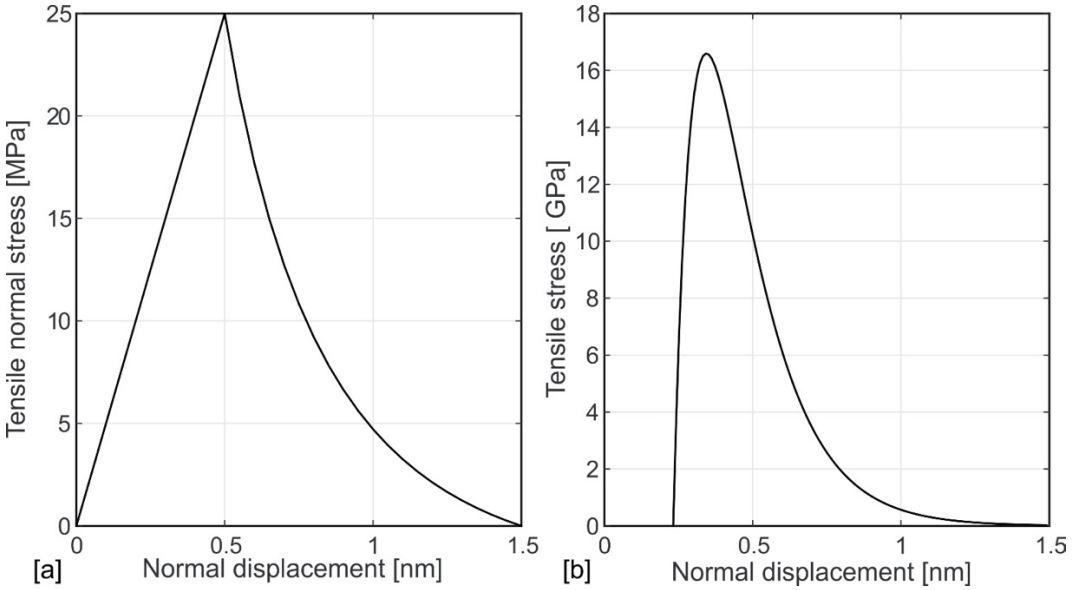

Figure 2.2. (a) Tensile normal stress evolution as function of grain-boundary separation distance for the damage model used in this contribution. The tensile yield stress is 25 MPa. The critical distance for damage

onset is 0.5 nm, and the maximum separation distance over which tensile stress is transmitted is 1.5 nm. (b) Theoretical evolution of tensile stress over average atom spacing in a defect-free cube of isotropic linear-elastic quartz plotted with Eq. (13) and material parameters for α-quartz from Tromans and Meech (2004).

2.3.4 Boundary and initial conditions

Prior to cooling and decompression, the entire model is at a temperature of 300 °C and a compressive mean stress (the average trace of the Cauchy stress, also referred to as pressure) of 300 MPa with closed grain boundaries and zero local differential stresses. These are also the assumed starting conditions for grain boundary opening in quartzites analyzed by Kruhl et al. (2013). To avoid model translation, the three planes making up the Cartesian coordinate system are fixed only in the respective directions perpendicular to each plane: $u_k(k = 0)$, $k = x, y, z$, where u_k denotes displacement in direction k. These are symmetry boundary conditions making the constrained coordinate planes mirror planes of the micro- structure and related stresses and displacements. The remaining three surfaces of the cube are unconstrained in terms of displacement but experience a normal-stress load and temperature load. During the exhumation simulation, temperature decreases linearly from the initial value to its final value of 25 °C at the model surface nodes over the duration of the simulation (ca. 10 °C per time step). Total simulation time is chosen large enough to allow for thermal equilibration of the model cube, which is certainly always the case for the considered length scale and tectonic exhumation time scales. To model decompression, a linearly increasing tensile normal stress is applied to all model surfaces in concert with the temperature load, resulting in a total bulk pressure drop by 278 MPa over the entire cooling interval. Through the chosen loading conditions, grain-boundary cracking is induced by cooling and decompression, driven by the internally mismatching strains that result from thermal-elastic anisotropy in combination with the 3D microstructure. The stress boundary conditions constitute a lower-bound estimate for grain-boundary cracking (Regenauer-Lieb et al., 2014). Alternatively, one could prescribe an arbitrary displacement history at the model boundaries. This procedure would enforce grain-boundary cracking and soon lead to an unphysical disintegration of the model. Moreover, it is difficult to determine a potential displacement history at the length scale modelled here in nature. The choice of stress boundary conditions for the exhumation path (in the absence of tectonic far-field loading) does not only provide conservative, physically meaningful results for cracking but can also be constrained readily in terms of actual loading magnitudes. We tested empirically if the boundary conditions promote crack nucleation at the model surfaces and found that most grain-boundary cracks nucleate in the model interior (see Appendix 2.A, Fig. 2.A1).

2.3.5 Material properties

Grains

We simulate crystalline quartz with anisotropic thermal expansivity with the coefficients α_{11}, $\alpha_{22} = \alpha_{33}$ (Vázquez et al., 2015; Table 2.2) and elastic stiffness (Heyliger et al., 2003; Table 2.2), isotropic temperature-dependent thermal conductivity (Yoon et al., 2004; Fig. 2.3) and specific heat capacity (Connolly, 2005; Fig. 2.3), and constant density ρ (Heyliger et al., 2003; Table 2.2).

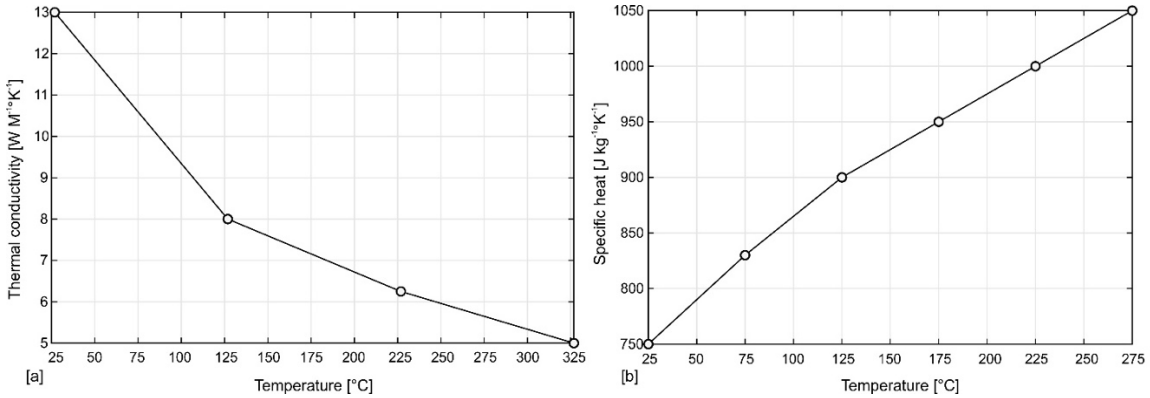

Figure 2.3. Temperature-dependent material properties of crystalline quartz used in the 3D simulations. The solid lines are shown for better visibility of the trend. Moreover, Abaqus employs linear interpolation in between tabulated material-property values. (a) Thermal conductivity (from Yoon et al., 2004). (b) Specific heat data are (from Connolly, 2005).

Table 2.2. Material properties of quartz grains used in 3D models

ρ (kgm $^{-3}$)[a]	α_{11} (°C $^{-1}$)[b]	α_{33} (°C $^{-1}$)[b]	C_{11} (GPa)[a]	C_{12} (GPa)[a]	C_{13} (GPa)[a]	C_{14} (GPa)[a]	C_{33} (GPa)[a]	C_{44} (GPa)[a]
2646.6 ± 0.01	14×10^{-6}	9×10^{-6}	87.16 ± 0.14	6.64 ± 0.10	12.09 ± 0.21	-18.15 ± 0.08	106.00 ± 0.20	58.14 ± 0.08

[a] From Heyliger et al. (2003)
[b] From Vázquez (2015)

Grain boundaries

For simplicity, all grain boundaries have the same contact proper- ties. Modeling tests on the parameter sensitivity of the boundary rheology show that the yield stress σ_y and the damping viscosity η are the main relevant parameters for grain-boundary separation behavior. We chose a value of $d_{crit} = 0.5\ nm$ based on natural measurements of the structural width of intact grain boundaries in a quartzofeldspathic ultramylonite (Hiraga et al., 1999). Small-angle scattering experiments on Volterra alabaster, a fine-grained natural gypsum rock with a foam- like microstructure and porosity < 2 % (Fusseis et al., 2012; Stretton, 1996), demonstrate that the Porod region of this material commences at scattering angles related to scatterers of the characteristic width of ca. 1 nm (Schrank et al., 2019). Since microscopic imaging of this material

confirms that the scatterers in virgin Volterra alabaster are mainly grain-boundary cracks, we use the width of 1.5 nm as maximum separation d_{max} in our damage rheology. Moreover, we found that the model results are essentially insensitive to the choice of d_{max} as long as it remains within physically reasonable bounds.

We also tested if our models are sensitive to the choice of the friction coefficient of the shear response between failed grain boundaries. Again, if these values stay within reasonable bounds, their choice does not affect the model results significantly (see Appendix 2.B, Fig. 2.B1), as also noted for the 2D contact models of grain-boundary cracking by Schrank et al. (2012). Therefore, a friction coefficient value of 0.5 is taken for all 3D models. To approximate the best values of yield stress σ_y and damping viscosity coefficient η for quartzite, for each of the two parameters four values are tested (see chapter 3.1). When grain boundaries are completely cracked, heat flux (q) (Eq. (8)) per unit surface crossing the gap between contact surfaces follows the radiation law (Hibbitt, Karlsson and Sorensen Inc.©, 2009):

$$q = H[(T_A - T_0)^4 - (T_B - T_0)^4], \tag{8}$$

where T_A and T_B denote the temperatures of the adjacent cracked grain surfaces, T0 is the absolute zero on the used temperature scale, and the coefficient H is given by Eq. (9):

$$H = \frac{F\zeta}{\frac{1}{e_A}+\frac{1}{e_B}-1} \tag{9}$$

where ζ is the Stefan-Boltzmann constant, F is the effective view factor, and e_A and e_B are the emissivities of the adjacent grain surfaces. When grain boundaries are closed, the conductive heat transfer between contact surfaces is defined by Fourier's law:

$$q = -K(T_A - T_B), \tag{10}$$

where K is the grain boundary conductance (Eq. (10)). When grain boundaries start to open, K decreases linearly as a function of normal distance between adjacent grain boundaries and assumes that the value of K drops to zero after 1.0×10^{-6} m. The values of all grain-boundary material parameters are summarized in Table 2.1.

2.4 Results

The result section is structured as follows. First, we present a parametric study of the effects of the two most important modeling parameters: the yield stress σ_y and damping viscosity η. Second, the effect of mesh size is investigated. Third, we present observations of grain-boundary fracture onset and propagation. Fourth, the relative importance of temperature and pressure gradient for crack evolution is elucidated.

2.4.1 Parametric study of the effect of yield stress and damping viscosity

The following parameter ranges are examined: σ_y (MPa) = η = [25; 50; 75; 100]. In all models, the total thermal gradient is ΔT = 275 °C and the total pressure gradient is ΔP=278MPa. The results for σ_y = 100 MPa are omitted because the first cracking of a single grain boundary only begins in the last time step. In other words, our models do not exhibit grain-boundary cracking at this yield stress. The evolution of crack width and the proportion of open grain boundaries are presented in Fig. 2.4. At σ_y = 25 MPa, the onset of cracking appears after ΔT (°C) = 80 ≅ ΔP (MPa) regardless of η (Fig. 2.4a). For all η, there is a non-linear increase in grain-boundary crack width beyond the onset of cracking. An increase in η results in a non-linear decrease of the final grain-boundary crack width ranging from 21 μm at η = 25 to 0.5 μm at η = 100. The sensitivity of the proportion of cracked boundaries to the choice of η is similar to that of grain-boundary crack width (Fig. 2.4b). An increase in η causes a non-linear reduction in the proportion of cracked grain boundaries ranging from 99 % at η =25 to 55 % at η =100.

For σ_y= 50MPa, the onset of cracking occurs after ΔT (°C) = 140 ≅ ΔP (MPa) regardless of η (Fig. 2.4c). A non-linear increase in grain-boundary crack width after the onset of cracking is observed for all η. An increase in η leads to a non-linear decrease of final grain- boundary crack width ranging from 0.6 μm at η = 25 to 0.2 μm at η = 100. The proportion of cracked grain boundaries shows similar sensitivity to the choice of η (Fig. 2.4d). An increase in η gives a non-linear drop in the proportion of cracked grain boundaries from 14 % at η=25 to 3 % at η=100.

Regarding the yield stress σ_y = 75 MPa, grain-boundary cracking begins after ΔT (°C) = 220 ≅ ΔP (MPa) regardless of η (Fig. 2.4e). For all η, grain-boundary crack width beyond the onset of cracking rises non- linearly. An increase in η results in a non-linear decrease of grain- boundary crack width ranging from 0.2 μm at η = 25 to 0.15 μm at η = 100. The proportion of cracked boundaries indicates similar behavior to the choice of η (Fig. 2.4f). High η causes a smaller proportion of open grain boundaries. The range of cracked grain boundaries is from 0.22 % at η=25 to 0.07 % at η=100. In summary, an increase in yield stress results in a delay in the onset of cracking and a decrease of final grain-boundary crack width as well as the proportion of open boundaries. An increase in damping viscosity has no impact on the onset of cracking but hampers crack opening and decreases the pro- portion of open boundaries.

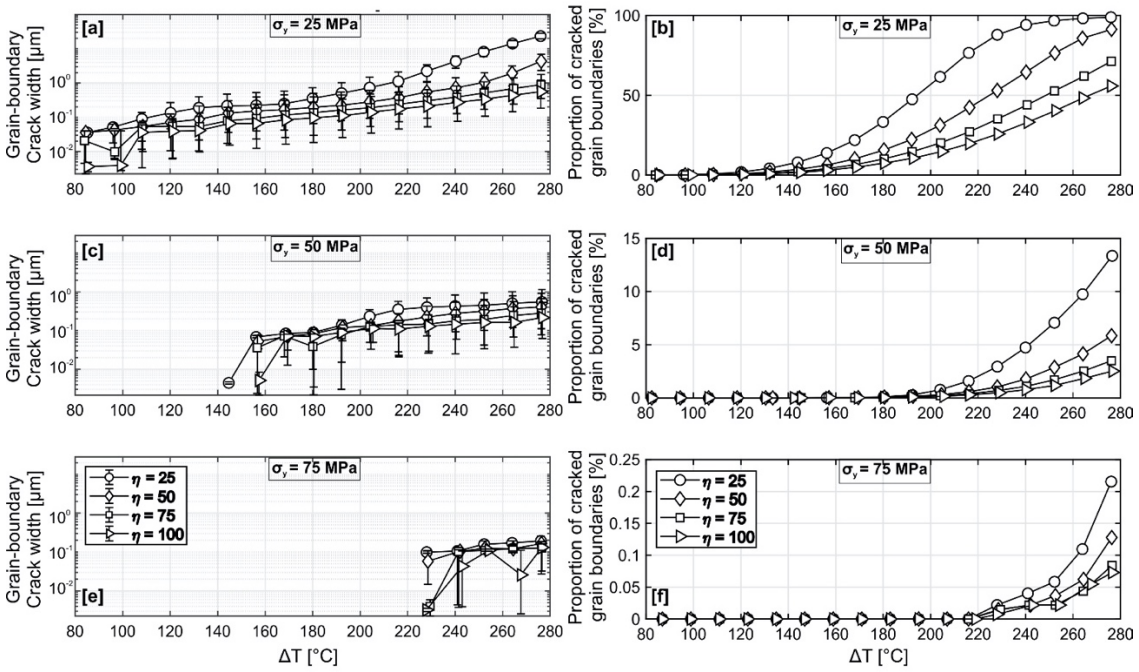

Figure 2.4. 3D modeling results of the effect of damping viscosity (η) on quartz grain boundaries with σ_y= 25, 50 and 75 MPa over ΔT= 275˚C and ΔP= 278 MPa. In all cases, 50-grain models with average grain size ranging from 3 to 5 mm and 214 grain boundaries are used. Left column: Evolution of the median of grain-boundary crack width and onset temperature and pressure of cracking for (a) σ_y= 25 MPa (c) σ_y= 50 MPa (e) σ_y= 75 MPa. In all cases, error bars indicate the 25- and 75-percentiles of the crack-width frequency distribution computed for all nodes on the contact surfaces making up grain boundaries. A grain-boundary node is considered as completely cracked once its displacement normal to the boundary is ≥ 1.5 nm. Right column: Evolution of the proportion of open grain boundaries for (b) σ_y= 25 MPa (d) σ_y= 50 MPa (f) σ_y= 75 MPa.

2.4.2 The effect of mesh size

The effect of mesh size on a 50-grain model with σ_y = 25 MPa and η = 100 with a total thermal and pressure gradient of ΔT = 275 °C and ΔP = 278 MPa is represented in Fig. 2.5. Contour plots (Figs. 5a-b) indicate the local contact pressure resulting from mesh discretization at contact surfaces at the onset of opening. The coarse model (characteristic element length of ca. 423 μm) shows a larger spatial variation in local contact pressure than the fine model (characteristic element length of ca. 358 μm). It ranges from –24 to 56 MPa for the model with coarse mesh and –18 to 44 MPa for the model with fine mesh. Maximum contact pressures occur at vertex points and triple lines in both models, indicating that grain-boundary cracking nucleates at these locations preferentially. In the coarse model, regions of high contact pressure at the triple lines show much smaller spatial gradients than in the fine model, which in turn promotes cracking as seen in the evolution of crack width and proportion of open boundaries (Figs. 2.5c-d). This effect is minor in the final crack-width statistics (Fig. 2.5c) but the pro- portion of open grain boundaries shows a more significant variation for differing the mesh size. The fine model exhibits a smaller

proportion of cracked boundaries at the end, around 45 %, 10 % lower than the coarse model (Fig. 2.5d).

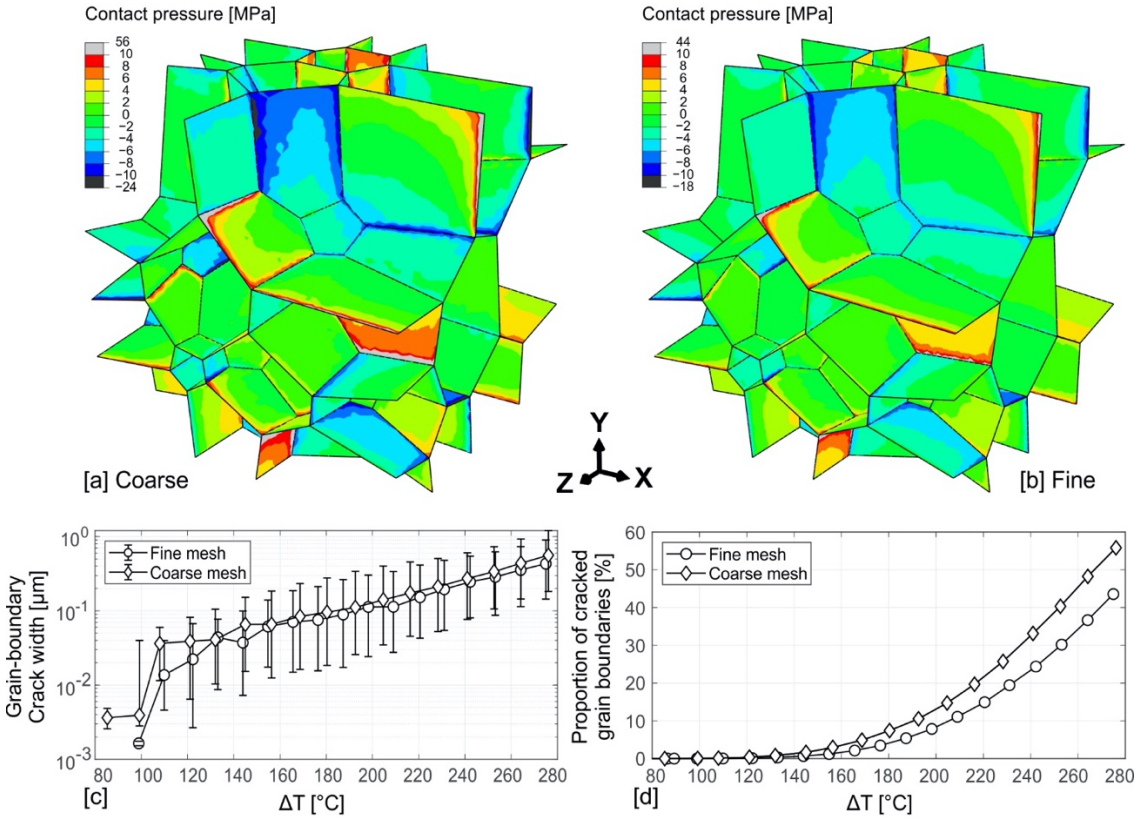

Figure 2.5. (a) and (b) Logarithmic contoured color plots of contact pressure (MPa) for coarsely and finely meshed models with σ_y = 25 MPa and η = 100 at the onset of cracking (ΔT (˚C) = 80 ≅ ΔP (MPa)). The coarse mesh results in an overestimation of pressure near the grain boundaries, which in turn promotes grain-boundary cracking. (c) and (d) Time evolution of median grain-boundary crack width for the coarse and fine models. The error bars denote the 25- and 75-percentiles of the crack-width frequency distribution. The overall trend is similar, but the coarse mesh exhibits slightly larger crack widths. (d) Proportion of cracked grain boundaries for the models shown in (a) and (b). The fine mesh exhibits fewer open boundaries, but the general trend is similar.

2.4.3 Grain-boundary fracture onset and propagation

The onset of cracking is a linear function of yield stress (Fig. 2.6). Crack nucleation occurs along grain vertices and triple–lines of grain- boundary junctions (Fig. 2.7), which concentrate internal stresses (Figs. 2.5a-b). Therefore, in the early stages, the crack network resembles an assemblage of pipes or narrow sheets (Figs. 7a-b) until cracks propagate across the grain faces (Figs. 7c-d).

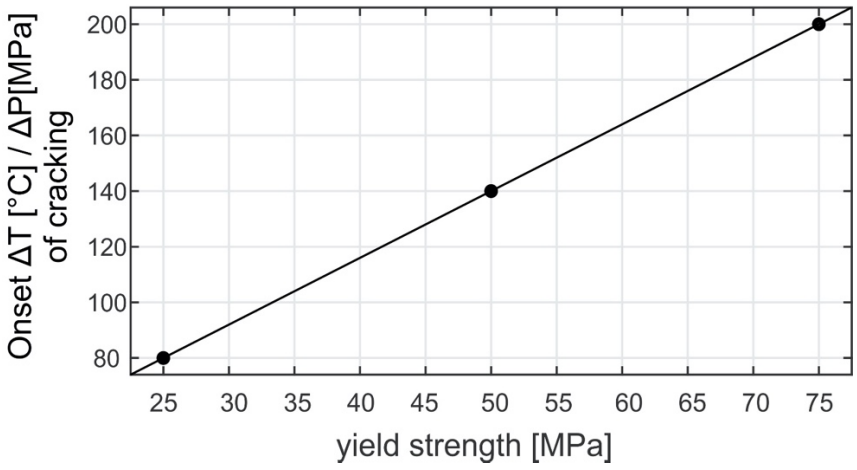

Figure 2.6. 3D modeling results of the effect of yield strength on the onset temperature of cracking during cooling from 300 to 25 °C and decompression from 300 to 22 MPa. In all cases, 50-grain models with average grain size ranging from 3 to 5 mm and 214 grain boundaries with η =100 are used. Solid line shows the linear fit.

2.4.4 The relative importance of temperature and pressure gradient for crack evolution

The relative effect of temperature and pressure gradient on the evolution of crack widths and the proportion of cracked grain boundaries is explored separately for two models with σ_y = 25, 50 MPa and η = 100. To this end, we computed two additional models for each yield stress, in which either the temperature or the pressure gradient was set to zero.

At σ_y = 25 MPa, models with only decompression or cooling exhibit the onset of cracking after ΔT (°C) = 100 ≅ ΔP (MPa). In contrast, the model subject to both temperature and pressure gradient initiates cracking earlier, after ΔT (°C) = 80 ≅ ΔP (MPa) (Fig. 2.8a). In all models, the grain-boundary crack width beyond the onset of cracking increases non-linearly. Grain-boundary crack width has the highest value for the model with only decompression and the lowest for a model with only cooling, ranging from 0.6 μm and 0.4 μm, respectively. The proportion of cracked grain boundaries for a model with only pressure gradient assumes the largest value of ca. 62 % while the model with only temperature gradient causes the lowest proportion of about 43 % (Fig. 2.8b).

At σ_y = 50 MPa, all 3 models have the same onset of cracking at ΔT (°C) = 160 ≅ ΔP (MPa) (Fig. 2.8c). The model with temperature gradient only has the highest final width of opening around 0.35 μm whereas the other models have the same value around 0.2 μm. The model including both temperature and pressure gradient has the lowest final proportion of open grain boundaries of about 2.5 %, while the model with only pressure gradient has the largest proportion of around 6.5 % (Fig. 2.8d). The model that experiences only temperature gradient is in the middle with a value of 4.5 %.

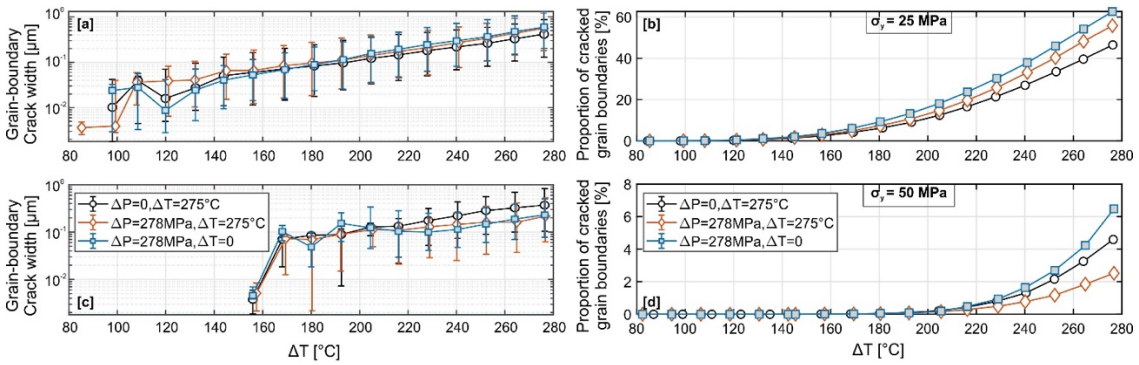

Figure 2.8. Comparison of models subject to both decompression and cooling (diamonds) to cases where only one of two is applied (squares for models with $\Delta T = 0$, and circles for those with $\Delta P = 0$). Left column: Evolution of grain-boundary crack width for (a) σ_y= 25 MPa (c) σ_y= 50 MPa. In all cases, error bars indicate the 25- and 75-percentiles of the crack-width frequency distribution for all grain-boundary nodes. Right column: Evolution of the proportion of open grain boundaries for (b) σ_y= 25 MPa (d) σ_y= 50 MPa.

2.5 Discussion

2.5.1 Grain-boundary cracks in nature and rock-physics experiments: how do our results compare?

Consistent with natural observations (Mancktelow and Pennacchioni, 2004) and experiments (Fredrich and Wong, 1986; Isaka et al., 2018; Kumari et al., 2017), grain-boundary cracks in our models nucleate at grain vertices and triple junctions (Fig. 2.7). This is because these areas provide geometrical stress concentrations. As a result, at the onset of interconnection, or percolation, the grain-boundary crack network in our models consists of fairly narrow, tube-like structures (Figs. 2.7a-b) and evolves slowly towards a more sheet-like geometry (Figs. 2.7c-d). The temperature and pressure interval for the onset of cracking depend linearly on the grain-boundary yield stress (Fig. 2.6), as expected for our simple rheological model for the grain boundaries. These critical intervals show insensitivity to the magnitudes of pressure and temperature differential during exhumation (Fig. 2.8). This observation contrasts with the 2D models of Bruner (1984), which suggest that cooling-induced internal stresses should most commonly play the dominant role in thermal-elastic cracking. The key difference between Bruner's model and ours is the considered microstructure. Grain size and shape have a large impact on local stresses, in particular in 3D (Picu and Gupta, 1997), and are not accounted for by Bruner (1984). How- ever, this notion also implies that the empirical relationship for the onset of cracking presented here is only valid for the particular microstructure under consideration, as indicated by Kruhl et al. (2013) who found that grain size relates to grain-boundary crack width in natural quartzite. Extensive cooling and/or depressurization experiments have examined crack evolution in rocks with different grain sizes (Fan et al., 2018; Isaka et al., 2018; Jin et al., 2019; Kumari et al., 2017; Wang et al., 1989; Wu et al., 2019). A notable shortcoming of studying cooling-induced cracks in the laboratory is that all samples have to be preheated first and then

cooled. Therefore, the generated cracks are a result of both heating and cooling cycles, and the reported temperature interval for the crack initiation only considers the heating cycle. For example, Wang et al. (1989) reported a temperature threshold of 85 °C ± 10 °C at ambient pressure for grain-boundary cracking in a granite sample with average grain size comparable to our models during preheating. This threshold is consistent with our models with σ_y = 25MPa and η = 100.

The evolution of crack width and the proportion of open grain boundaries are readily observed in our models. However, it is difficult to track both parameters in nature and laboratory experiments. Careful microstructural studies of natural rocks exhumed over various temperature and pressure differentials provide empirical bounds for grain- boundary crack widths and the proportion of cracked grain boundaries. High-resolution TEM studies of Kruhl et al. (2013) on quartzite show that most of the grain boundaries are partially to totally open with crack widths of up to several hundred nanometers.

In terms of the proportion of cracked grain boundaries, experimental studies (Wang et al., 1989) give a range from 60 to 75 %. Microstructural studies on a variety of natural rocks by Wirth et al. (2019) indicate an even higher amount of open grain and phase boundaries. Considering the data from naturally and experimentally cracked grain boundaries, the following model fit the observations best: σ_y = 25 MPa, η = 100.

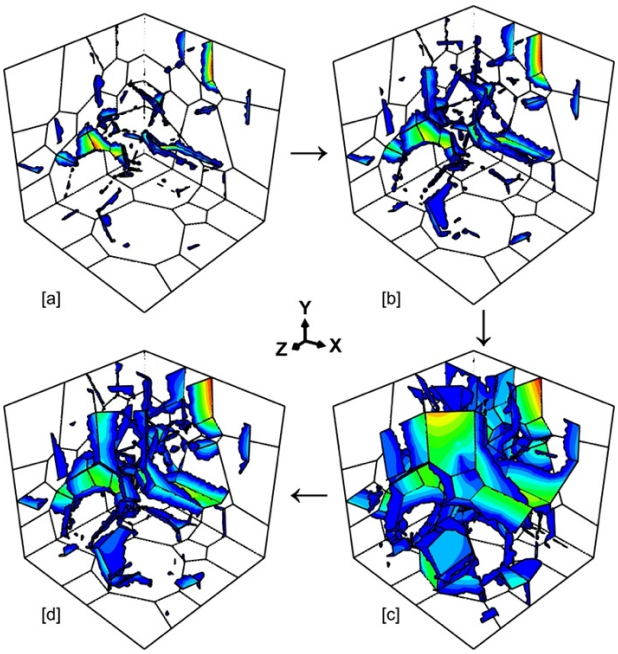

Figure 2.7. Visualization of the evolution of grain-boundary cracks during cooling from 300 to 25 °C and decompression from 300 to 22 MPa for a model with σ_y= 25 MPa and η = 100. The displayed grain-boundary cracks have a minimum opening of 1.5 nm (complete loss of cohesion has occurred). Color contours denote normal opening displacements where blue colors show low values and red ones high values. Crack initiates at ΔT (˚C) = 80 ≅ ΔP (MPa). Snapshot of propagation of crack growth in a normal direction of crack plane at (a) ΔT (˚C) =168 ≅ ΔP (MPa), (b) ΔT (˚C) = 205 ≅ ΔP (MPa), (c) ΔT (˚C) = 230 ≅ ΔP (MPa) and (d) ΔT (˚C) = 300 ≅ ΔP (MPa).

2.5.2 Simplifications of our models

Homogeneous and constant grain boundary material properties and geometry

All model grain boundaries have identical material properties that are temperature- as well as pressure-invariant. This is certainly not the case in natural materials. The strength of natural grain boundaries depends on many parameters. Of particular importance are the orientations, symmetry, and composition of the adjacent crystal lattices (Kohyama, 2002; Meyers and Ardell, 1993), lattice-scale defects (Valiev et al., 1986), and the presence of secondary nano- and micro-scale phases such as nano- and micro-pores (Hirth and Tullis, 1989, 1991) or minerals (Kanaori et al., 1991; Savanick and Johnson, 1974). Secondary phases decorating grain boundaries are very common (Herwegh et al., 2011) and usually have a large weakening effect (Mikhailovskij et al., 2011). This is the reason why our model yield strengths must be orders of magnitudes smaller than the maximum tensile yield strength of un- damaged quartz (Tromans and Meech, 2004) in order to produce any cracks over the examined PT-interval, as so commonly observed in natural rocks. However, the effective material properties of natural mineral grain boundaries are poorly known and expected to vary significantly in nature. We deliberately neglect a stochastic perturbation of grain-boundary strength for simplicity and interpret our results in terms of an effective average yield strength of high-angle quartz grain boundaries. Our best-fit results for the yield stress discussed above can thus be inverted for, as an example, the required density of grain-boundary secondary phases or defects. Moreover, all model grain boundaries are flat. This is also a special geometry only observed in particular classes of rocks. Geometrical ″asperities″ on grain boundaries such as bulges or lobate-cuspate structures (Passchier and Trouw, 2005) can be expected to have a similar effect as vertices and triple junctions: they will serve as geometric stress concentrations and enhance nucleation of grain-boundary cracks. One can thus envisage that cracking behaviour will differ as soon as a critical asperity density is reached. This analysis is beyond the scope of the work at hand.

The grains only deform elastically

Our models neglect inelastic intracrystalline deformation of quartz. In the studied temperature regime, one could expect inelastic low- temperature deformation (Groshong, 1988), for example accommodated by intragranular fracturing (Kranz, 1983), pressure-dissolution creep (Tada and Siever, 1989), deformation lamellae (Blacic, 1975; Heard and Carter, 1968), kinking (Blacic and Christie, 1984), or undulose extinction (Blacic, 1975). If any and which of these occur de- pends on a number of loading parameters such as the state of stress, temperature, pore-fluid pressure and strain rate as well as micro- structural properties of deformed minerals, for example water content of quartz, grain size, and presence of pre-existing deformation or secondary features (cracks, fluid inclusions, subgrains, etc.). Since we are mainly interested in grain-boundary

fracture, we ignore all these mechanisms. Their presence would generally provide an additional stress- relaxation mechanism and thus decrease the amount of grain-boundary fracturing (Schrank et al., 2012). Given that we start out with intact grains, our models provide upper-bound limits for dissipation by grain- boundary cracking. Moreover, an inspection of the stored differential stresses at the end of our best-fit models (Fig. 2.9) demonstrates that the largest portion of the model cube exhibits residual stresses consistent with those measured in natural quartz samples (Friedman, 1972). This suggests that, if grain boundaries constitute the weakest structural feature of quartzite, they can relax internal stresses efficiently and may thus even suppress other deformation mechanisms. This is in turn consistent with microstructures of some natural quartzites (Kruhl et al., 2013). Intragranular inelastic deformation will be subject to future research.

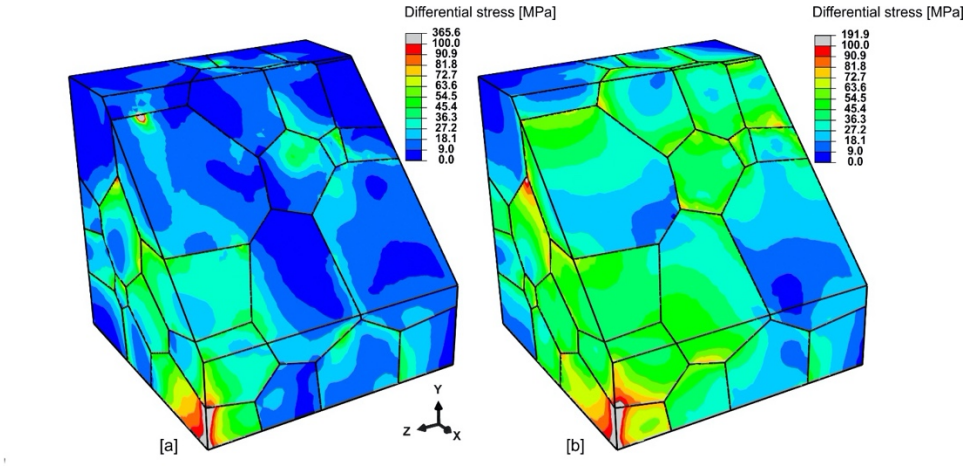

Figure 2.9. Contoured color plots of residual differential stress (MPa) after temperature and pressure gradients of 275 °C and 278 MPa for models with (a) σ_y = 25, η = 100 and (b) σ_y = 50, η = 100. High tensile strength of grain boundaries promotes larger residual differential stress. The weak model (a) exhibits intragranular differential stresses < 27 MPa throughout most of the sample. In contrast, the strong model (b) displays stored differential stresses between 36 and 64 MPa in most of the model cube. Both models yield residual differential stresses compatible with natural data for quartzite (Friedman, 1972).

Meshing and damping viscosity

Since our model rheology is rate-independent and lacking a prescribed, physically meaningful characteristic length scale, the stresses and strains are mesh-dependent near the tips of grain boundary cracks and at sharp corners and grain tips (Needleman, 1988; Wang et al., 1997). The modeling of crack tips is intrinsically challenging because stresses there are singular (Hutchinson, 1968). In our models, zones of intermittent stress/strain concentration are typically one or two elements wide (De Borst et al., 1993). Therefore, modelled stresses and strains near the tips of propagating grain boundary cracks are not reliable (Fig. 2.10). However, element size is small enough to reduce the relative error in stress to < 10 % over the distance of one or two elements in areas with corners, etc. Therefore, the state of stress within the bulk of individual model grains is

simulated quite well. When this study was conducted, Neper (Quey et al., 2011) did not permit refined meshing near grain interfaces. Hence, computational cost limited the degree to which element size could be decreased for better stress estimates. However, mesh refinement has been implemented in Neper very recently. Thus, future numerical experiments with this meshing tool will improve in the quality of stress estimates.

In addition, we used viscous regularization to tackle convergence problems due to elastic snap-back (Gao and Bower, 2004; Yu et al., 2016). While the latter approach certainly is a numerical trick, it is reasonable to assume that the opening and propagation of cracks in natural materials proceed at finite speed. The damping viscosity was used as an empirical fitting parameter in this study, and we tuned both the grain-boundary yield stress as well as the damping viscosity such that the bulk model crack evolution is consistent with natural rocks. It is important to keep in mind that the onset of cracking is not affected by our use of viscous regularization (Fig. 2.4) since the latter only kicks in after the onset of grain boundary fracturing. Moreover, models with yield stress $\geq$ 75 MPa show barely any grain-boundary cracking, regardless of the choice of mesh size and damping viscosity (see Appendix 2.C, Figs. 2.C1-2.C3). This observation is clearly inconsistent with the microstructure of natural rocks that travelled along a similar exhumation path and have similar material and geometrical properties to our models (Kruhl et al., 2013). Hence, we argue that our models provide a reliable upper bound for the grain-boundary yield stress of 75 MPa. On the other hand, for the lowest yield stress and damping viscosity studied here, the model rock essentially disintegrates completely. Since the natural samples of Kruhl et al. (2013) display a certain amount of cohesive grain boundaries that do not show evidence for later cementation, the models at hand suggest that grain-boundary yield strength is probably not much smaller than $\sim$ 20 MPa. However, physically better- constrained approaches to modeling the time evolution of crack propagation may change this lower bound. For example, energy-based criteria from classic linear fracture mechanics (Nasseri et al., 2007, 2009a, 2009b) are a good candidate and subject to ongoing work. In conclusion, while our models do not provide reliable stress fields at propagating cracks, they do allow us to narrow down the critical temperature and pressure intervals for the onset of grain-boundary cracking as well as the tensile yield stress of natural quartz grain boundaries. However, one needs to keep in mind that these values also depend on the specific microstructure (grain size, grain shape, spatial arrangement of crystallographic axes), which was kept constant here.

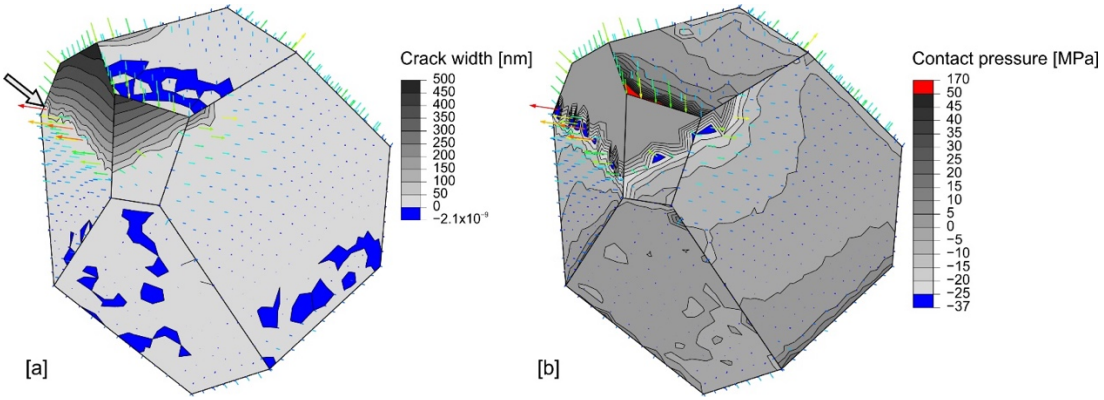

Figure 2.10. Snapshot of deforming model grain in a simulation with σ_y = 25 MPa and η = 25 after cooling to a temperature of 144 °C and experiencing a pressure drop of ca. 144 MPa. The coloured arrows denote the instantaneous normal forces acting on the boundaries of the grain. (a) Contour plot of crack width normal to grain boundary. This model grain exhibits one open grain-boundary crack extending across three grain faces, marked by the dark contoured polygons. The crack front is marked with a thick grey arrow. It emanates from triple lines at the top of the grain adjacent to faces in a compressive stress state. Regions shown in blue experience so-called overclosure where the compressive state of stress brings two closed surfaces closer to one another. As seen in [b], the associated contact pressures are not anomalously high. (b) Contour plot of contact pressure normal to the grain boundaries. The highest tensile (negative sign) contact pressure occurs at the crack front (blue polygons), the typical mesh-size effect in simulations without (artificial) characteristic length scale or regularization mechanism. For one-time step, the stresses just ahead of the crack front overshoot the tensile yield strength, here by about 12 MPa. It is clear that stresses near the crack front are not very well resolved. The red polygons denote high compressive contact stresses at a vertex points, highlighting the important geometric effect of 3D microstructure for stress distribution.

2.6 Conclusions

In this paper, fracturing of exhumation-induced grain boundaries in a millimetric-grain quartzite with randomly oriented crystallographic axes and anisotropic thermal-elastic properties is simulated in 3D. Exhumation occurs over cooling from 300 to 25 °C and decompression from 300 to 22 MPa, equivalent to exhumation from a depth of ca. 11 km to about 1 km. Failure behaviours of grain boundaries in tension and shear follow an empirical damage-mechanics model (Schrank et al., 2012) inspired by Morse-type atomic bonding models (Tromans and Meech, 2004).

Our results provide testable predictions for rocks with a similar microstructure:

(a) The maximum tensile yield strength (σ_y) of natural quartz grain boundaries is smaller than 75 MPa and may have a lower bound near 20 MPa. Overall, an increase in tensile yield stress causes a delay in the onset temperature and pressure interval of cracking and a decrease of final grain-boundary crack width as well as the proportion of open boundaries. The best-fit results are obtained for σ_y = 25 MPa which implies that, starting at 300 °C and 300 MPa, quartz grain-boundary opening initiates after a temperature and pressure decrease of ca. 80 °C and 80 MPa, respectively. Our best-fit model also indicates the value of 55 % for proportion of open grain

boundaries which is in the range of microstructural observations of natural rocks (Kruhl et al., 2013; Wirth et al., 2019).

(b) Grain-boundary fractures initiate at grain vertices and triple lines, locations with more internal stresses, and propagate across the grain faces.

(c) Statistically, the bulk effects of a pure reduction in pressure or temperature are similar in regard to grain-boundary cracking.

2.7 Acknowledgements

This research was funded by the German Research Foundation (DFG) [grant number KR691/36-1/SCHM930/17-1]. The authors would like to thank High Performance Computing Centre (HPC) of Queensland University of Technology (QUT) for access to computational facilities and valuable software support. Special thanks go to Detlef Körner at Department of Earth and Environmental Sciences Ludwig-Maximilians-Universität (LMU), and to Sebastian Felix Gehrlein at Faculty of Civil, Geo and Environmental Engineering Technische Universität München (TUM), for their technical support and for providing software license. Not least, we are grateful to the two anonymous reviewers and the editor for their useful comments that greatly helped to improve the manuscript.

2.8 Appendices

Appendix 2.A

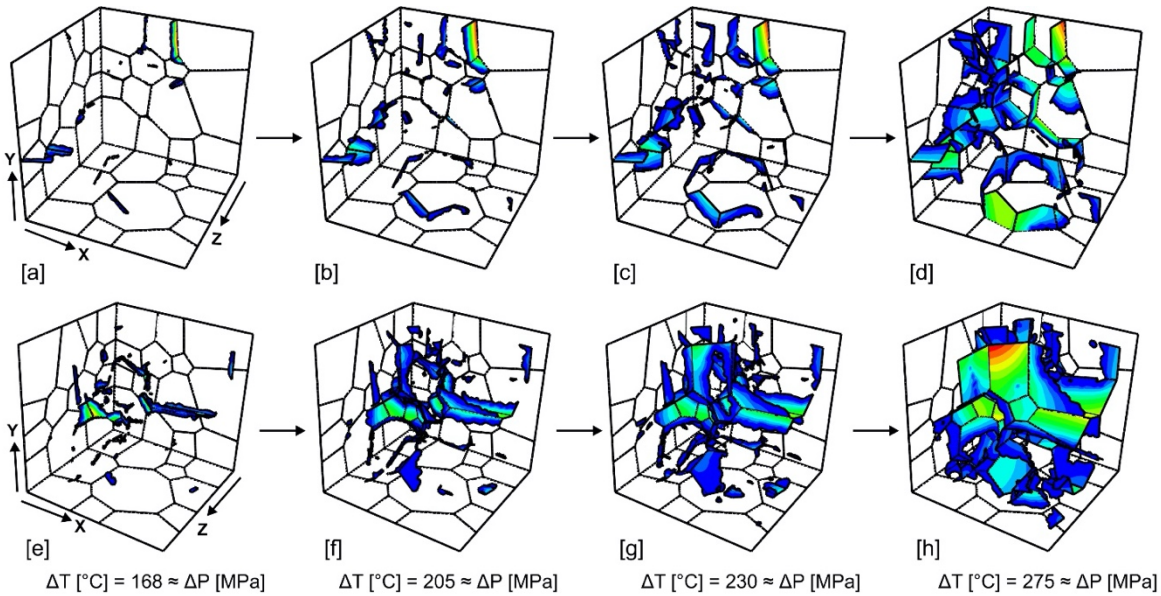

Figure 2.A1. Visualization of the evolution of grain-boundary cracks during cooling from 300 to 25 °C and decompression from 300 to 22 MPa for a model with $\boldsymbol{\sigma_y}$= 25 MPa and η = 100. Figures a-d (upper row) only shows cracks that nucleate from the model surface while figures e-h (lower row) displays only those, which nucleate in the model interior. The displayed grain-boundary cracks have a minimum opening of 1.5 nm (complete loss of cohesion has occurred). Colour contours denote normal opening displacements

where blue colours show low values and red ones high values. The comparison of upper and lower row demonstrates that grain-boundary cracks more commonly nucleate and grow in the model interior. We interpret this observation as an indication that the physical effects of boundary conditions, although visible, are negligible compared to those imposed by the choice of internal 3D microstructure and the actual material properties.

Appendix 2.B

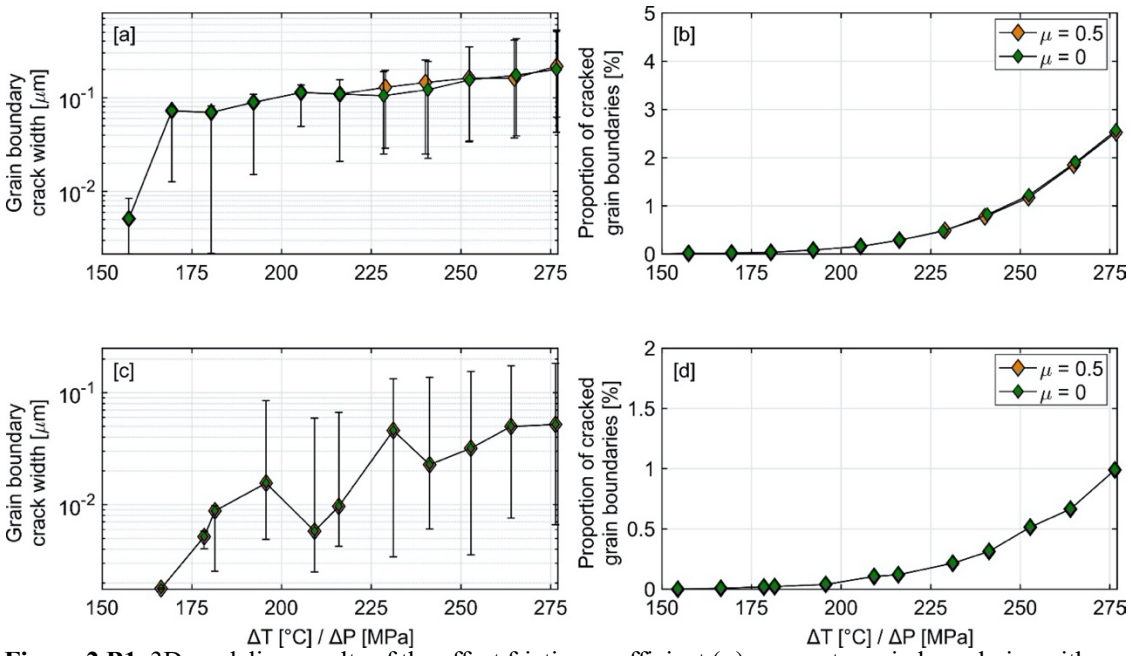

Figure 2.B1. 3D modeling results of the effect friction coefficient (μ) on quartz grain boundaries with $\boldsymbol{\sigma_y}$= 50 MPa over ΔT= 275˚C and ΔP= 278 MPa. In all cases, 50-grain models with average grain size ranging from 3 to 5 mm and 214 grain boundaries are used. (a-c): Evolution of the median of grain-boundary crack width and onset temperature and pressure of cracking for (a) η = 100 and (c) η = 250. In all cases, error bars indicate the 25- and 75-percentiles of the crack-width frequency distribution computed for all nodes on the contact surfaces making up grain boundaries. A grain-boundary node is considered as completely cracked once its displacement normal to the boundary is ≥ 1.5 nm. (b-d): Evolution of the proportion of open grain boundaries for (b) η = 100 and (d) η = 250.

Appendix 2.C

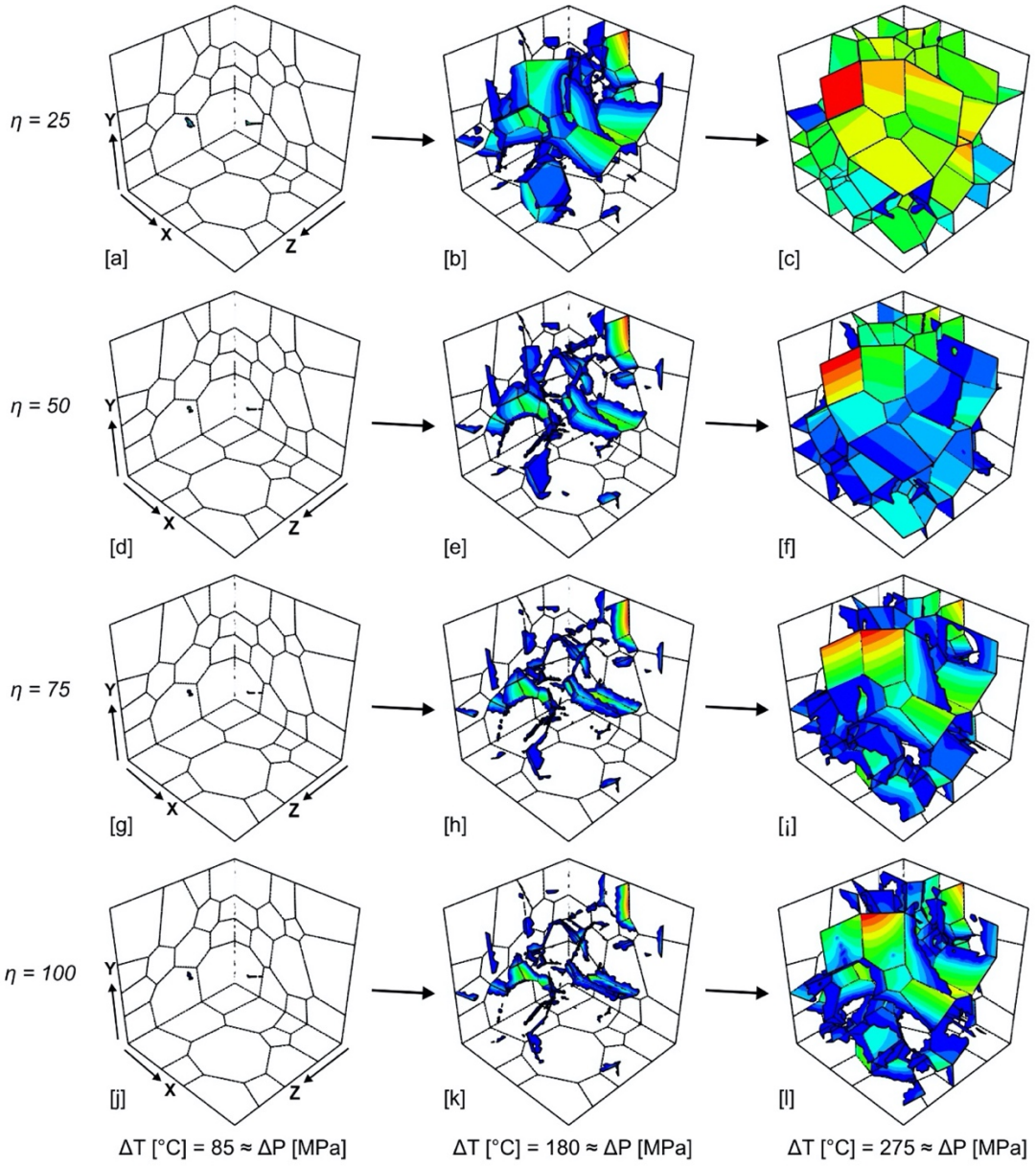

Figure 2.C1. Snapshot of the effect of damping viscosity (η) on the evolution of tensile grain-boundary cracks during cooling from 300 to 25 °C and decompression from 300 to 22 MPa for a model with $\boldsymbol{\sigma_y}$= 25 MPa. The displayed grain-boundary cracks have a minimum opening of 1.5 nm (complete loss of cohesion has occurred). Colour contours denote normal opening displacements where blue colours show low values and red ones high values. Crack initiates at $\Delta T\ (^{\circ}C) = 80 \cong \Delta P$ (MPa).

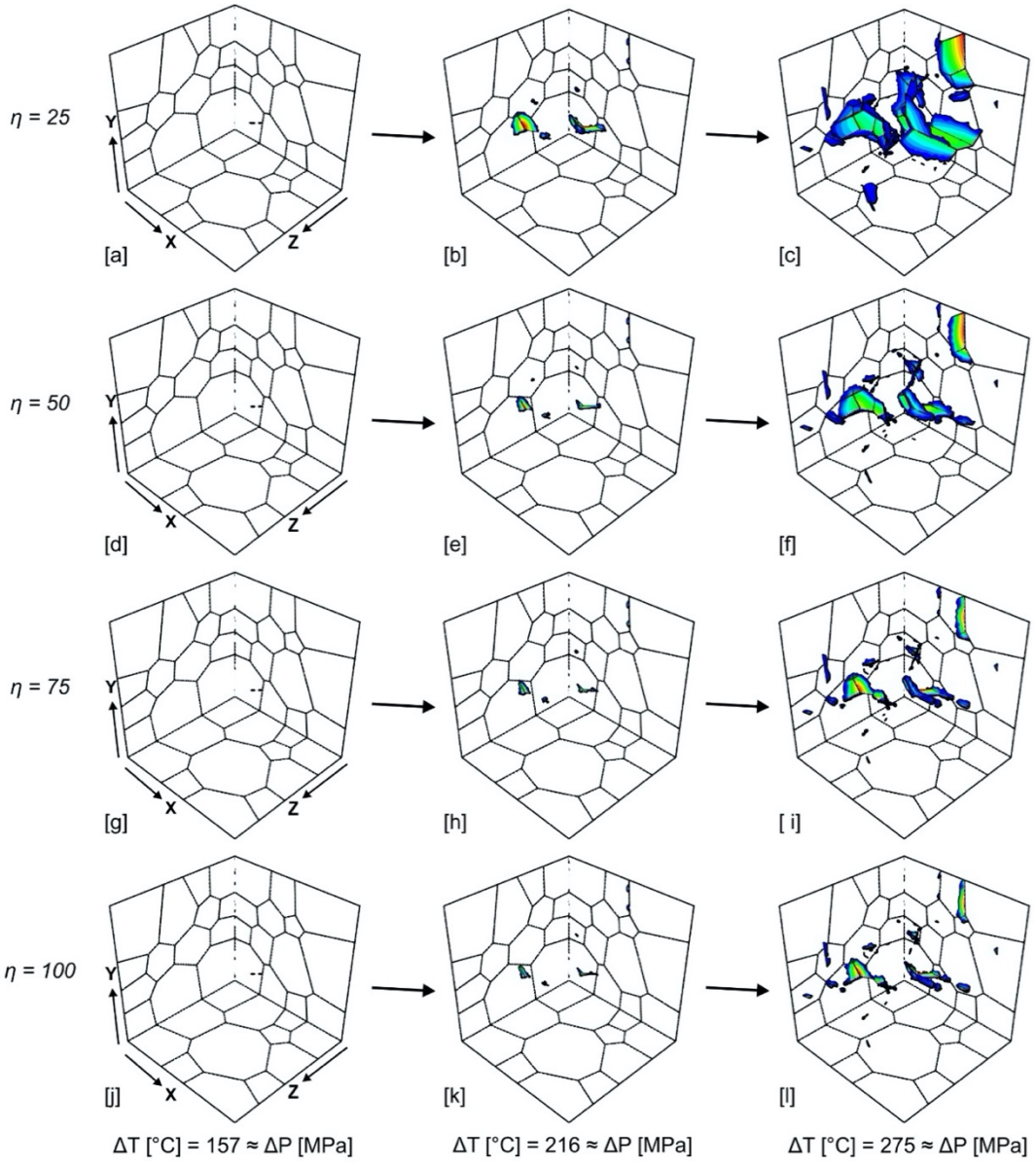

Figure 2.C2. Snapshot of the effect of damping viscosity (η) on the evolution of tensile grain-boundary cracks during cooling from 300 to 25 °C and decompression from 300 to 22 MPa for a model with σ_y= 50 MPa. The displayed grain-boundary cracks have a minimum opening of 1.5 nm (complete loss of cohesion has occurred). Colour contours denote normalopening displacements where blue colours show low values and red ones high values. Crack initiates at ΔT (˚C) = 140 ≅ ΔP (MPa).

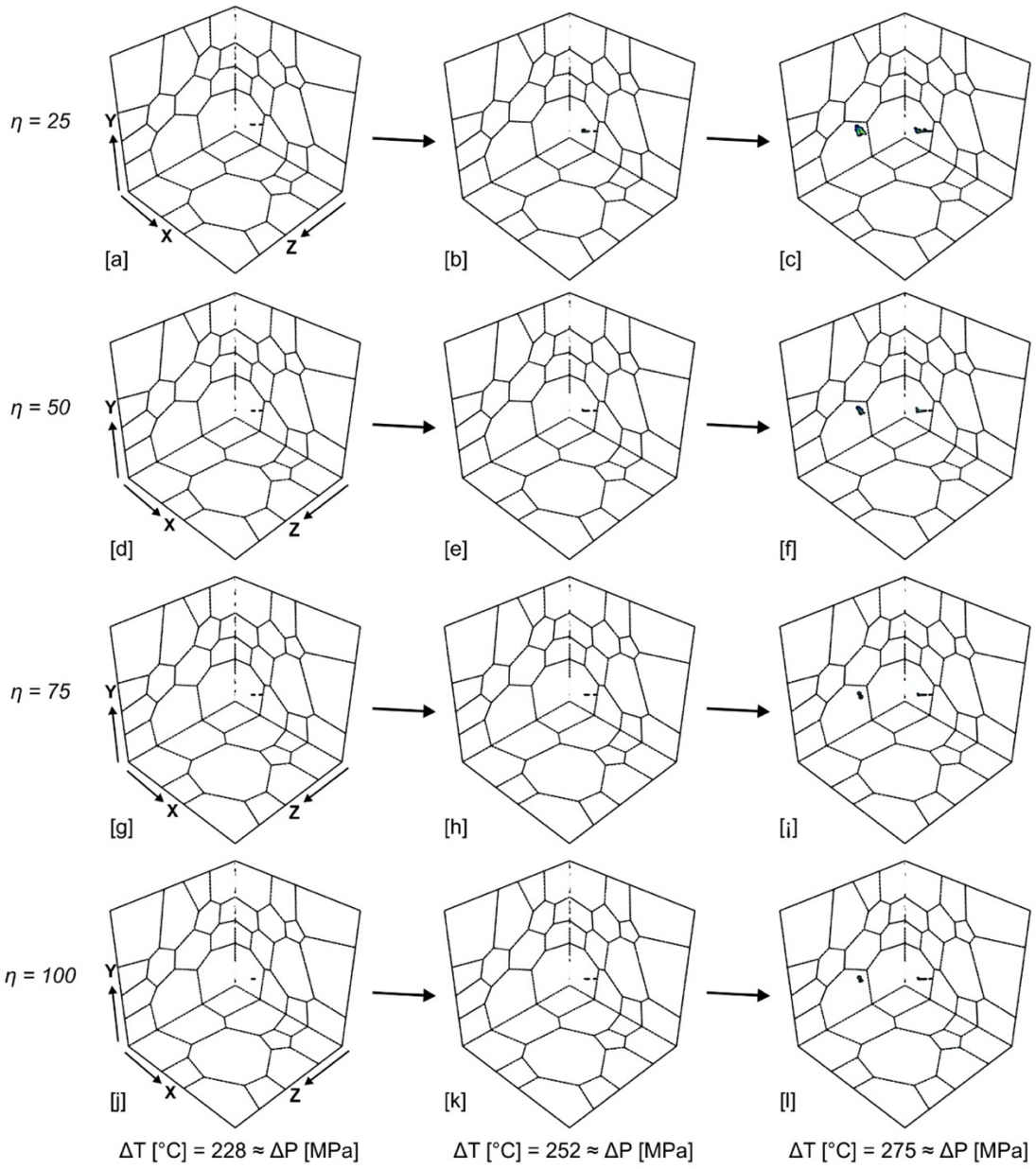

Figure 2.C3. Snapshot of the effect of damping viscosity (η) on the evolution of tensile grain-boundary cracks during cooling from 300 to 25 °C and decompression from 300 to 22 MPa for a model with σ_y= 75 MPa. The displayed grain-boundary cracks have a minimum opening of 1.5 nm (complete loss of cohesion has occurred). Colour contours denote normal opening displacements where blue colours show low values and red ones high values. Crack initiates at $\Delta T\ (^{\circ}C) = 220 \cong \Delta P$ (MPa).

Chapter 3

An alternative approach to studying exhumation-induced grain-boundary openings in quartz grain aggregates: 3D modeling

In preparation for submission: Elnaz Raghami, Christoph Schrank, Jörn H. Kruhl: An alternative approach to studying exhumation-induced grain-boundary openings in quartz grain aggregates: 3D modeling.

The underlying research was designed by Elnaz Raghami, Christoph Schrank, Jörn H. Kruhl. Elnaz Raghami performed the numerical modeling at Queensland University of Technology in Australia and wrote the manuscript. She brought it into its final shape, with comments from the coauthors.

3.1 Abstract

The evolution of exhumation-induced grain-boundary opening in quartz grain aggregates is investigated numerically with a combination of the finite-element method and contact mechanics. Grain boundaries of thermally and elastically anisotropic quartz grains in random orientation are simulated as contact surfaces that can crack. Fracture propagation along grain boundaries is modeled through a linear fracture-energy criterion, which directly relates to mode-I fracture toughness. This modeling approach is compared to our previous study, which employed an empirical stress-displacement approach for grain-boundary opening (Raghami et al., 2020). We show that the fracture-energy approach is numerically more stable and provides better estimates of contact stresses near the propagating fracture front. We then proceed with a parametric study of exhumation-induced grain-boundary cracking to examine the impact of the tensile grain-boundary strength and the fracture energy. A synthetic microstructure, which resembles a natural quartzite sample, is used to invert for ranges of tensile grain-boundary strength and fracture toughness, which in turn are compared to laboratory data. Our results indicate that the yield strength of quartz grain boundaries in the studied example varies between ca. 10 to 15 MPa, fracture-energy and fracture toughness range from ca. 0.3 to 0.9 Jm^{-2} and 0.24 to 0.45 $MPam^{0.5}$, respectively.

Keywords: Grain-boundary cracking, grain-boundary yield strength, fracture-energy, mode-I fracture toughness, internal stresses, thermal-elastic anisotropy

3.2 Introduction

Studies on thermally induced cracking in crystalline rocks during heating and cooling have received much attention (Browning et al., 2016; Bruner, 1984; Darot et al., 1992; Fredrich and Wong, 1986; Homand-Etienne and Houpert, 1989; Isaka et al., 2018; Meredith et al., 2019; Weng et al., 2020). These types of cracks generally form due to an internal stress concentration arising from the geometric mismatch of neighboring grains caused by different and/or anisotropic thermal expansion coefficients and elastic properties of constituent minerals in polycrystalline rocks. In crystalline materials, thermal stresses primarily produce microcracks along grain boundaries as predominant sources of thermal-elastic mismatch, with secondary fracturing along cleavage planes, phase boundaries or pre-existing microcracks (Brace et al., 1972; Bombolakis, 1973; Kranz, 1979; Tapponier and Brace, 1976). In previous decades, laboratory studies and natural observations have progressed to investigate the crucial impact of thermally induced microcracks on the rock's mechanical and transport properties such as thermoelastic moduli (Zhu et al., 2019a, 2019b), permeability and porosity (Chen et al., 2017; Kruhl et al., 2013; Pimienta et al., 2018), thermal conductivity (Pimienta et al., 2018), fracture toughness and strength (Nasseri and

Mohanty, 2008; Nasseri et al., 2009a, 2009b). Although most existing experimental observations have provided beneficial insight concerning the fracture mechanism in rocks, they reveal many difficulties and complexities concerning specimen preparation and monitoring of fracture initiation under pre-defined conditions (Baud et al., 2004; Desrues and Viggiani, 2004; Fusseis et al., 2012; Hall et al., 2006; Hall and Bodnar, 1989; Jansen et al., 1993; Nasseri et al., 2006; Schrank et al., 2012; Stanchits et al., 2006; Thompson et al., 2009). In order to overcome such operating limitations, the method in this paper uses computational modeling.

The cooling and decompression of a 3D quartz grain aggregate with anisotropic elastic and thermal properties in random orientation is simulated with finite element methods (FEM) and contact mechanics. Quartz grains themselves are considered as continuous anisotropic elastic bodies while their boundaries are treated as strain-softening elastoplastic cohesive interfaces with contact mechanics. In our previous study (Raghami et al. 2020), we used the following grain-boundary rheology: linear-elastic prior to yield followed by exponential strain-softening rheology in tension and shear, and cohesionless friction in shear at full failure. Although the stated rheology is common, it indicates convergence problems during separation due to local softening. To overcome convergence problems due to elastic snapback (Gao and Bower 2004; Hibbitt, Karlsson and Sorensen Inc.©, 2009; Yu et al., 2016), viscous regularization was used to stabilize the crack-opening process. Viscous regularization (Gao and Bower, 2004; Yu et al., 2016) introduces an arbitrary linear rate dependence in the separation law and leads to stress modification through viscous damping, stabilizing crack growth and opening. However, the viscous damping term does not have a sound physical or experimental meaning and thus cannot be easily related to material properties measured in the laboratory. Moreover, some singularities were found in the computation of stresses and strains near crack tips and during crack growth (Raghami et al., 2020; section 4.2.3), which are undesirable. To overcome these shortcomings, we explore a different damage rheology for cohesive grain boundaries, which is based on a linear fracture-energy criterion (Hibbitt, Karlsson and Sorensen Inc.©, 2009). One significant advantage of this approach is that the fracture-energy dissipated during crack opening relates directly to mode-I fracture toughness (K_{IC}), which is commonly measured in the laboratory for a wide range of rocks (Dutler et al., 2018; Feng et al., 2019; Guardiola et al., 2004; Möller and Bitzek, 2014; Nasseri et al., 2006; Whitney et al., 2007; Wood and Weidlich, 1982). Fracture toughness is a key material property, which reflects the ability of rocks to resist fracturing. Deformation experiments on several rock types (Bhagat, 1985; Gunsallus and Kulhawy, 1984; Haberfield and Johnston, 1989; Hanson et al., 1994; Khan and Al-Shayea, 2000; Whittaker et al., 1992; Zhang et al., 1998) have determined that mode-I fracture toughness is directly proportional to the tensile strength and can be expressed as

$$\sigma_y = a_0 K_{IC}, \quad (1)$$

where σ_y is tensile strength, K_{IC} is fracture toughness and a_0 is a constant value. For soil a_0 is 15.4, and for soft rock has a value of 13.6 (Hanson et al., 1994). An empirical constant value (a_0 = 6.88) was introduced by Zhang (2002) for wide range rock types, from soft sedimentary to igneous and metamorphic hard rocks, under quasi-static or low speed impact loading. Four sources of experimental data (Khan and Al-Shayea, 2000; Nordlund et al., 1999; Whittaker et al., 1992; Zhang et al., 1998) were used by Zhang, (2002) as shown in Fig. (3.1).

The concepts of fracture-energy and fracture toughness have a sound foundation in the classical theory of linear fracture mechanics and experimental rock physics. They constitute commonly measured quantities for a wide range of rock types. This motivates us to use these concepts in the modeling study at hand. Additional technical improvements in the current study are enabled by advances in Neper version 3.5.2, a free (open source) software package used for model generation and meshing (Quey, 2020). In our previous study, mesh refinement along grain boundaries could not practically be conducted by Neper (Quey et al., 2011). In the absence of a physically meaningful regularization mechanism, simulation of stresses and strains near the tips of grain boundary cracks, at sharp corners and grain tips exhibit mesh-size sensitivity (Needleman, 1988; Wang et al., 1997). This localized mesh-size effect is reduced when a non-uniform mesh with increasingly finer elements along the grain boundaries is used. The new mesh element sizes along grain boundaries is ca. 0.45 % of the average grain size whereas the size of these elements is ca. 4 % of the average grain size within the grains. In contrast, the mesh element used in our previous study (Raghami et al., 2020; Fig. 3.1) was uniform along grain boundaries and within the grain with values ca. 10 % of average grain size. In addition, the new mesh not only improves resolution and stress accuracy near grain boundaries but also reduces element numbers within grains and computation time.

In the following, we first compare the modeling approach using a fracture-energy criterion to our previous study (Raghami et al., 2020). We then present a case study of the new modeling approach where we attempt to estimate the fracture toughness and tensile yield strength of a natural quartzite sample (Kruhl et al., 2013) with a parametric study. A critical discussion of the modeling approach and the natural case study concludes this contribution.

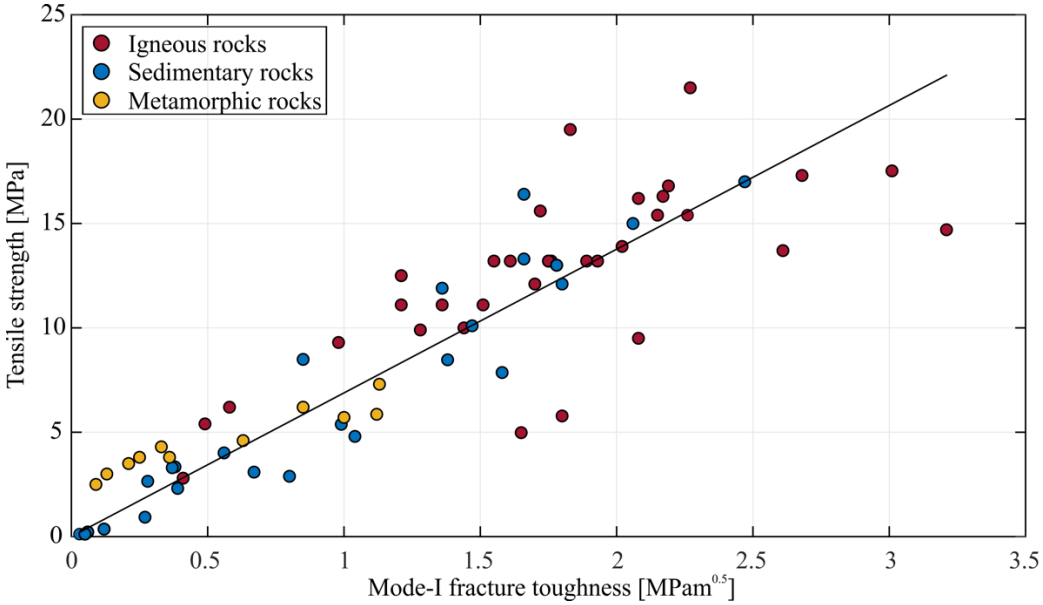

Figure 3.1. Empirical relation reported by Zhang (2002) between mode-I fracture toughness and tensile yield strength of rocks. The solid black line is the linear regression to 69 rock types for zero intercept (R^2 = 0.65, RMSE = 3.29).

3.3 3D modeling of grain-boundary cracking: methods

We investigate the fracture behavior of quartz grain boundaries in 3D grain-scale models. These models have foam microstructures and are created in model cubes composed of quartz. We simulate linear and time-independent temperature and pressure drops corresponding to those determined for the natural quartzite samples in Kruhl et al. (2013): cooling from 300 (roughly the "recrystallization temperature" of quartz; Stipp et al., 2002; Voll, 1976) to 25 °C and decompression from 300 to 22 MPa.

3.3.1 3D microstructure generation and meshing

To generate 3D models that are sufficiently compatible with the geometric heterogeneity of annealed natural quartz microstructures, we employ a foam-structure technique. The foam-structure is created by the grain growth morphological approach implemented in Neper (Quey et al., 2011). The resulting grains in the polycrystalline structure are polyhedral with no overlaps and planar boundaries.

There are two types of model cubes in this paper. In the first group, to compare the results obtained from a fracture-energy criterion with those from our previous approach (i.e. stress-displacement approach), we use 3D models which are geometrically identical to those used in Raghami et al. (2020; section 2.1): the assumed domain is a cube with 15 mm edge length, consisting of 50 discrete deformable grains with random crystallographic orientation, grain diameters ranging from 3 to 5 mm and 214 grain boundaries. The model has 823,996 tetrahedral 4-node linear-displacement and linear-temperature elements (C3D4T) and a corresponding

characteristic element length of ca. 423 µm. Each grain boundary in the finite-element (FE) model acts as contact surface with the initial separation of zero at the onset of analysis.

In the second group, to estimate the fracture toughness and yield strength of quartz grain boundaries compared to natural rocks using the fracture-energy approach, we generate 3D models comparable to natural quartz samples in Kruhl et al. (2013).

Before going into detail, it should be noted that we only model 30 grains in our new models because the fracture evolution is statistically identical to 50-grain models (Appendix 3.A, Fig. 3.A.1). The 30-grain model is still valid in evaluating the grain-boundary fracture behavior and beneficial in reducing the computational time.

To obtain a distribution of quartz grain sizes similar to those of the samples analyzed by Kruhl et al. (2013), thirty discrete deformable grains with random crystallographic orientation and 129 grain boundaries are generated by the 3D random polycrystal generator Neper (Quey et al., 2011) in a millimetric cubic domain. The resulting model grains have diameters ranging from approximately 210 to 578 µm. Models are meshed by 372,114 4-node linear displacement and temperature tetrahedral mesh elements (C3D4T) with characteristic sizes ranging from ca. 1.65 to 15 µm. Mesh density has non-uniform distribution: finer elements along grain boundaries and coarser elements within the grains (Fig. 3.2).

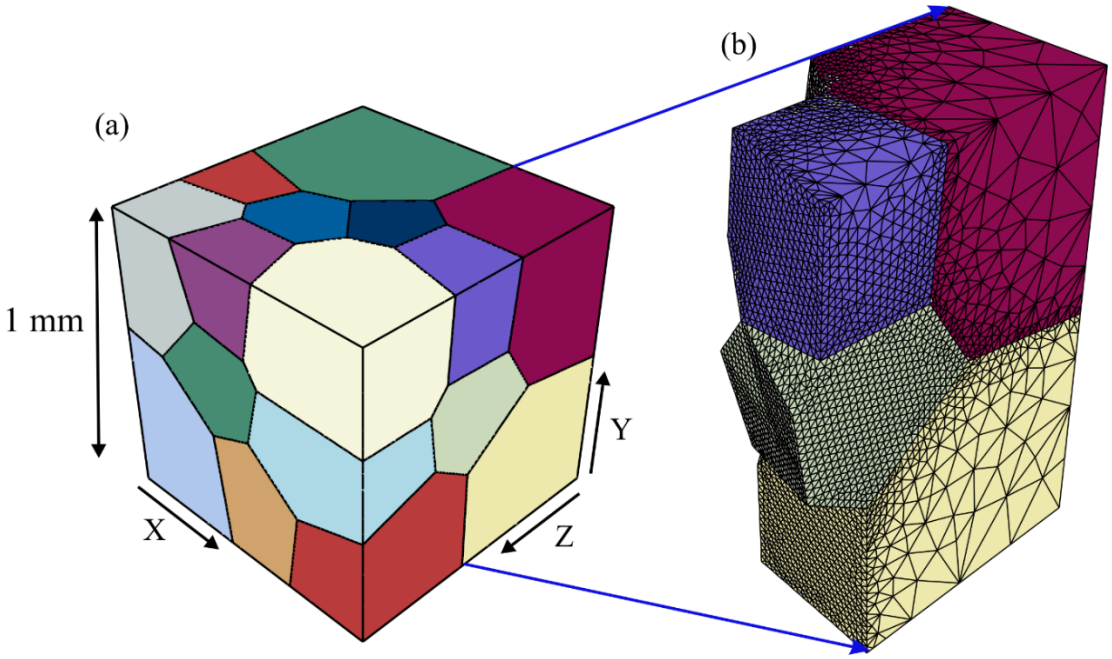

Figure 3.2. Foam microstructure and detailed view of grain-based models with high resolution mesh composed of tetrahedral elements generated by Neper (Quey et al., 2011). Colors mark individual grains with random crystallographic orientation. XYZ represents the global coordinate system (a right-handed, rectangular Cartesian system). (a) 30-grain model with 129 grain boundaries generated in a cubic domain (1 mm edge length). The grain size ranges from 210 to 578 µm. The non-uniform mesh elements shown here have characteristic sizes ranging from ca. 1.65 to 15 µm, which are created by Neper (Quey et al., 2011) relative to size of each grain.

3.3.2 Governing equations

We solve the governing equations with the implicit Lagrangian FE solver ABAQUS Standard using adaptive time stepping (Hibbitt, Karlsson and Sorenson Inc. ©, 2009). Problems with the simultaneous temperature and displacement fields are solved by coupled temperature-displacement analysis and the large-displacement formulation, which has additive strain-rate decomposition and uses Jaumann's stress rate (Jaumann, 1911).

The governing equations describe the conservation of mass, conservation of both linear and angular momentum, and conservation of energy. The conservation of mass for any deformable solid is defined as:

$$\frac{D\rho}{Dt} + \rho\nabla v = 0, \tag{2}$$

where ρ is density and v is the velocity vector. Inertia terms are neglected. Therefore, the total momentum of the system is equal to linear momenta, which can be written in terms of Cauchy stress tensor $\boldsymbol{\sigma}$ and body force vector f:

$$\nabla . \boldsymbol{\sigma} + \rho \mathrm{f} = 0, \tag{3}$$

Moreover, the conservation of angular momentum leads to a symmetric tensor for the Cauchy stress. For our purposes, conservation of energy is related to thermal energy and is given by Regenauer-Lieb and Yuen (2004):

$$\rho c_p \frac{DT}{Dt} - \nabla(k\nabla T) = 0, \tag{4}$$

where c_p is specific heat capacity; T is temperature; $\frac{D(.)}{D(.)}$ is the material derivative; t is time; and k is thermal conductivity.

3.3.3 Rheological properties

Grains

Intracrystalline plasticity in the studied temperature interval for quartz (i.e., α-quartz) is not considered since at temperatures below ca. 300 °C ("recrystallization temperature"), diffusion-driven crystal-plastic deformation is ineffective in quartz (Stöckhert et al., 1999). As solid model grains have a fully anisotropic linear-elastic rheology, their thermoelastic behavior is governed by the general form of Hook's law (Wang et al., 2018) together with the thermal strain according to:

$$\boldsymbol{\sigma} = \boldsymbol{C}: (\boldsymbol{\varepsilon} - \boldsymbol{\varepsilon}^{\theta}), \tag{5}$$

where $\boldsymbol{\sigma}$ is the Cauchy stress tensor, $\boldsymbol{C}$ is the fourth-order stiffness tensor, $\boldsymbol{\varepsilon}$ is the second-order total strain tensor and $\boldsymbol{\varepsilon}^{\theta}$ is the thermal strain, which can be defined based on thermal expansion tensor $\boldsymbol{\beta}$:

$$\boldsymbol{\varepsilon}^{\theta} = \boldsymbol{\beta}(T - T_0), \tag{6}$$

where, T_0 is the reference temperature. Trigonal symmetry of quartz reduces elastic stiffness tensor components to six independent coefficients ($C_{11}, C_{12}, C_{13}, C_{14}, C_{33}, C_{44}$) (Heyliger et al., 2003).

Grain boundaries

Grain boundaries as interfaces between adjacent grains are modeled as planar contact surfaces with identical contact properties in all constructed 3D models. They have no initial separation at the onset of analysis. Their failure behavior is determined by the node-to-surface contact method with a master-slave approach and the small-sliding approximation proposed in Hibbitt, Karlsson and Sorenson Inc. © (2009). Prior to crack initiation across grain boundaries, contact stresses are linear-elastic (Eq. 7a). Crack initiation and propagation are based on an elastoplastic damage model in tension and shear (Eq. 7b). We determine onset of failure by a displacement-dependent tensile yield strength, which is reached at the critical displacement d_{crit}. When displacements exceed d_{crit}, stresses transmitted across the interface progressively decay to zero up to a maximum displacement d_{max}, at which complete failure has occurred. The shape of the stress-displacement decay function is controlled by the damage variable D (Eq. 7b). The resulting elastoplastic damage interface rheology can be written as:

$$\sigma(d) = \begin{cases} d \le d_{crit} \rightarrow \sigma(d) = K_n d & (a) \\ d > d_{crit} \rightarrow \sigma(d) = \sigma_y\big(1 - D(d)\big) & (b) \end{cases}, \tag{7}$$

where σ is tensile/shear traction, σ_y is tensile/shear yield stress, d is extensional/shear displacement perpendicular/parallel to the grain-boundary segment under consideration, K_n is an elastic modulus with unit Pa/m, and D as a damage parameter has values between 0 and 1. Linear or non-linear softening function can be implemented through the damage variable D. For our fracture-energy approach, a linear decay of contact stresses is modeled via the damage parameter D (Hibbitt, Karlsson and Sorenson Inc. ©, 2009) (Appendix 3.A, Fig. 3.A.2b):

$$D(d) = \frac{d(d_{max} - d_{crit})}{d_{max}(d - d_{crit})}, \tag{8}$$

where $d_{max} = \frac{2G}{\sigma_y}$, with G as the fracture-energy at the critical displacement. The use of this specific damage evolution is consistent with the concept of critical energy release rate during damage processes to compute the displacement at which full material damage occurs.

In contrast, in our previous study (Raghami et al., 2020), stresses across grain boundaries are modelled by an exponential elastoplastic damage law as a function of relative displacement (Appendix 3.A, Fig. 3.A.2a), inspired by Morse-type bonding models (Tromans and Meech, 2004):

$$D(d) = 1 - \frac{d_{crit}}{d}\left(1 - \frac{1-\exp\left(\frac{-a(d-d_{crit})}{d_{max}-d_{crit}}\right)}{1-\exp(-a)}\right), \quad (9)$$

where a is a shape parameter. The relevant material parameters are displayed in Table 3.1.

In both approaches, we do not consider healing of cracked grain boundaries. Nevertheless, if in later stages open grain boundaries come into contact again, compressive stresses are transferred in contraction. In addition, if the grain boundaries slide past one another, the relation between shear and normal stress follows a static linear isotropic friction model with constant friction coefficient μ and zero cohesion.

Table 3.1. Quartz grain-boundary properties

σ_y (MPa)	K_n (m^{-1}MPa)	G (Jm^{-2})	d_{crit} (nm)	d_{max} (nm)	ζ ($Wm^{-2}K^{-4}$)	e_A, e_B	K ($JK^{-1}m^{-2}s^{-1}$)	F	a
3	6.02×10^{15}	0.15 to 15	0.5	1.5	5.67×10^{-8}	0.8	3000	1	1
5	1.0×10^{16}								
10	2.0×10^{16}								
15	3.0×10^{16}								
20	4.0×10^{16}								
25	5.0×10^{16}								
30	6.01×10^{16}								

3.3.4 Boundary and initial conditions

Boundary and initial conditions are identical with those used in Raghami et al. (2020): Planes corresponding to the Cartesian coordinate system are fixed only in directions perpendicular to each plane to avoid model translation; the entire model starts at a temperature of 300°C and a compressive mean stress of 300 MPa, with closed grain boundaries and zero local differential stresses at the beginning of the exhumation process; and during the exhumation procedure, linear temperature and pressure drops apply to the model from 300 to 25 °C and 300 to 22 MPa, respectively.

3.3.5 Material properties

Grains

All grains are assumed to have the same thermo-elastic properties: anisotropic thermal expansivity with the coefficients α_{11}, $\alpha_{22} = \alpha_{33}$ and elastic stiffness (Table 3.2), isotropic temperature-dependent thermal conductivity (Appendix 3.A, Fig. 3.A.3a), specific heat capacity (Appendix 3.A, Fig. 3.A.3b), and constant density ρ (Table 3.2). Thermal-elastic mismatch is induced by generating randomly oriented crystal lattices from grain to grain, as described in Raghami et al. (2020).

Table 3.2. Material properties of quartz grains used in 3D models

ρ (Kgm^{-3})[a]	α_{11} (°C $^{-1}$)[b]	α_{33} (°C $^{-1}$)[b]	C_{11} (GPa)[a]	C_{12} (GPa)[a]	C_{13} (GPa)[a]	C_{14} (GPa)[a]	C_{33} (GPa)[a]	C_{44} (GPa)[a]
2646.6	14×10^{-6}	9×10^{-6}	87.16	6.64	12.09	-18.15	106.00	58.14

[a] From Heyliger et al. (2003)
[b] From Vázquez (2015)

Grain boundaries

For simplicity, all grain boundaries have the same contact properties in any simulation. Based on natural measurements of the structural width of intact grain boundaries in a quartzofeldspathic ultramylonite (Hiraga, 1999), we use d_{crit}= 0.5 nm. Moreover, a value of 1.5 is used as a maximum separation d_{max} in stress-displacement approach, which is consistent with X-ray scattering results on Volterra alabaster obtained by Schrank et al. (2020).

For the comparison of the different damage laws (i.e., the linear fracture-energy criterion versus exponential displacement criterion), we use a tensile strength (σ_y) of quartz grain boundaries of 25 MPa, the best-fit result from our previous study (Raghami et al., 2020). In addition, we choose G = 7 Jm^{-2}, a value close to the area under the old damage model (Appendix 3.A, Fig. 3.A.2a).

For the parametric study, σ_y and fracture-energy G are varied systematically. Our choices for values of G are inspired by laboratory measurements of fracture energies of intact quartz single crystals (Brace and Walsh, 1962; Darot et al., 1985; Feng et al., 2019; Hartley and Wilshaw, 1973; Mueller et al., 2015; Parks, 1984). They typically range from 0.2 to 15 Jm^{-2}. As the grain boundaries are regions with weak atomic bonds, it is reasonable to assume that the fracture-energy of a grain boundary is lower than values relevant to single grains. A grain-boundary can be 100 times weaker than the maximum stated here (Peck and Gordon, 1982; Tromans and Meech, 2004), thus we test the following values: G = [0.15; 1.5; 7.5; 15]. According to Zhang (2002), the tensile strength for this range of fracture energies varies from ca. 1 to 23 MPa. Here we examine the following parameter range: σ_y (MPa) = [3; 5; 10; 15; 20; 25; 30].

In all models, the conductive heat transfer between closed contact surfaces is defined by Fourier's law:

$$q = -K(T_A - T_B), \tag{10}$$

where K is the grain boundary conductance. With progressive grain-boundary fracturing, K decreases linearly as a function of normal distance between adjacent grain boundaries and assumes that the value of K drops to zero after 1µm. If grain boundaries are completely cracked, heat flux (q), as the rate of energy emission per unit surface crossing the gap between contact surfaces, follows the radiation law (Hibbitt, Karlsson and Sorenson Inc. ©, 2009):

$$q = H[(T_A - T_0)^4 - (T_B - T_0)^4], \tag{11}$$

where T_A and T_B denote the temperatures of the adjacent cracked grain surfaces, T_0 is the absolute zero on the used temperature scale, and the coefficient H is given by:

$$H = \frac{F\zeta}{\frac{1}{e_A}+\frac{1}{e_B}-1}, \quad (12)$$

where ζ is the Stefan-Boltzmann constant, F is the effective view factor, and e_A and e_B are the emissivities of the adjacent grain surfaces. All parameters are summarized in Table 3.1.

3.4 Results

3.4.1 Comparison of the fracture-energy approach to the stress-displacement approach

In this section, the performance of the fracture-energy approach (the "new" approach in the following) on the fracture behavior of quartz grain boundaries subjected to cooling from 300 to 25 °C and decompression from 300 to 22 MPa is assessed by comparing the computed results with the stress-displacement approach (Raghami et al., 2020, the "old" approach). For this objective, the new models are identical to those in Raghami et al. (2020) with two exceptions: the grain-boundary damage law, as explained above, and the magnitude of the viscous damping term. In the old model, the damping term has a value of 100, and in the new model a smaller value of 10.

Modelled stresses and strains near crack tips

The two approaches exhibit remarkable differences in the stresses and strains near the tips of grain-boundary cracks. The old approach demonstrates excess stresses and strains near the tips of propagating grain boundary cracks. The maximum stress overshoots the yield strength by 126 MPa due to excessive viscous damping accommodating the elastic snapback at the adjacent grain boundary crack front (Fig. 3.3a). In contrast, the overshooting is significantly decreased to around 35 MPa by the fracture-energy approach and confined in a narrower zone (Fig. 3.3b). The alternative approach diminishes the problem of overshooting at the crack tips encountered in the previous study.

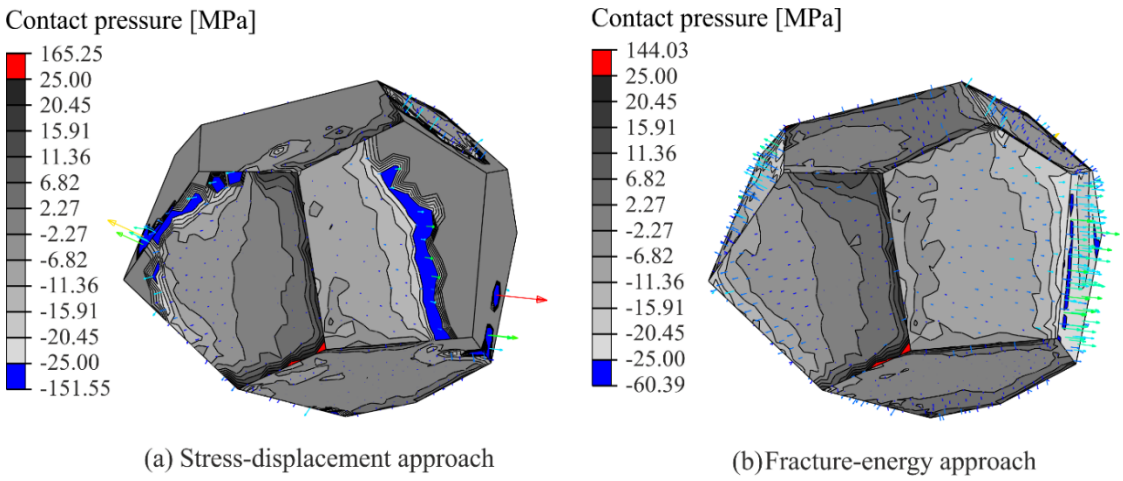

(a) Stress-displacement approach (b) Fracture-energy approach

Figure 3.3. Snapshot of deforming model grain in a simulation with (a) stress-displacement approach used in Raghami et al. (2020) ($\boldsymbol{\sigma_y}$ = 25 MPa and η = 100), (b) fracture-energy approach ($\boldsymbol{\sigma_y}$ = 25, G = 7 Jm^{-2} and η = 10). Contour plot of contact pressure normal to the grain boundaries after cooling to a temperature of 48 °C and experiencing a pressure drop of ca. 48 MPa. The colored arrows denote the instantaneous normal forces acting on the boundaries of the grain. The highest tensile (negative sign) contact pressure occurs at the crack front (blue polygons). For the model with stress-displacement approach, the stresses just ahead of the crack front overshoot the tensile yield strength, here by about 126 MPa. In contrast, for a model with the fracture-energy approach, the maximum excess stress is ca. 35 MPa. Therefore, elastic snapback does not pose as much of a problem near the crack front in the fracture-energy approach.

Convergence

We use adaptive time stepping based on half-increment residuals (Hibbitt and Karlsson, 1979). Thus, the step time can be used to monitor convergence. In both compared modeling approaches, the size of the initial step-time increment in the elastic regime is set to 10 to facilitate fast initial convergence of the contact code. Maximum step-time size is limited to 400 in the old approach and 100 in the new approach. The damping coefficient η is a linear-viscous relaxation time. Hence, with $\eta = 100$ in the old models and $\eta = 10$ in the new ones, the former steps forward at four relaxation times at its maximum and the latter at 10 relaxation times. Therefore, at the largest permitted step time, the old models involve contact stresses relaxed to about 98% of their steady-state value while the new ones can be considered 100% at steady state. Both approaches reach their maximum step time quickly in the elastic regime, which attests to smooth convergence there (Fig. 3.4a). However, at the onset of failure, the old approach encounters convergence difficulties and cuts back step time to $< \eta$ (Fig. 3.4b). Until the end of the model run, the step time remains at $< \eta$ and shows periodic oscillations of step time, which indicates convergence issues associated with significant overshooting of stresses near propagating cracks (Fig. 3.4a). In contrast, the new approach moves forward at constant step increments of 10η for more than half of the total runtime and cuts back only once to just below 8η (Fig. 3.4b). Since the step increments are well above five relaxation times, the overshooting problem is significantly reduced.

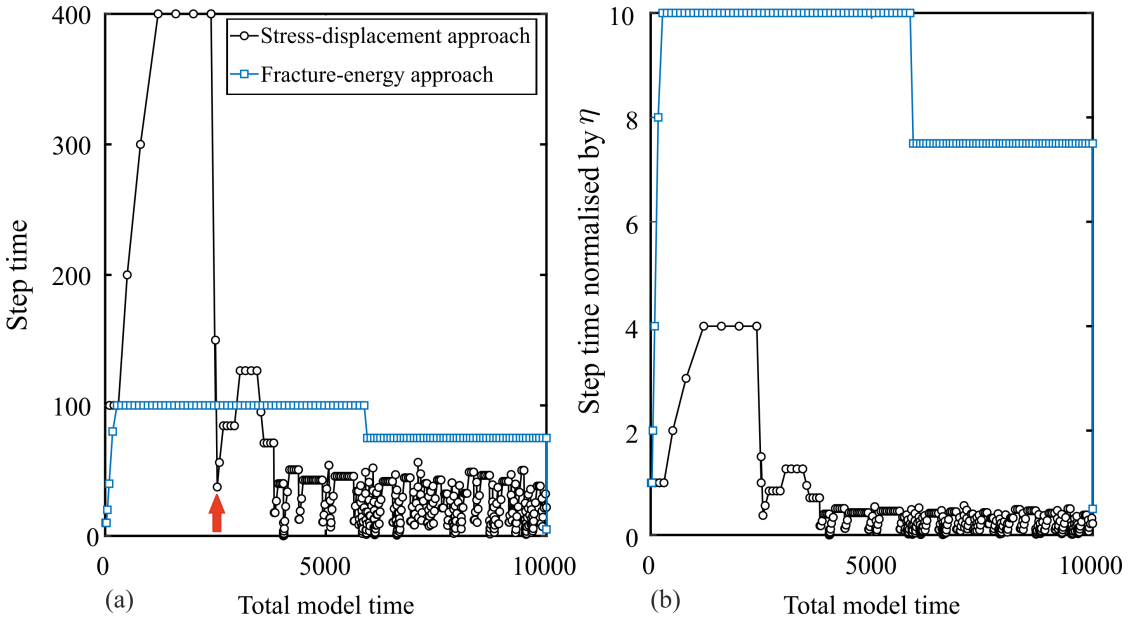

Figure 3.4. Monitoring of model convergence through evolution of adaptive step time over total time. Time is in arbitrary units. Plots of (a) absolute step time over total model time, and (b) step time normalized by the damping coefficient, which is a viscous relaxation time. The red arrow in (a) marks the onset of grain-boundary cracking.

Grain-boundary crack evolution

The relative effect of the fracture-energy on the grain-boundary crack width and the proportion of cracked grain boundaries compared to the previous study (i.e., the stress-displacement approach) for a 50-grain model consisting of 214 quartz grain boundaries with σ_y= 25 MPa is represented in Fig. 3.8. The value of G = 7 Jm^{-2} is employed for fracture-energy, which is close to the area under the previous damage model (Appendix 3.A, Fig. 3.A.2a).

The onset temperature and pressure of cracking as well as the final grain-boundary crack width in both approaches exhibit no significant differences, as expected. Finally, only the post-failure behavior of grain boundaries is varied in the new approach. The onset of cracking begins around ΔT (°C) = 85 ≅ ΔP (MPa) (Fig. 3.5a) and the final grain-boundary crack width is around 0.6 μm.

There is a non-linear increase in grain-boundary crack width and proportion of cracked grain boundaries beyond the onset of cracking in both cases. However, in the new model, grain-boundary crack width grows more slowly up to a finite temperature increment of ca. 25 °C. Moreover, the new approach results in a significant drop from ca. 60% to 40 % in the final proportion of cracked grain boundaries.

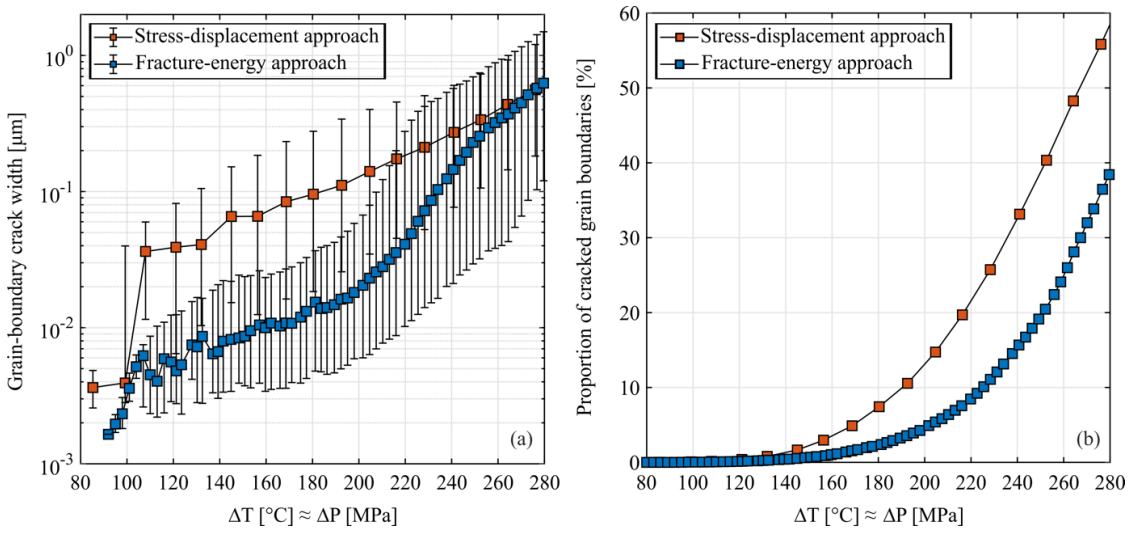

Figure 3.5. Comparison of modeling results obtained from fracture-energy ($\boldsymbol{\sigma_y}$ = 25, G = 7 Jm^{-2} and η = 10) and stress-displacement approaches ($\boldsymbol{\sigma_y}$ = 25 MPa and η = 100) for quartz grain-boundary cracks over ΔT= 275˚C and ΔP ≅ 278 MPa. In all cases, 50-grain models with grain size ranging from 3 to 5 mm and 214 grain boundaries are used. (a) Evolution of grain-boundary crack width. The symbols denote the median of the crack-width frequency distribution, and the lower and upper limits of the error bars denote the 25%- and 75%-percentile, respectively. A grain-boundary node is considered as completely cracked once its displacement normal to the boundary is ≥ 1.5 nm. (b) Evolution of the proportion of cracked grain boundaries.

With the exception of highly localized overshooting near crack tips, the ranges in contact pressures on grain boundaries are similar in both approaches (Fig. 3.6). Maximum contact pressures occur at vertex points and triple lines in both models, indicating that grain-boundary cracking preferentially nucleates at these locations. In the fracture-energy method, regions of high contact pressure at the triple lines show smaller and less nonlinear spatial gradients than in the stress-displacement method (Fig. 3.6a).

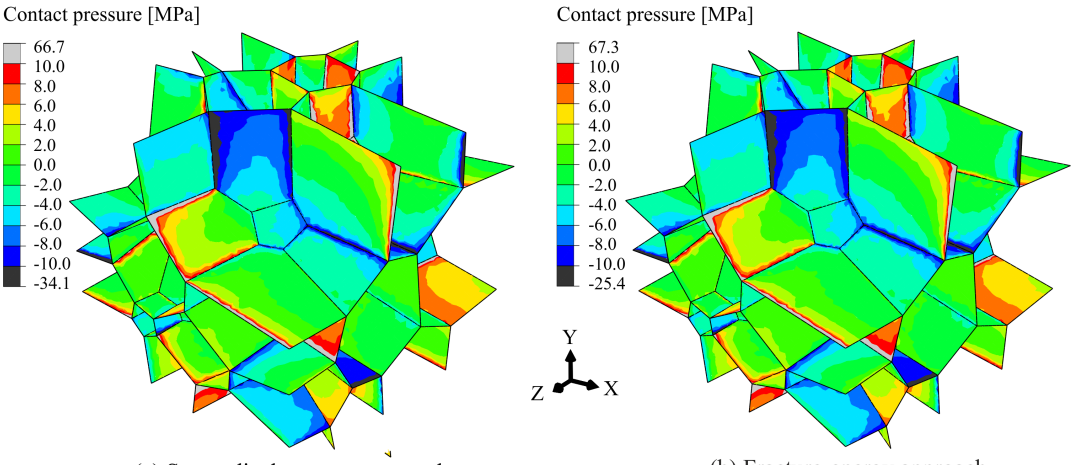

(a) Stress-displacement approach (b) Fracture-energy approach

Figure 3.6. Contoured color plots of contact pressure (MPa) for models with (a) stress-displacement approach in Raghami et al. (2020) ($\boldsymbol{\sigma_y}$ = 25 MPa and η = 100); and (b) fracture-energy approach ($\boldsymbol{\sigma_y}$ = 25 MPa, G = 7 Jm^{-2} and η = 10) at the onset of cracking (ΔT (˚C) = 85 ≅ ΔP (MPa). XYZ represent the coordinate axes.

3.4.2 Case study: estimating the yield strength and fracture toughness of natural quartzite sample

In the following section, firstly observations relevant to grain-boundary fracture initiation and propagation are demonstrated. Secondly, the relative effect of the yield stress $\boldsymbol{\sigma_y}$ and fracture energy (G) on the crack evolution is elucidated. For this objective, 3D models comparable to natural quartz samples in Kruhl et al. (2013) consisting of 30 grains with grain size ranging from 210 to 578 µm and fine mesh subjected to cooling from 300 to 25 °C and decompression from 300 to 22 MPa are employed.

Grain-boundary fracture onset and propagation

Modeling results indicate that there is a power-law relationship between grain size and the temperature and pressure differentials for the onset of (Fig. 3.7). Moreover, these results demonstrate that grain boundary openings begin first at triple lines and grain vertices, where geometric stress concentrations localize, and propagate across the grain faces (Fig. 3.8).

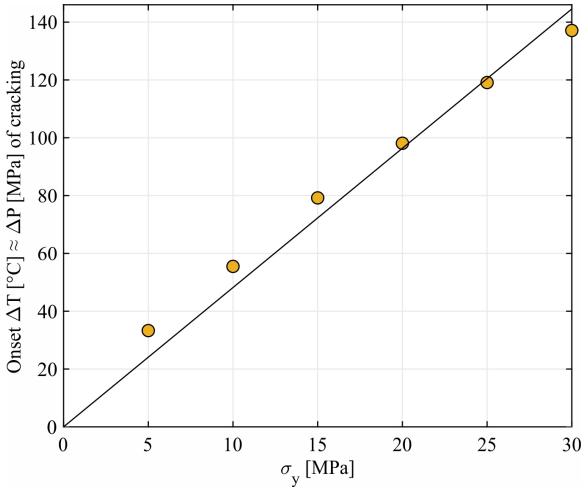

Figure 3.7. 3D modeling results of the effect of yield strength on the onset temperature and pressure of cracking using the fracture-energy approach. Solid black line is a linear fit to group of data for zero intercept.

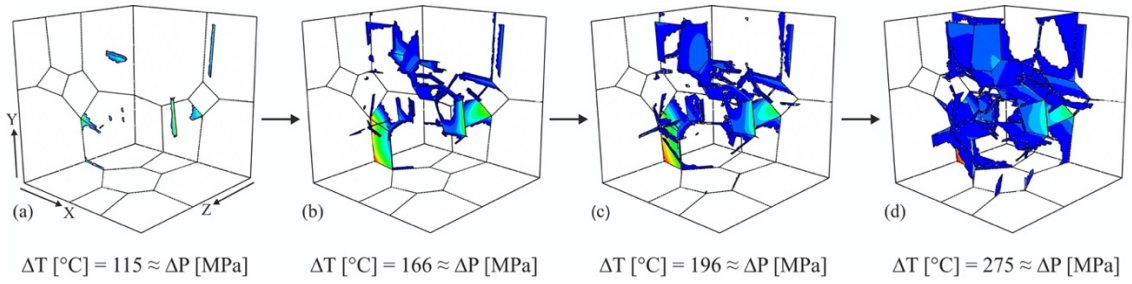

Figure 3.8. Visualization of the evolution of grain-boundary cracks during cooling from 300 to 25 °C and decompression from 300 to 22 MPa for a model with $\boldsymbol{\sigma_y}$ = 15 MPa, η = 10 and G = 7.5 Jm-2. The displayed grain-boundary cracks have a minimum opening of 1.5 nm (complete loss of cohesion has occurred). Color contours denote normal opening displacements, where blue colors show low values and red ones high values.

Parametric study of the effect of yield stress and fracture-energy

The general impact of the fracture-energy and yield stress are examined for models with σ_y (MPa) = [5; 10; 15; 20; 25; 30]; η = 10; and G (Jm^{-2}) = [0.15; 1.5; 7.5; 15]. We examine modeling results for models, which cooled from 300 to 25 °C ($\Delta T = 275^{\circ}C$) and decompressed from 300 to 22 MPa ($\Delta P \cong 278$ MPa). Two specific cases are analyzed: In case 1 the fracture-energy changes according to the range mentioned above and yield strength remains unchanged at 25 MPa (Figs. 3.9a-b); in case 2 the yield strength varies corresponding to the stated range and fracture-energy fixes at 1 Jm^{-2} (Figs. 3.9c-d). It is then followed by summary of results for models subjected to different fracture energies as well as yield strengths (Fig. 3.10).

In the model with σ_y (MPa) = 25 MPa, for all G, a non-linear increase in the grain-boundary crack width beyond the onset of cracking occurs (Fig. 3.9a). An increase in G results in a decrease in the final grain-boundary crack width, ranging from 0.2 µm at G = 0.15 Jm^{-2} to 0.006 µm at G = 15 Jm^{-2}. The sensitivity of the proportion of cracked boundaries to the choice of G is similar to that of grain-boundary crack width (Fig. 3.9b). An increase in G causes a non-linear reduction in the proportion of cracked grain boundaries from 100 % at G = 0.15 Jm^{-2} to 10 % at G = 15 Jm^{-2}.

Concerning the model with G = 1 Jm^{-2}, for all σ_y, a non-linear increase in the grain-boundary crack width beyond the onset of cracking occurs (Fig. 3.9c). An increase in σ_y results in a delay in the onset of cracking and decreases the final grain-boundary crack width, ranging from 0.2 µm at σ_y = 5 MPa to 0.005 µm at σ_y = 30 MPa. The proportion of cracked grain boundaries shows similar sensitivity to the choice of σ_y (Fig. 3.9d). An increase in σ_y gives a non-linear drop in the proportion of cracked grain boundaries, from 100 % at $\sigma_y = 5$ MPa to 15 % at $\sigma_y = 30$ MPa.

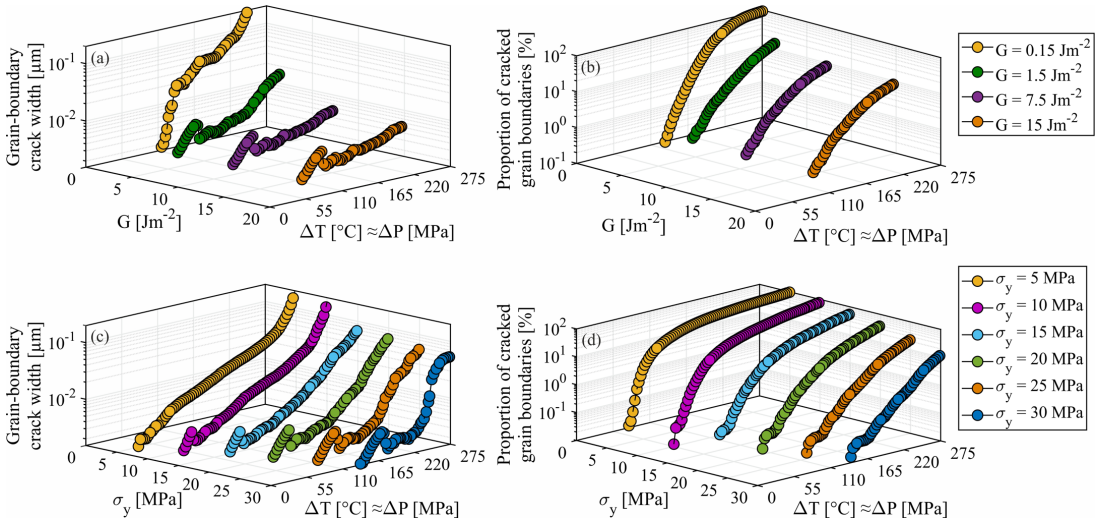

Figure 3.9. 3D modeling results of the effect of fracture energy (G) and yield strength ($\boldsymbol{\sigma_y}$) on quartz grain boundaries over $\Delta T = 275^{\circ}C$ combined with $\Delta P \cong 278$ MPa. In all cases, 30-grain models with grain sizes ranging from 210 to 578 µm and 129 grain boundaries are used. Left column: Evolution of the median of grain-boundary crack width for (a) $\boldsymbol{\sigma_y}$ = 25 MPa, G (Jm^{-2}) = [0.15; 1.5; 7.5; 15] and (c) $\boldsymbol{\sigma_y}$ (MPa) = [5; 10; 15; 20; 25; 30], (G) = 1 Jm^{-2}. Right column: Evolution of the proportion of open grain boundaries for (b) $\boldsymbol{\sigma_y}$ = 25 MPa, G (Jm^{-2}) = [0.15; 1.5; 7.5; 15] and (d) $\boldsymbol{\sigma_y}$ (MPa) = [5; 10; 15; 20; 25; 30], (G) = 1 Jm^{-2}.

The effect of fracture-energy on the evolution of final crack width and the proportion of open grain boundaries are summarized in Fig. 3.10 for yield stresses ranging from 5 to 30 MPa.

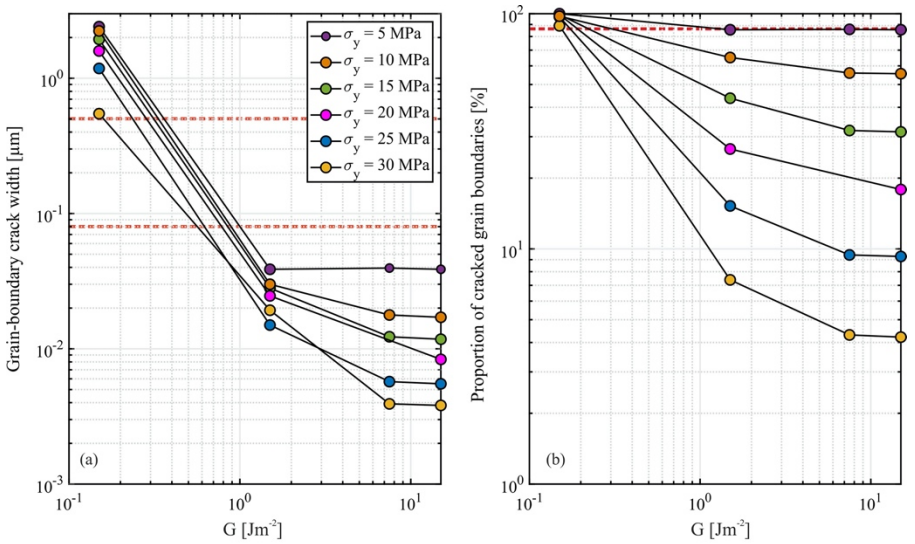

Figure 3.10. Summary of the 3D modeling results of the effect of fracture-energy (G) on quartz grain boundaries with $\boldsymbol{\sigma_y}$ = [5; 10; 15; 20; 25; 30] after ΔT = 275 °C combined with ΔP ≅ 278 MPa. Solid black lines interpolate the points piecewise-linearly. (a) Median of grain-boundary crack width as a function of G. (b) final proportion of open grain boundaries as a function of G. Red lines indicate the possible ranges based on data in Kruhl et al. (2013) and Wirth et al. (2020) (see text).

3.5. Discussion

3.5.1 Performance of fracture-energy approach compared to stress-displacement approach

Modeling of crack tips is intrinsically challenging due to the singularity of stresses and strains at these points (Hutchinson, 1968). Our modeling results indicate that the fracture-energy approach leads to a significant decrease in stresses and strains near the tips of propagating grain boundary cracks and overcomes the overshooting at these points (Fig. 3.3). In contrast, the old approach used in Raghami et al. (2020) demonstrates excess stresses and strains near crack tips, which cause overshooting. Furthermore, the fracture-energy criterion results in a better convergence as long as the viscous regularization is 10 times smaller than before (Fig. 3.4).

Although the alternative approach improves the computation time and convergence problems, the effect of both approaches on final results obtained for width of cracked grain boundaries are roughly the same (Fig. 3.5a). However, in terms of proportion of open grain boundaries, the fracture-energy approach yields a lower percentage of open grain boundaries (Fig. 3.5b). A main reason for this is smaller pressure distribution along grain boundaries (Fig. 3.6b), which can produce fewer open boundaries in the model.

3.5.2 Grain-boundary fracture onset and propagation compared to laboratory observations

In our models, grain-boundary cracks begin at grain vertices and triple junctions (Figs. 3.8a-b), regions of high contact pressure, and propagate across the grain faces (Figs. 3.8c-d), which is consistent with experimental observations (Fredrich and Wong, 1986; Isaka et al., 2018; Kumari et al., 2017). The threshold temperature and pressure of cracking for our specific microstructure displays a linear dependence on the strength of grain boundaries over temperature and pressure gradients of 275 °C and 278 MPa (Fig. 3.7) corresponding to the relation obtained by Raghami et al. (2020). The slight scatter around the linear regression (Fig. 3.7) most likely reflects discretization effects in time (i.e., the finite size of the integration time steps) and the mesh.

3.5.3 Parametric study of the effect of yield stress and fracture-energy compared to nature

Our modeling results lead to various proportions and widths of open grain boundaries. High-resolution TEM studies by Kruhl et al. (2013) and Wirth et al. (2020) on quartz grain boundaries from different metamorphic rocks indicate that not only a large number of the grain boundaries are partially to totally open with crack widths of up to several hundred nanometers but also, although weak, a correlation exists between grain sizes and widths of open boundaries.

In terms of proportion and width of open quartz grain boundaries, Kruhl et al. (2013, Tab. 1) and Wirth et al. (2020) show that on average roughly 87 % of the boundaries are open and the widths of 90 % of them range from 80 to ca. 500 nm. Percentage of open boundaries is based on 33 boundaries with a total length of nearly 300 µm and width of open boundaries is based on 28 measurements. The diameters of ca. 93 %, i.e. 26 from 28, of the grains adjacent to the analyzed boundaries range from 200 to 943 µm. A diameter is taken as average of the two diameters of the neighboring grains. These grain diameters are based on 2D measurements. Among many possible stereological correction factors used to correct the section effect, we use the factor of 1.273, which is estimated by Kong et al. (2005) to convert the 2D size distributions to 3D. This factor shifts the grain diameters presented in Kruhl et al. (2013) and Wirth et al. (2020) from 200-943 µm in 2D to 255-1200 µm in 3D. Considering our 3D model, grain sizes vary between ca. 210 to 578 µm. The intersection of our range of grain sizes with the data on grain sizes, transferred to 3D, and grain boundary crack width reported by Kruhl et al. (2013) and Wirth et al. (2020) yields a probable range of 0.09 to 0.26 µm for width of open grain boundaries (Appendix 3.A, Fig. 3.A.4).

It is difficult to measure the onset temperature for cooling-induced cracking in laboratory experiments or in natural samples. Although many experimental studies investigate crack formation during cooling in rocks with different grain sizes (Browning et al., 2016; Fan et al., 2018; Isaka et al., 2018; Jin et al., 2019; Kumari et al., 2017; Wang et al., 1989; Wu et al., 2019, Zhang et al., 2018), their drawback is that the rock specimens are heated first and then cooled.

Hence, cracks form over both heating and cooling cycles but the temperature interval reported for crack initiation only considers the heating cycles. For example, Johnson et al. (1978) report a threshold temperature of 75 °C for a Westerly granite sample with grain sizes ca. 0.5 mm. This range was measured by acoustic emission for macroscopic cracking process.

The combination of all information provided for widths of cracked grain boundaries (Fig. 3.10a), proportion of open grain boundaries (Fig. 3.10b), and onset temperature of cracking (Fig. 3.7) demonstrates the probable ranges for yield strength and fracture-energy in our specific microstructure: $10 \leq \sigma_y \leq 15$ MPa, $0.3 \leq G \leq 0.9$ Jm^{-2}. As stated by the Griffith's theory of linear fracture mechanics (Griffith and Taylor, 1921), fracture-energy is related to mode-I fracture toughness (K_{IC}) through:

$$K_{IC} = \sqrt{2EG}, \tag{13}$$

where E is Young's modulus. According to Bass 1995, the averaged isotropic Young's modulus of quartz is 95.567 GPa, which results in a range between ca. 0.24 and 0.45 MPam$^{0.5}$ for mode-I fracture toughness of quartz grain boundaries in our model. Compared to Zhang's empirical relation (Fig. 3.1), our modeling results predict smaller values of mode-I fracture toughness for the estimated ranges of yield strength. A main reason for this contradiction is that the mode-I fracture toughness and the yield strength used in Zhang's empirical relation are measured for the macroscopic cracking of whole specimens consist of a large number of grain boundaries with different orientations, different grain sizes and etc. Additionally, fracturing process through laboratory measurements also produces inter- and intra- granular fractures, which together influence the final measured value for mode-I fracture toughness of bulk-sample. Consequently, this relation is invalid for the microscopic yield strength and mode-I fracture toughness of single grain boundaries. Experimental, natural, and other mathematical studies (Brace, 1961; Eberhardt et al., 1999; Fredrich et al., 1990; Li et al., 2017; Peng et al., 2017) imply that the crack initiation is more dependent on the length of grain boundaries and size of intergranular cracks. However, the grain size has a significant effect on controlling the behavior of cracks once they begin to propagate. This will be investigated in our next study.

3.6 Conclusions

In this study, first the performance of a linear fracture-energy criterion directly related to mode-I fracture toughness, is examined for fracture behaviors of exhumation-induced quartz grain boundaries used in our previous study (Raghami et al., 2020). Exhumation occurs over a temperature interval of 275 °C, i.e. from 300 to 25 °C combined with a pressure interval of ca. 278 MPa, i.e. from 300 to 22 MPa. In all 3D models, quartz grains have anisotropic elastic and thermal properties whereas the grain-boundary separation occurs along a linear elastoplastic damage model. The damage model is defined in terms of the energy dissipated due to failure at

grain-boundary scale. 3D models are identical to those used in our previous study (Raghami et al., 2020): 50 grains, 214 grain boundaries, grain size ranging from ca. 3 to 5 mm and constant mesh density within grains and along grain boundaries. The modeling results obtained from fracture-energy approach are then compared to our previous study, which employed an empirical stress-displacement approach for grain-boundary opening (Raghami et al., 2020). The modeling results indicate that the fracture-energy approach is numerically more stable and provides better estimates of contact stresses near the propagating fracture front (Figs. 3.6 -3.7).

We then proceed with a parametric study of exhumation-induced grain-boundary cracking using the fracture-energy to examine the impact of the tensile grain-boundary strength, fracture-energy and fracture toughness. To achieve this aim, 30-grain models with 129 grain boundaries and grain size ranging from 210 to 578 μm are used. On this basis, we conclude the following:

1) The maximum tensile yield stress (σ_y), fracture-energy (G) and fracture toughness (K_{IC}) relevant to the natural quartz grain boundaries are probably between 10 to 15 MPa, 0.3 to 0.9 Jm^{-2} and 0.24 to 0.45 $MPam^{0.5}$, respectively.
2) Overall, an increase in tensile yield stress results in a delay in the onset temperature and pressure intervals of cracking and a decrease of final grain-boundary crack width as well as the proportion of open boundaries. In addition, the results indicate a linear correlation between onset of cracking and yield stress, which is consistent with our previous findings for our specific microstructure (Raghami et al., 2020).
3) Changes in the fracture-energy values have no effect on the onset of cracking but a significant impact on the crack growth.

3.7 Acknowledgements

Funding for the present work was provided by the German Research Foundation (DFG) [grant number KR691/36-1/SCHM930/17-1]. Computational resources used in this work were provided by the eResearch Office, Queensland University of Technology, Brisbane, Australia. E. Raghami gratefully acknowledges the support of Karl Hughes at English Coaching center of Technische Universität München (TUM) in improving the writing skills. Special thanks go to Sebastian Felix Gehrlein at Faculty of Civil, Geo and Environmental Engineering, Technische Universität München (TUM) for providing the software license.

3.8 Appendix

Appendix 3.A

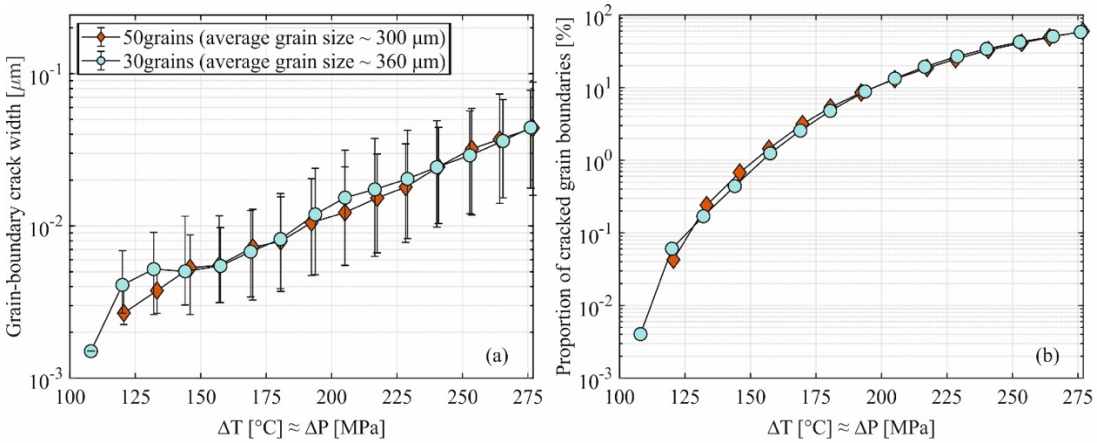

Figure 3.A.1. Modeling results of the evolution of grain-boundary crack width and proportion of open grain boundaries, over cooling from 300 to 25 °C and decompression from 300 to 22 MPa, for 30-grain models with average grain size of 360 µm and 50-grain models with average grain size of 300 µm with $\boldsymbol{\sigma_y}$ = 25 MPa and η = 100. (a) Evolution of grain-boundary crack width. Error bars indicate the 25- and 75-percentiles of the crack-width frequency distribution for all grain-boundary nodes. (b) Evolution of the proportion of open grain boundaries.

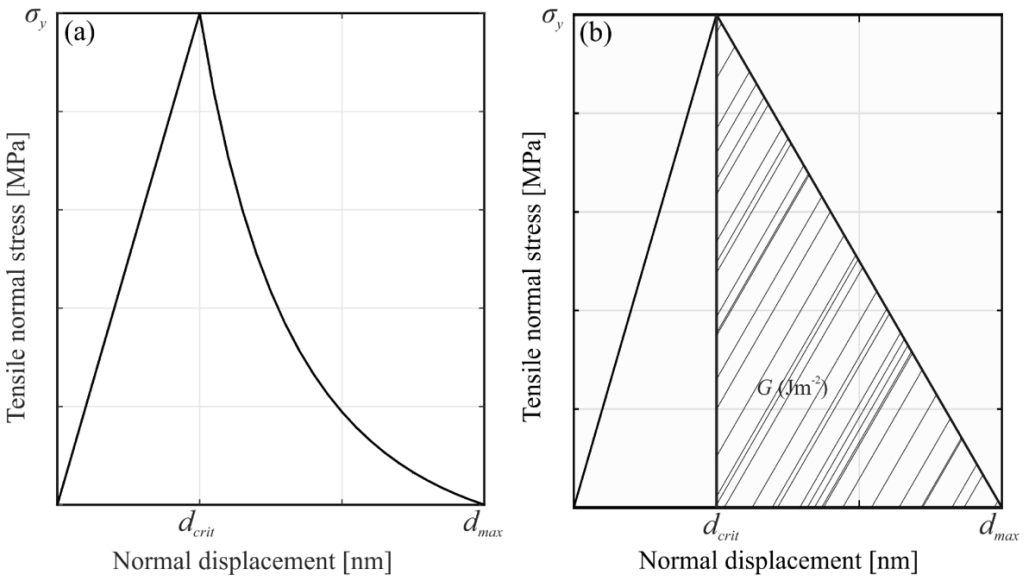

Figure 3.A.2. Tensile normal stress evolution as function of grain-boundary separation distance for damage models with (a) the stress-displacement approach used in Raghami et al. (2020) and (b) the fracture-energy approach. (a) The critical distance for damage onset is 0.5 nm, and the maximum tensile strength is 25 MPa. The maximum separation distance over which tensile stress is transmitted is 1.5 nm. (b) The shaded area corresponds to the fracture-energy dissipated during damage, which is assumed to be 7 Jm^{-2} here. The maximum tensile strength is 25 MPa. The critical distance for damage and the maximum separation distance are calculated automatically by Abaqus based on the fracture-energy value.

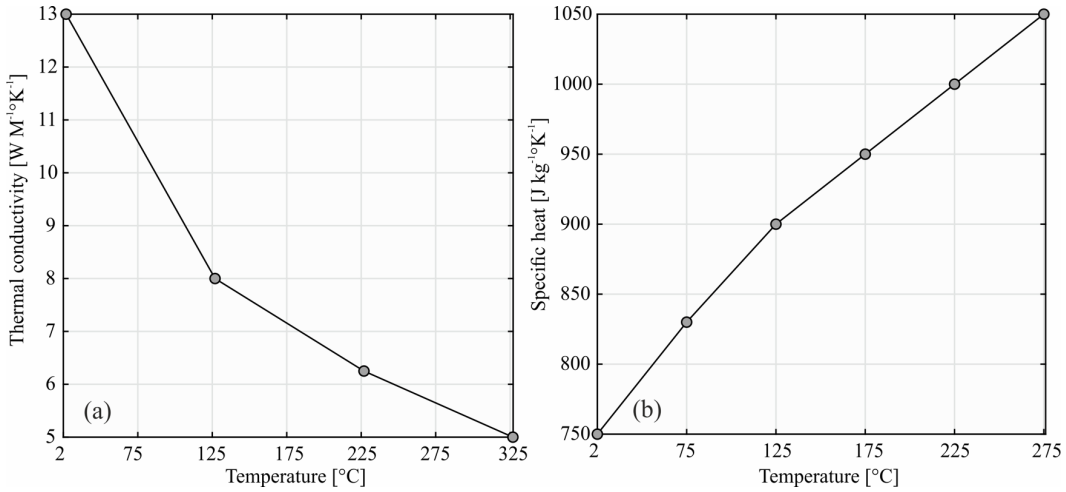

Figure 3.A.3. Temperature-dependent material properties of crystalline quartz used in the 3D simulations. The solid lines are shown for better visibility of the trend. Moreover, Abaqus employs linear interpolation in between tabulated material-property values. (a) Thermal conductivity (from Yoon et al., 2004). (b) Specific heat data are (from Connolly, 2005).

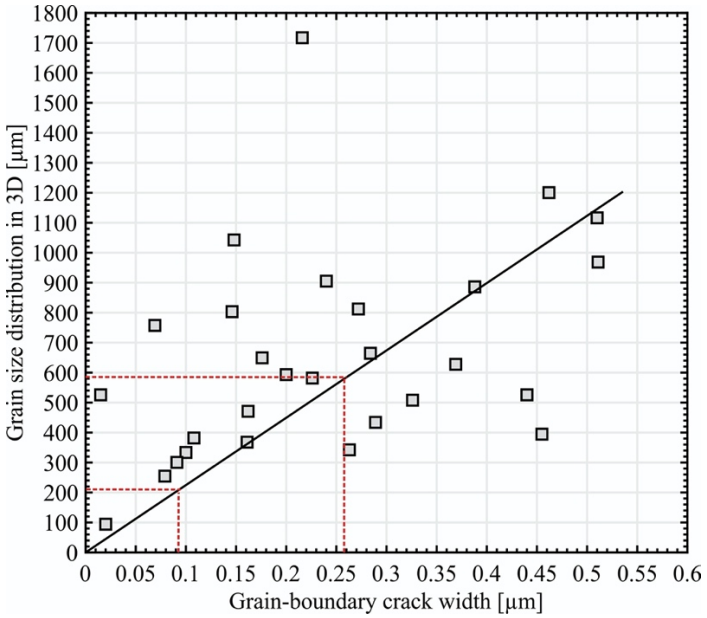

Figure 3.A.4. Correlation between grain sizes and width of open grain boundaries of quartz for data reported by Kruhl et al. (2013) and Wirth et al. (2020). The 2D grain sizes are changed to 3D values by factor 1.273 given in Kong et al. (2005). The solid black line is the linear regression fitted to data for zero intercept. Comparison of grain sizes used in modeling (horizontal red dotted lines) with the correlation of natural grain sizes and crack widths leads to a range of grain boundary crack widths of 0.09 to 0.26 µm.

Chapter 4

Numerical analysis of the effect of grain size on exhumation-induced grain-boundary cracking in quartz grain aggregates

In preparation for submission: Elnaz Raghami, Christoph Schrank, Jörn H. Kruhl: Numerical analysis of the effect of grain size on exhumation-induced grain-boundary cracking in quartz grain aggregates.

The underlying research was designed by Elnaz Raghami, Christoph Schrank, Jörn H. Kruhl. Elnaz Raghami performed the numerical modeling at Queensland University of Technology in Australia and wrote the manuscript. She brought it into its final shape, with comments from the coauthors.

4.1 Abstract

This study investigates the purely geometric influence of grain size on the fracturing response of exhumation-induced quartz grain boundaries with 3D numerical modelling. To achieve this aim, the finite-element method (FEM) combined with contact mechanics is used. Grain boundaries are simulated as contact surfaces between thermal-elastically anisotropic quartz grains, which are randomly orientated. Fracture propagation along grain boundaries is modelled through a linear fracture-energy criterion, which directly relates to mode-I fracture toughness. Eight different average grain sizes are considered: 10, 36, 100, 361, 1000, 1500, 2500, and 3619 μm. Our results demonstrate that the average grain size has a significant effect in controlling the evolution of grain-boundary fractures. In agreement with experimental observations, grain boundaries in models with larger average grain sizes fracture more readily than those in fine-grained models. Final grain-boundary crack width and total proportion of cracked grain-boundary increase none-linearly as a function of the average grain size. In contrast, the critical temperature and pressure difference needed for the onset of cracking show an inverse relationship with the average grain size. Accordance to laboratory observations, the strength of quartz boundaries is inversely related to average grain sizes.

Keywords: Grain size, grain-boundary yield strength, grain-boundary fracture-energy, thermal-elastic anisotropy

4.2 Introduction

Exhumation-related cooling and decompression has been investigated more than four decades (Bruner, 1984; Heard and Page, 1982; Nur and Simmons, 1970; Rosenfeld et al., 1961; Walsh, 1973) because this process can give rise to thermal-elastic micro-cracks in typical crustal rocks. A main reason for formation of thermal-induced micro-cracks is heterogeneous contact stresses arising from contact interaction at grain scale. Temperature and/or external stress changes of rocks as aggregates of mineral grains with different and/or anisotropic thermal expansion as well as elastic properties (Bass, 1995; Skinner, 1966) can cause contact interaction and thus internal stresses at grain scale due to a geometric mismatch between adjacent grains with different and/or anisotropic thermal-expansion coefficients and elastic moduli (Fredrich and Wong, 1986; Johnson et al., 1978; Kranz, 1983). Many researchers have indicated that grain and phase boundaries as predominant sources of thermal-elastic mismatch are preferred sites for crack initiation (Brace et al., 1972; Bombolakis, 1973; Kranz, 1979; Tapponier and Brace, 1976).

It is well established by experimental investigations that the critical stress along grain and phase boundaries for crack initiation and propagation as well as the amount of porosity is highly influenced by grain size (Cordero et al., 2016; Fredrich and Wong, 1986; Fredrich et al., 1990;

Hatzor and Palchik, 1997; Karaka, 2012; Kronenberg and Tullis, 1984; Ogolo et al., 2015). Moreover, experimental studies by Hall (1951) and Petch (1953) predicted that there is an empirical relation between grain-boundary strength (i.e. yield stress at fracture initiation) and grain size in mild metals according to the well-known Hall–Petch relationship:

$$\sigma_y = \sigma_0 + kd^{-1/2} \quad (1)$$

where σ_0 and k are chemistry- and microstructure-dependent constants. In the context of brittle crystalline rocks, extensive experimental evidence suggested that the measured fracture stresses are inversely related to grain size upon uniaxial compressive tests (e.g. Brace, 1961; Hatzor and Palchik, 1997; Fredrich et al., 1990; Wong et al., 1996). They are few experiments monitoring thermal cracks (e.g. Fredrich and Wong, 1986; Johnson et al., 1978). The findings of these studies only demonstrate that the number of resulting micro-cracks are notably influenced by grain size. However, due to the limitation and difficulty in direct observation of fracture initiation and thus inability to investigating the effect of grain size on this process in laboratory (e.g. Baud et al., 2004; Desrues and Viggiani, 2004; Fusseis et al., 2012; Nasseri et al., 2006; Schrank et al., 2012), it is worth employing advanced computational methods. Further drawback of the experimental examinations is their inability to evaluate cooling-induced microcracks initiation because during this examination samples have to be heated first and then cooled, hence the resulting cracks are from both heating and cooling cycles and thus following the crack formation during only cooling is impossible.

To date, various numerical techniques have been developed aiming at simulating the effect of grain size on the crack initiation and evolution (e.g. Li et al., 2017; Saadat and Taheri, 2019; Shushakova et al., 2013; Yu et al., 2018). However, these studies place emphasize on the effect of grain size on micro-crack generation during only heating or only confining pressure. Moreover, owing to the complex microstructure of rocks, these models and techniques mainly focus on crack formation in 2D. To the best our knowledge, there is no 3D modelling study focusing on the exhumation-induced microcracking so far.

The objective of this study is to elucidate the single effect of grain size on the initiation and propagation of grain-boundary cracks in monophase, thermal-elastically anisotropic quartzite induced by exhumation-related cooling and decompression. To achieve this goal, we firstly construct a basic 3D model using foam structure and random orientation of crystallographic axes consist of pure quartzite in a cubic domain with edge-length of 1m. Then we rescale the basic model with various factors to gain 3D models with eight different average grain sizes ranging from 10 to 3619 μm. Afterwards, we combine contact mechanics with the finite-element method to simulate in 3D the grain-scale thermal-elastic cracking of grain boundaries during the exhumation of pure quartzite over a temperature interval of 275 °C, i.e. from 300 to 25 °C, and pressure interval of ca. 278 MPa, i.e. from 300 to 22 MPa. Finally, the purely geometric effect of

grain size on the grain-boundary crack initiation and propagation is analyzed and compared with natural and experimental observations.

4.3 3D numerical modeling: methods

We explore the effect of grain size on the fracture behavior of quartz grain boundaries in 3D grain-scale models. We simulate linear and time-independent exhumation-related temperature and pressure identical to those applied in our previous studies (Raghami et al., 2020, 2021). Decrease of temperature and pressure corresponds to the final portion of the retrograde P-T path of the natural quartzite samples studied by Kruhl et al. (2013): cooling from 300 °C (roughly the "recrystallization temperature" of quartz; Stipp et al., 2002; Voll, 1976) to 25 °C and decompression from 300 to 22 MPa.

4.3.1 3D model generation and analysis

In this study, Neper as a free open-source software package for polycrystal generation and meshing (Quey et al., 2011) was used to simulate 3D grain-scale models. This software implements a grain growth morphological approach to create 3D models with a foam structure (Raghami et al., 2020, 2021), which results in grains with polyhedral shapes, no overlaps and planar boundaries, adequately consistent with the geometric heterogeneity of a quartz microstructure. In order to explore the effect of grain size on the fracture behavior of quartz grain boundaries, eight models including various grain sizes are generated by rescaling of an original model. Thus, all models have the same microstructure (i.e. the grain shapes and other variables are exactly the same). The assumed domain boundary of the original model is a cube composed of pure quartz with the edge length of 1m. This model cube contains 30 discrete deformable grains with random crystallographic orientation and 129 grain boundaries. The scaling factors are assumed to be: [0.000027; 0.0001; 0.00027; 0.001; 0.0027; 0.0042; 0.007; 0.01], therefore the resulting average grain sizes corresponding to each scale factors are approximately 10, 36, 100, 361, 1000, 1500, 2500, and 3619 μm. Each grain boundary in the finite element (FE) is modeled as a contact surface with the zero-initial separation at the onset of analysis.

As in our previous study, the mesh density is defined to be non-uniform, with finer elements along grain boundaries and coarser elements within the grains (Raghami et al., 2021). This type of mesh distribution (Fig. 4.1) is able to enhance the accuracy of results during the fracturing process by increasing the number of nodes along the grain boundaries. The number of mesh element sizes along grain boundaries is ca. 0.45 % of the average grain size whereas the size of these elements is ca. 4 % of the average grain size within the grains. The original model is meshed by 772051 tetrahedral 4-node linear-displacement and linear-temperature elements (C3D4T) with characteristic sizes ranging from ca. 1.65 to 15 μm.

Conservation of mass, of both linear and angular momentum, and of energy are fundamental governing equations in this study. The governing equations are given in our previous studies (Raghami et al., 2020, 2021). In order to solve the governing equations, the Lagrangian FE solver ABAQUS Standard (Hibbitt, Karlsson and Sorenson Inc. ©, 2009), which employs an implicit integration scheme with adaptive time stepping, is used. To solve problems with the simultaneous temperature and displacement fields, coupled temperature-displacement analysis and the large-displacement formulation is used since this formulation has additive strain-rate decomposition and uses Jaumann's stress rate (Jaumann, 1911).

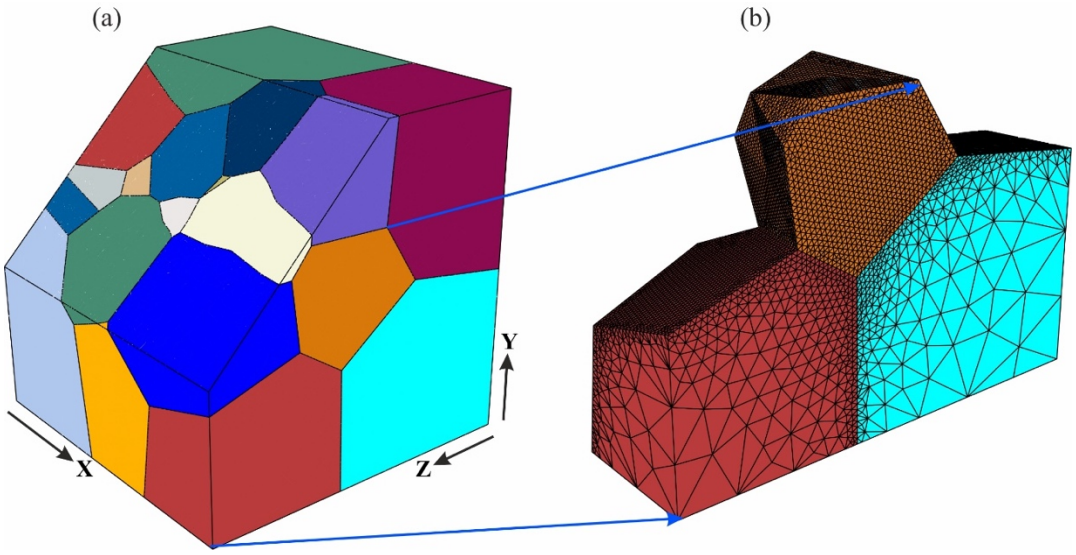

Figure 4.1. (a) Foam microstructure in the 30-grain model with 129 grain boundaries generated in a cubic domain (1 m-edge length). The YZ-plane is cut obliquely to reveal part of the model interior. The average grain size is 0.36 m. Colors mark individual grains. (b) Detailed view of three grains with the non-uniform mesh composed of tetrahedral elements.

4.3.2 Rheological and material properties

Grains

In the present study the used temperature interval is below the recrystallization temperature of quartz (ca. 300 °C), i.e. in the stability field of trigonal α-quartz, where crystal-plastic deformation due to diffusion in quartz and grain boundary migration is ineffective (Stöckhert et al., 1999), and therefore intracrystalline plasticity can be ignored. Additionally, thermoelastic behavior of solid model grains with a fully anisotropic linear-elastic rheology can be explained by the general form of Hook's law (Wang et al., 2018) combined with the thermal strain (Appendix 4.A, Eqs. 4.A.1- 4.A.2).

We simulate grains with the same thermo-elastic properties: anisotropic thermal expansivity with the coefficients α_{11}, $\alpha_{22} = \alpha_{33}$ and elastic stiffness (Appendix 4.A, Table 4.A.2), isotropic temperature-dependent thermal conductivity (Appendix 4.A, Fig. 4.A.1a) and specific heat capacity (Appendix 4.A, Fig. 4.A.1b), and constant density ρ (Appendix 4.A, Table 4.A.2).

Thermal-elastic mismatch is induced by generating randomly oriented crystal lattices from grain to grain, as described in (Raghami et al., 2020).

Grain boundaries

Grain boundaries are simulated as flat contact surfaces between adjoining grains using the node-to-surface contact method with a master-slave approach and the small-sliding approximation proposed in Hibbitt, Karlsson and Sorenson Inc. © (2009). Grain boundaries have identical contact properties in all models as well as no separation at the beginning of analysis. Failure behavior of contact surfaces follows an empirical elastoplastic damage model in tension and shear (Eq. 1).

$$\sigma(d) = \begin{cases} d \le d_{crit} \rightarrow \sigma(d) = K_n d & (a) \\ d > d_{crit} \rightarrow \sigma(d) = \sigma_y\big(1 - D(d)\big) & (b)' \end{cases} \quad (2)$$

where σ is tensile/shear traction, σ_y is tensile/shear yield stress, d is extensional/shear displacement perpendicular/parallel to the grain-boundary segment under consideration, K_n is an elastic modulus with unit Pa/m, and D as a damage parameter has values between 0 and 1. This law is a function of displacement (d). Before critical displacement (d_{crit}), contact stresses across grain boundaries are linear-elastic (Eq. 2a)

We determine onset of failure by a displacement-dependent tensile yield strength, which is reached at the critical displacement d_{crit}. When displacements go beyond d_{crit}, the critical yield strength is reached, and stresses transmitted across the interface decay linearly to zero up to a maximum displacement d_{max}, where complete separation occurs and beyond which no tensile or shear traction are transmitted. The linear decay is modelled via the damage parameter D (Hibbitt, Karlsson and Sorenson Inc. ©, 2009):

$$D(d) = \frac{d(d_{max} - d_{crit})}{d_{max}(d - d_{crit})}, \quad (3)$$

where $d_{max} = \frac{2G}{\sigma_y}$, with G as the fracture-energy at the critical displacement. This damage evolution is consistent with the concept of energy release rate during damage processes to compute the displacement at which full material damage occurs. The relevant material parameters are displayed in Appendix 4.A, Table 4.1.

Here, healing of cracked grain boundaries is ignored. Nevertheless, if in later stages open grain boundaries close again, compressive stresses are transferred in contraction. In addition, if the grain boundaries slide past one another, the relation between shear and normal stress follows a static linear isotropic friction model with a constant friction coefficient μ and zero cohesion. Here, as in our previous studies (Raghami et al., 2020, 2021), a constant value of 0.5 is used in all 3D models. The value of critical displacement (d_{crit}) in our models is 0.5 nm based on natural

measurements of the structural width of intact grain boundaries in a quartzofeldspathic ultramylonite (Hiraga, 1999).

In order to reduce the number of variables and examine only the geometric effect of grain size on the grain-boundary fracture initiation and propagation, we assume that all models have the same yield strength ($\boldsymbol{\sigma_y}$) and fracture-energy (G) at 10 MPa and 7.5 Jm^{-2}, respectively. On the other hand, for the parametric study, σ_y is varied systematically and examined for models with average grain sizes of 36, 361 and 3619 µm. Since our previous study (Raghami et al., 2021) revealed that the onset of cracking is insensitive to choose of fracture-energy, therefore we assume that fracture-energy in all models has a fixed value of 7.5 Jm^{-2}. Besides, according to Zhang (2002), the tensile strength of almost all types of rocks varies between ca. 1 to 23 MPa. This range motivates us to test the ranges, which are summarized in Table 1 for the yield strength of models with average grain sizes of 36, 361 and 3619 µm. The results related to models with average grain size of 361µm are available in our previous study (Raghami et al., 2021).

Table 4.1 Yield strength of quartz grain boundaries used in the parametric study

Average grain size (µm)	σ_y (MPa)
36	1, 3, 5, 10
361	5, 10, 15
3619	10, 15, 20, 25

When grain boundaries are closed, the conductive heat transfer is defined by Fourier's law (Appendix 4.B, Eq. 4.B1). In contrast, if grain boundaries are completely cracked, heat flux, as the rate of energy emission per unit surface crossing the gap between contact surfaces, follows the radiation law (Hibbitt, Karlsson and Sorenson Inc. ©, 2009) (Appendix 4.B, Eq. 4.B2).

4.3.3 Boundary and initial conditions

Boundary and initial conditions are identical with those used in our previous studies Raghami et al. (2020, 2021): Prior to exhumation, the entire model remains at a temperature of 300 °C and a compressive stress of 300 MPa, with zero local differential stress and closed grain boundaries. During cooling and decompression, linear temperature and pressure drops apply to the model from 300 to 25 °C and 300 to 22 MPa, respectively. To avoid model translation, planes corresponding to the Cartesian coordinate system are fixed only in directions perpendicular to each plane.

4.4 Results

In the first and second parts, we present results for average grain sizes (µm) [10, 36, 100, 361, 1000, 1500, 2500, 3619] with fixed σ_y (MPa) = 10 and G (Jm^{-2}) = 7.5 to examine the geometric

effect of grain size alone. In the last results part, we examine the effect of σ_y on the onset of cracking in models with average grain sizes of 36, 361 and 3619 μm and fixed G (Jm^{-2}) = 7.5. The relevant parameters are summarized in Table 4.1.

4.4.1 The effect of grain size on critical temperature and pressure drops for the onset of grain-boundary cracking

An increase in a grain size results in a decrease of the temperature and pressure differentials needed for the onset of grain-boundary cracking (Fig. 4.2). The relationship between average grain size and temperature and pressure intervals of cracking is strongly non-linear up to grain size of 1.5 mm and then remains constant. Moreover, the distribution of cracked grain boundaries in three models with different average grain sizes represents that at the second increment after onset of cracking (Fig. 4.3), models with larger grain sizes experience more tensile stresses along grain boundaries as the model with a smaller average grain size (Appendix 4.C, Fig. 4.C.1). The difference between the number of tensile stresses along grain boundaries lead to opening of entire grain-boundary faces in coarse-grained models (Figs. 4.3b-4.3c) whereas grain boundaries in a fine-grained model start opening at triple lines (Fig.4.3a).

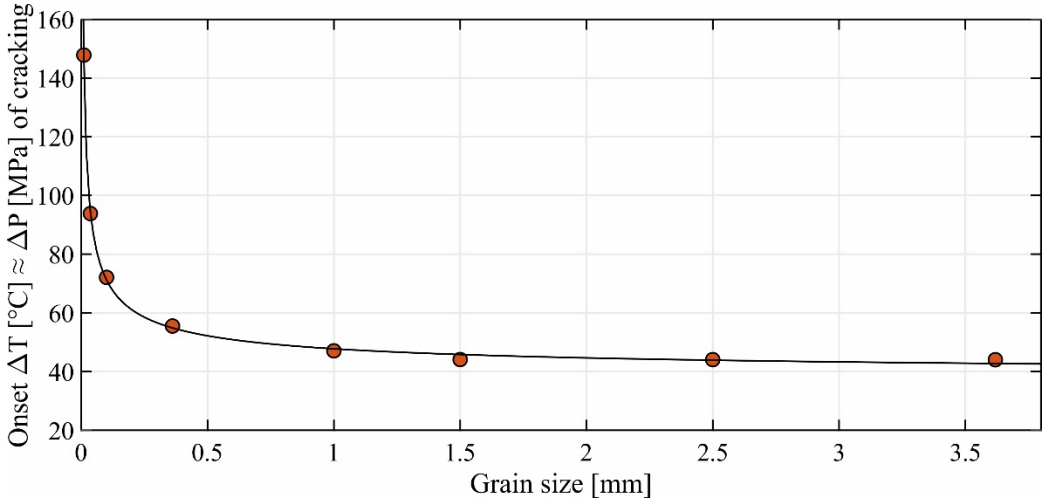

Figure 4.2. A correlation of grain size with the onset temperature and pressure of cracking for quartz grain boundaries. In all cases, σ_y = 10 MPa G = 7.5 Jm^{-2} and η = 10. The solid black line is a power-law fit (f(x) = 37.4 + 360.2 ($x^{-0.5139}$)) to a group of data with R^2 = 0.9993.

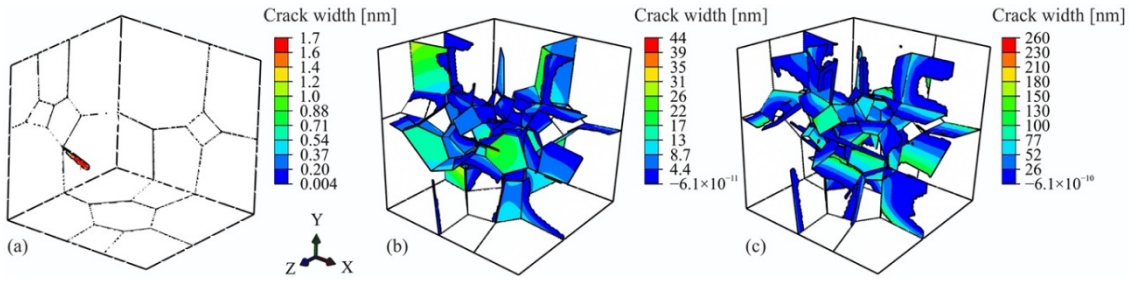

Figure 4.3. Contoured color plots of grain-boundary opening (nm) at the second increment after onset of cracking in models with a grain size difference of a factor 10 (a) 10 μm, ΔT (˚C) = 143 ≅ ΔP (MPa) (b)100

μm, ΔT (˚C) = 66 ≅ ΔP (MPa) and (c) 1000 μm, ΔT (˚C) = 40 ≅ ΔP (MPa). In all cases, $\boldsymbol{\sigma_y}$ = 10 MPa, η = 10 and G = 7.5 Jm^{-2}. X, Y, and Z represent the coordinate axes.

4.4.2 The effect of grain size on the grain-boundary crack evolution

The effect of grain size on the evolution of grain-boundary crack width and the proportion of open grain boundaries is presented in Fig. 4.4. The following ranges for average grain size (μm) are examined: [10, 36, 100, 361, 1000, 1500, 2500, 3619]. Regardless of grain size, there is a non-linear increase in grain-boundary crack width beyond the onset of cracking (Fig. 4.4a). An increase in average grain size results in a non-linear growth in the final grain-boundary crack width ranging from 2.5 μm at average grain size of 3619 μm to 1nm at average grain size of 10 μm. The sensitivity of the proportion of cracked boundaries to the average grain size is similar to that of grain-boundary crack width (Fig. 4.4b). A rise in average grain size causes a non-linear increase in the proportion of cracked grain boundaries, ranging from 90 % at average grain size of 3619 μm to 13 % at average grain size of 10 μm.

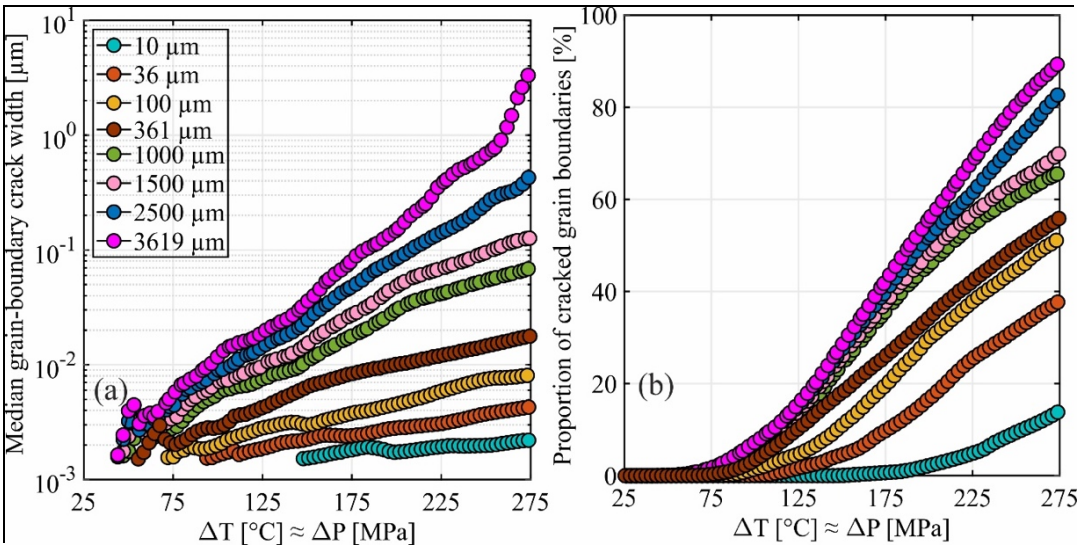

Figure 4.4. Modeling results of the evolution of median grain-boundary crack width and proportion of open grain boundaries, over cooling from 300 to 25 °C and decompression from 300 to 22 MPa, for models with average grain sizes ranging from 10 of 3619 with $\boldsymbol{\sigma_y}$ = 10 MPa G = 7.5 Jm^{-2} and η = 10. (a) Evolution of grain-boundary crack width. (b) Evolution of the proportion of open grain boundaries.

Further examination of grain-boundary crack width and the proportion of cracked grain boundaries after various temperature and pressure differentials present that there is a non-linear correlation (i.e. power law fit) between grain-boundary crack width and the proportion of cracked grain boundaries with grain size (Fig. 4.5). By increasing the P-T intervals, the exponent in the power-fit law grows from 0.6528 at ΔT (°C) = 50 ≅ ΔP (MPa) to 5.483 at ΔT (°C)= 275 ≅ ΔP (MPa).

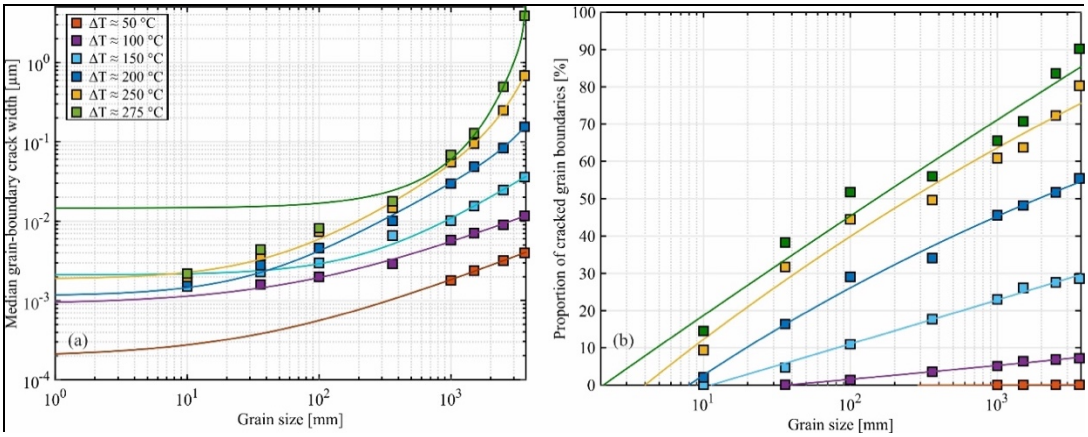

Figure 4.5. Correlation of grain size with (a) the grain-boundary crack width and (b) the proportion of open grain boundaries after different ΔT (°C) ≅ ΔP (MPa) ranging from 50 (red square), 100 (purple square), 150 (light blue square), 200 (dark blue square), 250 (yellow square) and 275 (green square). In all cases, $\boldsymbol{\sigma_y}$ = 10 MPa G = 7.5 Jm^{-2} and η = 10. The solid lines are non-linear fit to a group of data.

4.4.3 The effect of yield stress on the onset of cracking in models with different grain sizes

The general impact of yield stress on the required temperature and pressure of cracking is examined individually in models with different average grain sizes: [36; 361; 3619] μm after total thermal and pressure gradients of ΔT = 275˚C and ΔP ≅ 278 MPa. The results related to models with average grain size of 361μm are taken from our previous study (Raghami et al., 2021). In order to investigate the effect of yield stress alone, we assume that fracture-energy has a fixed value of 7.5 Jm^{-2}.

Modeling results indicate that regardless of grain-size, an increase in the yield stress leads to a rise in the temperature and pressure differentials of crack initiation (Fig. 4.6). Moreover, for models with average grain sizes of 361 and 3619 μm, the onset of cracking is dependent to yield stress linearly. In contrast, in a model with average grain size of 36 μm there is a non-liner relationship between the temperature and pressure differentials for the onset of cracking and yield stress (Fig. 4.6).

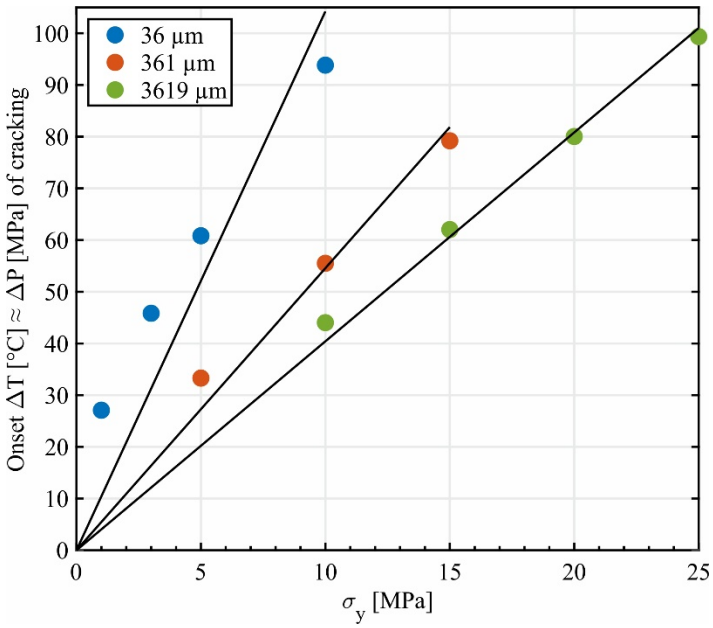

Figure 4.6. 3D modeling results of the effect of yield strength on the onset temperature and pressure of cracking of models with different grain sizes at G = 7.5 Jm^{-2}. 36 µm (blue circles), 361 µm (orange circles) taken from Raghami et al. (2021) and 3619 µm (green circles). Solid black lines show the linear fit to a group of data for zero intercept.

4.5 Discussion

In this section we interpret the geometric effect of grain size on the initiation and evolution of grain-boundary cracking in exhumed-induced quartzite and try to represent how our results compare to experimental observations.

4.5.1 The effect of grain size on the grain-boundary crack initiation

The findings of this study suggest that the geometric heterogeneity resulting from the average grain sizes influences local tensile stresses in the whole model (Appendix 4.C, Fig. 4.C.1). Coarse-grained models experience larger tensile stresses compared to a fine-grained model, which give rise to lower P-T intervals for the microcrack initiation and thus more cracked grain boundaries in models with larger grain sizes compared to the small one (Figs. 4.2-4.3). The empirical correlation between P-T intervals with the average grain size in Fig. (4.2) is:

$$\Delta T \sim \Delta P \propto \frac{1}{d^{\alpha}} \quad , \tag{4}$$

where d is the average grain size and α is a constant value of 0.5139. In addition, it is determined that the average grain size has impact on the strength of grain boundaries at the onset of cracking (Fig. 4.5), which can be written as:

$$\Delta T \sim \Delta P \propto \sigma_y^{\beta} \, , \tag{5}$$

where σ_y is the yield strength of grain boundaries and β is between 0.5 and 1 according to the empirical relationship. The combination of Eqs. (4) and (5) results the below relation:

$$\sigma_y \propto \frac{1}{d^{\gamma}} \quad (6)$$

where $\gamma = \frac{\alpha}{\beta}$, would have an approximate value between 0.5 and 1. The general form of Eq. (6) is in agreement with extensive experimental studies, which observed that an increase in grain size leads to a decrease in the strength (e.g. Brace et al., 1961; Eberhardt et al., 1999; Hatzor and Palchik, 1997; Nalsund and Jensen, 2013; Olsson, 1974; Peng et al., 2017a, 2017b; Wong et al., 1996). However, they reported that the strength is proportional to inverse square root of grain size (i.e. γ = 0.5), which is in our estimated range for γ. They are some possibilities that can change the value of γ. First, most of these studies are designed based on the effect of grain size on the strength of whole rocks, which is summing up of the strength of all boundaries in microscale, under only the uniaxial compressive loading and at constant temperature. In addition, the studied samples are typically composed of micro-cracks and various mineral components, which have major impact on the initiation stress (Lan et al., 2010; Nicksiar and Martin, 2014). Accordingly, their reported relation is invalid for our study, which examine only the purely geometric effect of average grain sizes on the grain-boundary initiation in models consisting of only quartz without any defect such as pores and pre-existing microcracks and relatively homogenous grain size distribution.

4.5.2 The effect of grain size on the grain boundary evolution

Natural observations of Kruhl et al. (2013) and Wirth et al. (2020) on natural quartz samples from various metamorphism conditions indicate that there is a linear correlation between grain size and width of cracked grain boundaries for grain size ranging from ca.200 to 943µm. Since these data are based on 2D measurements, hence we use a stereological correction factor of 1.273, which is estimated by Kong et al. (2005) to convert the 2D size distributions to 3D. This factor shifts the grain diameters presented in Kruhl et al. (2013) and Wirth et al. (2020) from ca. 200-943 µm in 2D to 255-1200 µm in 3D. A comparison between the natural data and our modeling results (Fig. 4.5) demonstrates that this range of grain sizes behaves roughly linearly as a function of crack width in our results, however grain sizes smaller than the natural range evolve non-linearly as a function of crack width.

4.5.3 Our model simplification

In the current study, the geometric effect of average grain sizes is analyzed on the grain-boundary initiation and propagation during exhumation of quartzite, which has no initial micro-cracks and defects. This is certainly not the case in natural materials. Actually, natural samples are generally composed of pre-existing microcracks, porosity, mineral grains with different and anisotropic elastic stiffnesses, different shapes, homogeneous and heterogeneous grain size distribution, etc., which are all micro-structural factors affecting the state of stress in the sample

and thus on the initiation stress of cracking and the evolution of cracking procedure (Hatzor et al., 1997; Lan et al., 2010, 2013; Liu et al., 2018; Peng et al., 2017a; Tang et al., 2000; Wong et al., 1996). A homogeneous specimen has more uniform internal stress distribution and this uniformity leads to higher strength than in a heterogeneous one with different grain properties. More initial microcracks decrease the initial strength of rock and also cause more heterogeneous tensile stress distribution, therefore new microcracks can produce easily. The initial crack length based on the Griffith's theory (Griffith, 1921) has significant impact on the stress required for crack initiation. Although it is possible to implement the crack length and crack width in Abaqus, we ignored the crack length and assumed that all modeled grain boundaries have no defect and vary as a function of grain size because the same properties are assigned to all grain boundaries to only analyze the effect of average grain size.

During studying the effect of grain size in laboratory, at least one or two microstructure properties are available, which cannot be ignored. Additionally, observation of the effect of grain size on the microcracking due to the experimental limitations is impossible. Consequently, the reported results for the effect of grain size on the strength of rock through laboratory tests are based on the macroscopic measurements. Hence, it is reasonable that our results differ from experimental observations. In order to gain better understanding about the effect of each microstructural factors separately and also combined with grain size on the strength of grain boundaries, further studies are required.

4.6 Conclusions

In this study the purely geometric effect of average grain size is investigated on the grain-boundary cracking of exhumed induced quartzite over temperature and pressure drops from 300 ° to 25 °C and 300 to 22 MPa. Failure behaviors of grain boundaries in tension and shear follow a linear fracture-energy criterion, is defined in terms of the energy dissipated due to failure at grain-boundary scale. A basic 3D model consisting of pure quartzite in a cubic domain with edge-length of 1m is rescaled with various factors: [0.000027; 0.0001; 0.00027; 0.001; 0.0027; 0.0042; 0.007; 0.01] to gain 3D models with eight different average grain sizes ranging from 10 to 3619 μm. All models are composed of 30 grains, 129 grain boundaries and non-uniform mesh elements. On this basis, we conclude the following:

1) The required temperature and pressure differentials of cracking is inversely related to grain size and directly related to the yield strength of grain boundaries.
2) Larger average grain sizes give rise larger tensile stresses, which produce more cracked grain boundaries compared to a model with a small average grain size.
3) An increase in the average grain size leads to larger width of open grain boundaries as well as proportion of open grain boundaries.

4) Width of open grain boundaries after temperature and pressure drops of 275 °C and 278 MPa changes non-linearly as a function of grain size. In contrast, proportion of open grain boundaries after the mentioned P-T intervals vary roughly linearly as a function of grain size.
5) The correlation between the P-T intervals of cracking and the yield strength of quartz grain boundaries indicates dependent to the average grain size. For the average grain size larger than ca. 36 μm, the correlation would be linear, while for the average grain size smaller than ca. 36 μm the relationship is non-linear.

4.7 Acknowledgments

Funding for the present work was provided by the German Research Foundation (DFG) [grant number KR691/36-1/SCHM930/17-1]. Computational resources used in this work were provided by the eResearch Office, Queensland University of Technology, Brisbane, Australia. Special thanks go to Sebastian Felix Gehrlein at Faculty of Civil, Geo and Environmental Engineering, Technische Universität München (TUM) for providing the software license.

4.8 Appendices

Appendix A

$$\boldsymbol{\sigma} = \boldsymbol{C}\colon(\boldsymbol{\varepsilon} - \boldsymbol{\varepsilon^{\theta}}), \tag{1}$$

where $\boldsymbol{\sigma}$ is the Cauchy stress tensor, $\boldsymbol{C}$ is the fourth-order stiffness tensor, $\boldsymbol{\varepsilon}$ is the second-order total strain tensor and $\boldsymbol{\varepsilon^{\theta}}$ is the thermal strain, which can be defined based on thermal expansion tensor $\boldsymbol{\beta}$:

$$\boldsymbol{\varepsilon^{\theta}} = \boldsymbol{\beta}(\boldsymbol{T} - \boldsymbol{T_0}), \tag{2}$$

where, T_0 is the reference temperature. Trigonal symmetry of quartz reduces elastic stiffness tensor components to six independent coefficients ($\boldsymbol{C_{11}}$, $\boldsymbol{C_{12}}$, $\boldsymbol{C_{13}}$, $\boldsymbol{C_{14}}$, $\boldsymbol{C_{33}}$, $\boldsymbol{C_{44}}$) (Heyliger et al., 2003).

Table 4.1. Quartz grain-boundary properties

σ_y (MPa)	K_n ($m^{-1}MPa$)	G (Jm^{-2})	d_{crit} (nm)	ζ ($Wm^{-2}K^{-4}$)	e_A, e_B	K ($JK^{-1}m^{-2}s^{-1}$)	F	a
1	1.9×10^{15}	0.15 to 15	0.5	5.67×10^{-8}	0.8	3000	1	1
3	6.02×10^{15}							
5	1.0×10^{16}							
10	2.0×10^{16}							
15	3.0×10^{16}							
20	4.0×10^{16}							

25	5.0×10^{16}							

Table 4.2. Material properties of quartz grains used in 3D models

ρ (Kgm^3)[a]	α_{11} ($°C^{-1}$)[b]	α_{33} ($°C^{-1}$)[b]	C_{11} (GPa)[a]	C_{12} (GPa)[a]	C_{13} (GPa)[a]	C_{14} (GPa)[a]	C_{33} (GPa)[a]	C_{44} (GPa)[a]
2646.6	14×10^{-6}	9×10^{-6}	87.16	6.64	12.09	-18.15	106.00	58.14

[a] From Heyliger et al. (2003)
[b] From Vázquez (2015)

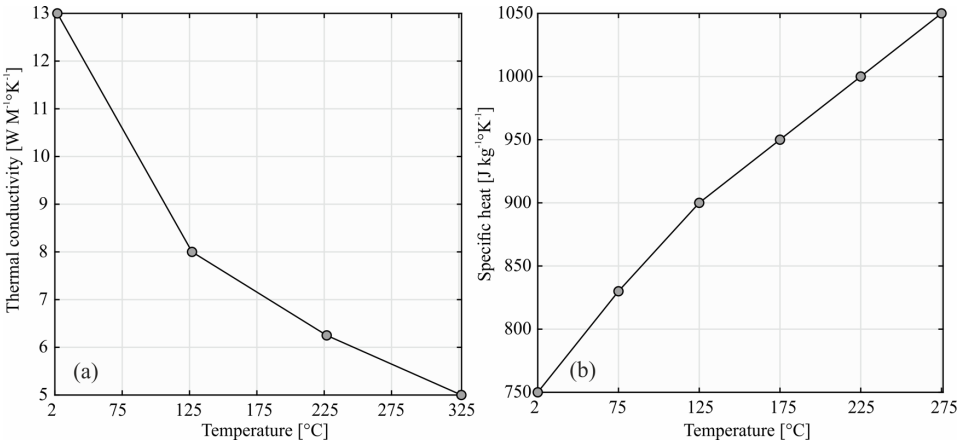

Figure 4.A.1. Temperature-dependent material properties of crystalline quartz used in the 3D simulations. The solid lines are shown for better visibility of the trend. Moreover, Abaqus employs linear interpolation in between tabulated material-property values. (a) Thermal conductivity (from Yoon et al., 2004). (b) Specific heat data are (from Connolly, 2005).

Appendix B

In all models, the conductive heat transfer between closed contact surfaces is defined by Fourier's law:

$$\boldsymbol{q = -K(T_A - T_B)}, \tag{1}$$

where K is the grain boundary conductance. With progressive grain-boundary fracturing, K decreases linearly as a function of normal distance between adjacent grain boundaries and assumes that the value of K drops to zero after 1 μm. If grain boundaries are completely cracked, heat flux (q), as the rate of energy emission per unit surface crossing the gap between contact surfaces, follows the radiation law (Hibbitt, Karlsson and Sorenson Inc. ©, 2009):

$$\boldsymbol{q = H[(T_A - T_0)^4 - (T_B - T_0)^4]}, \tag{2}$$

where T_A and T_B denote the temperatures of the adjacent cracked grain surfaces, T_0 is the absolute zero on the used temperature scale, and the coefficient H is given by:

$$\boldsymbol{H = \frac{F\zeta}{\frac{1}{e_A}+\frac{1}{e_B}-1}}, \tag{3}$$

where ζ is the Stefan-Boltzmann constant, F is the effective view factor, and e_A and e_B are the emissivities of the adjacent grain surfaces. All parameters are summarized in Appendix A, Table 4.A.1.

Appendix C

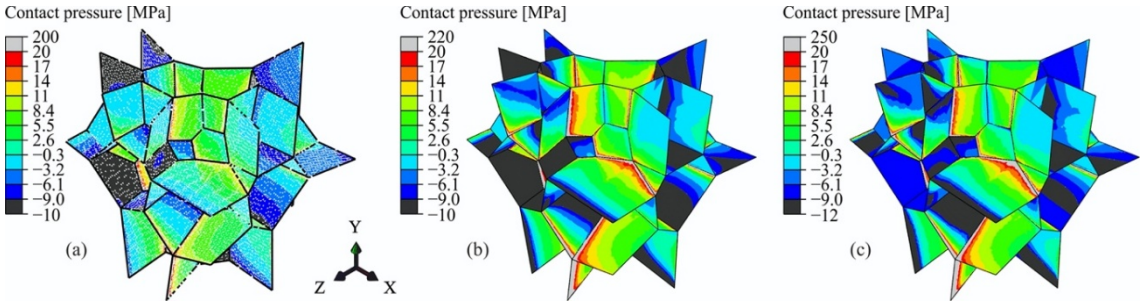

Figure 4.C.1. Contoured color plots of contact pressure (MPa) at the second increment after onset of cracking in models with a grain size difference of a factor 10 (a) 10 µm, ΔT (˚C) = 143 ≅ ΔP (MPa) (b)100 µm, ΔT (˚C) = 66 ≅ ΔP (MPa) and (c) 1000 µm, ΔT (˚C) = 40 ≅ ΔP (MPa). In all cases, $\boldsymbol{\sigma_y}$ = 10 MPa, η = 10 and G = 7.5 Jm^{-2}. X, Y, and Z represent the coordinate axes.

Chapter 5
Synthesis and Discussion

This study aims to contribute to a number of topics in relation to quartz grain-boundary fracturing induced by exhumation-related cooling and decompression during a typical exhumation P-T path in the continental crust (i.e. exhumation from a depth of ca. 11 to 1 km along a geothermal gradient of ca. 27 °C km^{-1}). These topics are fully stated in chapter one include:

1) After which typical temperature and pressure decreases do grain-boundary cracks begin to form?
2) How do grain-boundary openings evolve in terms of their geometry (width, length, from vertices over triple lines to grain faces)?
3) How much of the proportion of grain boundaries crack along the exhumation path?
4) How can we best model grain-boundary cracks numerically for 3D anisotropic microfabrics in terms of their grain-boundary mechanical properties?
5) What are the relevant mechanical properties of quartz grain boundaries?
6) How does grain size affect the required differential temperature and pressure for grain-boundary cracking and the proportion of cracked grain boundaries?

The above mentioned questions were raised because the most interesting aspect in relation to thermally induced microcracks is their effect on the physical properties of rocks such as elasticity, strength, fracture toughness, thermal conductivity, and permeability (e.g. Darling et al., 2013; Feng et al., 2019; Kruhl et al., 2013; Nasseri et al., 2009a; Pimienta et al., 2018), which are major factors in the context resource extraction (e.g., mining, quarrying, and drilling), nuclear waste disposal, and reservoir stimulation (Heard and Page, 1982; Nasseri et al., 2007).

The main focus of this study is on quartz because it is one of the most abundant rock-forming minerals in the Earth's continental crust (ca. 12.6 wt %) (Götze, 2018) and, like nearly all rock-forming minerals, exhibits anisotropic thermal and elastic behavior during temperature and pressure changes. Therefore, it is expected that, overall outcome of this study would have broad applicability for the impact of exhumation on the physical properties of other rock types.

I addressed these topics through employing 3D numerical modeling, presented in chapters two, three and four of this dissertation. In detail, the fracturing of quartz grain boundaries during exhumation of quartzite was simulated with contact mechanics combined with the finite-element method. In these models, grains had an anisotropic linear-elastic rheology and an anisotropic thermal-expansion tensor. Moreover, grain boundaries were modeled as contact surfaces with a

strain-softening rheology. According to the analysis of these issues, key findings and their implications are summed up subsequently as follows.

5.1 Summary and implications

After which typical temperature and pressure decreases do grain-boundary cracks begin to form?

This was investigated in chapter 4 that the required differential temperature and pressure for onset of cracking is a function of yield strength and grain size. If the average grain size has a value smaller than ca. 36 μm, there is a non-linear correlation between P-T intervals of cracking and the yield strength while for average grain sizes more than ca. 36 μm, these two factors are linearly dependent. Besides, the relationship between average grain size and P-T intervals of cracking is strongly non-linear up to grain size of 1.5 mm and then remains constant. In addition to the mentioned results, P-T intervals of grain-boundary cracking showed insensitivity to the magnitudes of pressure and temperature differentials during exhumation (chapter 2). However, these findings differ from those obtained by Bruner (1984) from modeling of fracturing induced during the cooling and stress relaxation associated with unroofing of granite intrusions, which implied that cooling-induced internal stresses should most commonly play the dominant role in thermal-elastic cracking. The effective factors in this inconsistency could have been the microstructure properties (e.g. grain size, variability of grain shape, mineral grains, pre-existing defects in the form of cracks). These features have a major impact on local stresses in particular in 3D and in the absence of cracks (Picu and Gupta, 1997), which were not accounted by Bruner (1984). Moreover, the stress heterogeneity resulting from different microstructure properties can significantly influence the crack initiation and propagation even when rocks are only subject to pressure changes (Blair and Cook, 1998a; 1998b; Gallagher et al., 1974; Lan et al., 2010; Liu et al., 2018; Peng et al., 2017a). As an example, this topic is critical in evaluating the mechanical properties of the bedrock for storage of deep underground geological disposal of nuclear waste. Bedrocks are typically constructed from crystalline rocks and clay soils with negligible permeability and low porosity, which have geological conditions (Brook et al., 2014; Fairhurst, 2004). Nuclear wastes generate heat, and the cooling of bedrock is done by injection of water. The cooling process and rate of cooling change the porosity and permeability of reservoir due to formation of thermally-induced microcracks (Isaka et al., 2018). Hence, in order to prevent or control micro-cracks formation in bedrock, the modeling results demonstrated that the amount of differential temperature during cooling procedure should be smaller than the required temperature and pressure gradients for micro-crack initiation, which is related to grain size and yield strength of the bedrock. Therefore, understanding the effect of each microstructure properties on the crack initiation and propagation in bedrock allows the safe nuclear waste storage and might contribute to analyses in the future studies.

How do grain-boundary openings evolve in terms of their geometry (width, length, from vertices over triple lines to grain faces)?

In terms of the geometric evolution of grain-boundary fracturing, regardless of the fracture approach employed in grain-boundary failure, grain-boundary cracks initiate at grain vertices and triple junctions, which are effective areas in creation of geometrical stress concentration and then propagate across the grain faces (chapters 2 and 3). This observation is in agreement with grain-boundary crack initiation and evolution in natural observations (Mancktelow and Pennacchioni, 2004) and experiments (Feng et al., 2016; Fredrich and Wong, 1986; Isaka et al., 2018; Kumari et al., 2017). These laboratory observations showed that grain-boundary cracking initiates at triple junction and continues until facing another triple line junction, at which time crack.

How much of the proportion of grain boundaries crack along the exhumation path?

The findings reveal that this value is also strongly related to both yield strength of grain boundaries and the average grain size (chapters 2 and 4). Overall, at least more than 55 % (for grain sizes ranging from ca. 3 to 5 mm) to roughly 90 % (for grain sizes ranging from ca. 200 to 600 μm) of grain boundaries are open. The range obtained for the proportion of open grain boundaries is broader than one which was observed by Wirth et al. (2020) on natural quartzitic rocks. These researchers indicated that nearly 90 % of grain boundaries are open. It is predicted that in addition to grain size, the variation of grain shape has significant effect on the crack stress initiation and thus the final open boundaries (Han et al., 2019; Liu et al., 2018). Consequently, it could be beneficial to investigate the geometric effect of grain shape separately and also combined with grain size on the strength of grain boundaries and cracking process.

How can we best model grain-boundary cracks numerically for 3D anisotropic microfabrics in terms of their grain-boundary mechanical properties? What are the relevant mechanical properties of quartz grain boundaries?

For all 3D simulations in this work, the commercial finite element code (FE) Abaqus standard (Hibbitt, Karlsson and Sorensen Inc.©, 2009) combined with contact mechanics was used. This is the most widely adopted method to simulate discontinuities in continuum mechanics using the strain-softening model (Wang et al., 2017). The application of a non-linear strain-softening rheology in tension and a Mohr-Coulomb rheology in shear (i.e. stress-displacement approach) in modelling the failure behavior of grain boundaries, is successful to estimate a value of 75 MPa for the upper bound of yield strength of quartz grain boundaries, with the best-fit results for σ_y = 25 MPa in models containing quartz grains ranging from 3 to 5mm (chapter 2). Although the stress-displacement criterion was simulated the state of stress within the bulk of individual model grains quite well (chapter 2), some singularities was observed in computation of stress and strain near the tips of grain-boundary cracks and at sharp corners (chapter 2). The best solution for this

issue was mesh refinement and the application of fracture-energy approach (chapter 3). A parametric study of exhumation-induced quartz grain-boundary cracking using fracture-energy criterion in 3D models consisting of grain sizes comparable to natural samples (Kruhl et al., 2013; Wirth et al., 2020) (i.e. ca. 200 to 600 µm), was successful to approximate a range for the maximum tensile yield stress (σ_y), fracture-energy (G) and mode-I fracture toughness (K_{IC}) relevant to the natural quartz grain boundaries, respectively: 10 to 15 MPa, 0.3 to 0.9 Jm^{-2} and 0.24 to 0.45 $MPam^{0.5}$ (chapter 3). However, the modeling results predicted smaller values of mode-I fracture toughness for the estimated ranges of yield strength compared to the value measured by Zhang, (2002). Because values reported for these parameters are related to the macroscopic cracking of whole specimens consist of a large number of grain boundaries with different orientations, different grain sizes and grain shape, differential mineral components and defects such as pre-existing microcracks. Accordingly, the Zhang's empirical relationship is not valid for microscopic yield strength and mode-I fracture toughness. As a result, the above-mentioned findings obviously display the dependence of mechanical properties of quartz grain boundaries on microstructure properties. The detection of microcrack initiation specifically during cooling has many limitations in laboratory because samples should be heated first and then cooled. Besides, examination of the effect of some microstructure properties such as grain size and grain shape on the strength of grain boundaries is rare or only related to macroscale. Hence, further numerical analyses on the effect of microstructure properties on the grain-boundary cracking could provide a complete picture of thermal cracking mechanism, which is important in energy resources applications in geothermal energy recovery (e.g., Fehler, 1981; Pearson et al., 1983) and nuclear waste disposal (e. g., Wang et al., 1981).

How does grain size affect the required differential temperature and pressure for grain-boundary cracking and the proportion of cracked grain boundaries?

As stated earlier, temperature and pressure intervals of cracking showed dependence on the yield strength and the average grain size. A coarse-grained model produces higher tensile stresses along grain boundaries compared to a fine-grained model, which in turn leads to crack initiation after smaller P-T intervals and causes larger crack width and proportion of cracked grain boundaries. Width of open grain boundaries as well as the proportion of open grain boundaries increases non-linearly as a function of grain size (chapter 4). This finding that the width of open grain boundaries is related to the grain size is in agreement with the outcome of Kruhl et al. (2013). Furthermore, it was explored by modeling the yield strength of quartz grain boundaries in models with various average grain sizes could be as low as ca. 5 MPa (chapter 4). Now the main question is that is it possible to have quartz grain boundaries with yield strengths as low as 1 MPa in nature?

Seismic studies from the Kola and KTB scientific boreholes (Smithson et al., 2000) discovered the presence of fluid-filled fractures and microcracks through the upper crust. Moreover, many laboratory tests have been conducted to evaluate the effect of water on the strength of different rock types (e.g. Dyke and Dobereiner, 1991; Simpson et al., 1968; Vasarhelyi and Van, 2006; Wong et al., 2016). These studies demonstrated the weakening effect of water on the strength of rocks. Consequently, it seems possible to have the yield strength as low as 1 to 5 MPa for the quartz grain-boundary. Although several water-weakening mechanisms have been conducted, it still appears that there is no well-proven explanation which is universally acceptable to report the influence of water on rock strengths, probably owing to the wide range of rock types (Eeckhout, 1976). According to inconsistent findings mentioned above, to investigate the effect of fluid on the strength of rocks, future studies using 3D models can take fluid-filled boundaries into consideration.

Simplifications of 3D models

All grain boundaries in this study were modeled as flat surfaces and all grains had random orientations. However, this is not the exact case in natural materials. The strength of natural grain boundaries depends on many parameters such as composition of adjacent crystal lattices (Kohyama, 2002; Meyers and Ardell, 1993), lattice-scale defects (Valiev et al., 1986), and the presence of secondary minerals (Kanaori et al., 1991; Savanick and Johnson, 1974), grain shape and grain size distribution (Shushakova et al., 2011, 2013). Furthermore, other researchers (e.g. Siegesmund et al., 2000; Grelk et al., 2004) indicated that interlobate or seriate grain boundaries reflect higher binding energy between grain boundaries than simple ones. In addition to the stated simplifications, since the aim of this study was to investigate the grain-boundary fracture, so that the inelastic low-temperature deformation of quartz (Groshong, 1988) neglected in the studied temperature regime (i.e. cooling from 300 to 25 °C). Consequently, it is crucial to conduct further studies on understanding the effect of these properties on the material properties of grain boundaries and thus the microcrack formation and the P-T intervals of crack initiation.

In summary, 3D simulation of grain-boundary cracking during the exhumation of pure quartzite (i.e. cooling from 300 to 25 °C and decompression from 300 to 22 MPa) indicated that grain-boundary cracking initiates after specific temperature and pressure intervals below the recrystallisation temperature of quartz (i.e. ca. 300°C). These intervals are strongly related to average grain size and yield strength of grain boundaries. Additionally, the proposed numerical approaches in this research provided an opportunity to assess the advantages and limitations of modeling approaches in characterizing the grain-boundary cracking. Moreover, this study was successful in estimating the material properties of quartz grain boundaries as a function of grain size such as yield strength, fracture-energy and mode-I fracture toughness. The last but not the least, this study showed how geometric heterogeneity resulting from grain size distribution can

influence the proportion of cracked grain boundaries, width of open grain boundaries and P-T intervals of cracking.

Bibliography

Abdelaziz, A., Zhao, Q., & Grasselli, G. (2018). Grain based modelling of rocks using the combined finite-discrete element method. Computers and Geotechnics, 103, 73-81. doi:10.1016/j.compgeo.2018.07.003

Bass, J. D. (1995). Elasticity of Minerals, Glasses, and Melts. In T. J. Ahrens (Ed.), Mineral Physics and Crystallography: A Handbook of Physical Constants (pp. 45-63). Washington, DC: American Geophysical Union.

Baud, P., Klein, E., & Wong, T.-f. (2004). Compaction localization in porous sandstones: spatial evolution of damage and acoustic emission activity. Journal of Structural Geology, 26(4), 603-624. doi:10.1016/j.jsg.2003.09.002

Becker, R., & Panchanadeeswaran, S. (1995). Effects of grain interactions on deformation and local texture in polycrystals. Acta Metallurgica et Materialia, 43(7), 2701-2719. doi:10.1016/0956-7151(94)00460-Y

Behrmann, J. H. (1985). Crystal plasticity and superplasticity in quartzite: a natural example. Tectonophysics, 115(1-2), 101-129. doi:10.1016/0040-1951(85)90102-7

Bhagat, R. B. (1985). Mode I fracture toughness of coal. International Journal of Mining Engineering 3, 229-236. doi:10.1007/BF00880769

Blacic, J. D. (1975). Plastic-deformation mechanics in quartz: the effect of water. Tectonophysics 27 (3), 271–294. doi:10.1016/0040-1951(75)90021-9

Blacic, J. D., & Christie, J. M. (1984). Plasticity and hydrolytic weakening of quartz single crystals. Journal of Geophysical Research: Solid Earth, 89(B6), 4223-4239. doi:10.1029/JB089iB06p04223

Blair, S. C., & Cook, N. G. W. (1998a). Analysis of compressive fracture in rock using statistical techniques: Part I. A non-linear rule-based model. International Journal of Rock Mechanics and Mining Sciences, 35(7), 837-848. doi:10.1016/S0148-9062(98)00008-4

Blair, S. C., & Cook, N. G. W. (1998b). Analysis of compressive fracture in rock using statistical techniques: Part II. Effect of microscale heterogeneity on macroscopic deformation. International Journal of Rock Mechanics and Mining Sciences, 35(7), 849-861. doi:10.1016/S0148-9062(98)00009-6

Bombolakis, E. G. (1973). Study of the brittle fracture process under uniaxial compression. 18(3-4), 231-248. doi:10.1016/0040-1951(73)90048-6

Bons, A. J., Drury, M. R., Schryvers, D., & Zwart, H. J. (1990). The nature of grain boundaries in slates implications for mass transport and processes during low temperature metamorphism. Physics and Chemistry of Minerals, 17(5), 402-408. doi:10. 1007/BF00212208.

Brace, W. F. (1961). Dependence of Fracture Strength of Rocks on Grain Size. Paper presented at the 4th U.S. Symposium on Rock Mechanics (USRMS), University Park, Pennsylvania.

Brace, W. F., Silver, E., Hadley, K., & Goetze, C. (1972). Cracks and Pores: A Closer Look. Science, 178(4057), 162-164. doi:10.1126/science.178.4057.162

Brace, W. F., & Walsh, J. B. (1962). Some direct measurements of the surface energy of quartz and orthoclase. The American Mineralogist, 47 (9-10), 1111-1122.

Brook, B. W., Alonso, A., Meneley, D. A., Misak, J., Blees, T., & van Erp, J. B. (2014). Why nuclear energy is sustainable and has to be part of the energy mix. Sustainable Materials and Technologies, 1-2, 8-16. doi:10.1016/j.susmat.2014.11.001

Browning, J., Meredith, P., & Gudmundsson, A. (2016). Cooling-dominated cracking in thermally stressed volcanic rocks. Geophysical Research Letters, 43(16), 8417-8425. doi:10.1002/2016gl070532

Bruner, W. M. (1979). Crack growth and the thermoelastic behavior of rocks. Journal of Geophysical Research, 84(B10). doi:10.1029/JB084iB10p05578

Bruner, W. M. (1984). Crack growth during unroofing of crustal rocks: Effects on thermoelastic behavior and near-surface stresses. Journal of Geophysical Research: Solid Earth, 89(B6), 4167-4184. doi:10.1029/JB089iB06p04167

Canova, G. R., Wenk, H. R., & Molinari, A. (1992). Deformation modelling of multi-phase polycrystals case of a quartz-mica aggregate. Acta Metallurgica et Materialia, 40(7), 1519-1530. doi:10.1016/0956-7151(92)90095-V

Cardozo, N., & Allmendinger, R. W. (2013). Spherical projections with OSXStereonet. Computers & Geosciences, 51, 193-205. doi:10.1016/j.cageo.2012.07.021

Chen, S., Yang, C., & Wang, G. (2017). Evolution of thermal damage and permeability of Beishan granite. Applied Thermal Engineering, 110, 1533-1542. doi:10.1016/j.applthermaleng.2016.09.075

Connolly, J. A. D. (2005). Computation of phase equilibria by linear programming: A tool for geodynamic modeling and its application to subduction zone decarbonation. Earth and Planetary Science Letters, 236(1-2), 524-541. doi:10.1016/j.epsl.2005.04.033

Cordero, Z. C., Knight, B. E., & Schuh, C. A. (2016). Six decades of the Hall–Petch effect – a survey of grain-size strengthening studies on pure metals. International Materials Reviews, 61(8), 495-512. doi:10.1080/09506608.2016.1191808

Darling, T. W., & Struble, W. (2013). Temperature dependent elasticity and damping in dehydrated sandstone. https://ui.adsabs.harvard.edu/abs/2013AGUFMMR13A2270D

Darot, M., Gueguen, Y., & Baratin, M.-L. (1992). Permeability of thermally cracked granite. Geophysical Research Letters, 19, 869-872. doi:10.1029/92GL00579

Darot, M., Gueguen, Y., Benchemam, Z., & Gaboriaud, R. (1985). Ductile-brittle transition investigated by micro-indentation: results for quartz and olivine. Physics of the Earth and Planetary Interiors, 40(3), 180-186. doi:10.1016/0031-9201(85)90128-1

De Borst, R., Sluys, L. J., Muhlhaus, H. B., & Pamin, J. (1993). Fundamental Issues in Finite Element Analyses of Localization of Deformation. Engineering Computations, 10(2), 99-121. doi:10.1108/eb023897

Desrues, J., & Viggiani, G. (2004). Strain localization in sand: an overview of the experimental results obtained in Grenoble using stereophotogrammetry. International Journal for Numerical and Analytical Methods in Geomechanics, 28(4), 279-321. doi:10.1002/nag.338

Durham, W. B., & Abey, A. E. (1981). The effect of pressure and temperature on the thermal properties of a salt and a quartz monzonite. Paper presented at the 22nd U.S. Symposium on Rock Mechanics, Cambridge, Massachusetts.

Dutler, N., Nejati, M., Valley, B., Amann, F., & Molinari, G. (2018). On the link between fracture toughness, tensile strength, and fracture process zone in anisotropic rocks. Engineering Fracture Mechanics, 201, 56-79. doi:10.1016/j.engfracmech.2018.08.017

Dyke, C. G., & Dobereiner, L. (1991). Evaluating the strength and deformability of sandstones. Quarterly Journal of Engineering Geology and Hydrogeology, 24(1), 123-134. doi:10.1144/gsl.Qjeg.1991.024.01.13

Eberhardt, E., Stimpson, B., & Stead, D. (1999). Effects of Grain Size on the Initiation and Propagation Thresholds of Stress-induced Brittle Fractures. Rock Mechanics and Rock Engineering, 32(2), 81-99. doi:10.1007/s006030050026

Eeckhout, E. (1976). The mechanisms of strength reduction due to moisture in coal mine shales. International Journal of Rock Mechanics and Mining Sciences & Geomechanics Abstracts, 13, 61-67.

Fairhurst, C. (2004). Nuclear waste disposal and rock mechanics: contributions of the Underground Research Laboratory (URL), Pinawa, Manitoba, Canada. International Journal of Rock Mechanics and Mining Sciences, 41(8), 1221-1227. doi:10.1016/j.ijrmms.2004.09.001

Fan, L. F., Gao, J. W., Wu, Z. J., Yang, S. Q., & Ma, G. W. (2018). An investigation of thermal effects on micro-properties of granite by X-ray CT technique. Applied Thermal Engineering, 140, 505-519. doi:10.1016/j.applthermaleng.2018.05.074

Fan, L. F., Wu, Z. J., Wan, Z., & Gao, J. W. (2017). Experimental investigation of thermal effects on dynamic behavior of granite. Applied Thermal Engineering, 125, 94-103. doi:10.1016/j.applthermaleng.2017.07.007

Fehler, M. (1981). Changes in P wave velocity during operation of a hot dry rock geothermal system. Journal of Geophysical Research: Solid Earth, 86(B4), 2925-2928. doi:10.1029/JB086iB04p02925

Fei, Y. (1995). Thermal Expansion. In T. J. Ahrens (Ed.), Mineral Physics and Crystallography: A Handbook of Physical Constants (Vol. 2, pp. 29-44). Washington, D.C.: AGU.

Feng, G., Kang, Y., & Wang, X. C. (2019). Fracture failure of granite after varied durations of thermal treatment: an experimental study. Royal Society open science, 6. doi:10.1098/rsos.190144

Feng, G., Wang, X.-c., Kang, Y., Luo, S.-g., & Hu, Y.-q. (2019). Effects of Temperature on the Relationship between Mode-I Fracture Toughness and Tensile Strength of Rock. Applied Sciences, 9(7). doi:10.3390/app9071326

Feng, H., Zhou, K., Lam, Y. C., Fang, Q., Kumar, S. B., & Wu, W. (2016). Initiation and growth of microcracks near a grain boundary precipitation in coarse-grained zones of welded materials. International Journal of Solids and Structures, 102-103, 155-162. doi:10.1016/j.ijsolstr.2016.10.008

Fredrich, J. T., Evans, B., & Wong, T.-F. (1990). Effect of grain size on brittle and semibrittle strength: Implications for micromechanical modelling of failure in compression. Journal of Geophysical Research: Solid Earth, 95(B7), 10907-10920. doi:10.1029/JB095iB07p10907

Fredrich, J. T., & Wong, T.-f. (1986). Micromechanics of thermally induced cracking in three crustal rocks. Journal of Geophysical Research: Solid Earth, 91(B12), 12743-12764. doi:10.1029/JB091iB12p12743

Friedman, M., Handin, J., & Alani, G. (1972). Fracture-surface energy of rocks. International Journal of Rock Mechanics and Mining Sciences and Geomechanics Abstracts, 9(6), 757-764. doi:10.1016/0148-9062(72)90034-4

Fusseis, F., Schrank, C., Liu, J., Karrech, A., Llana-Fúnez, S., Xiao, X., & Regenauer-Lieb, K. (2012). Pore formation during dehydration of polycrystalline gypsum observed and quantified in a time-series synchrotron radiation based X-ray micro-tomography experiment. Solid Earth Discussions, 3(2), 857-900. doi:10.5194/sed-3-857-2011

Gallagher, J. J., Friedman, M., Handin, J., & Sowers, G. M. (1974). Experimental studies relating to microfracture in sandstone. Tectonophysics, 21(3), 203-247. doi:10.1016/0040-1951(74)90053-5

Gao, F., Stead, D., & Elmo, D. (2016). Numerical simulation of microstructure of brittle rock using a grain-breakable distinct element grain-based model. Computers and Geotechnics, 78, 203-217. doi:10.1016/j.compgeo.2016.05.019

Gao, Y. F., & Bower, A. F. (2004). A simple technique for avoiding convergence problems in finite element simulations of crack nucleation and growth on cohesive interfaces. Modelling and Simulation in Materials Science and Engineering, 12(3), 453-463. doi:10.1088/0965-0393/12/3/007

Ghazvinian, E., Diederichs, M. S., & Quey, R. (2014). 3D random Voronoi grain-based models for simulation of brittle rock damage and fabric-guided micro-fracturing. Journal of Rock Mechanics and Geotechnical Engineering, 6(6), 506-521. doi:10.1016/j.jrmge.2014.09.001

Giger, S. B., Tenthorey, E., Cox, S. F., & Fitz Gerald, J. D. (2007). Permeability evolution in quartz fault gouges under hydrothermal conditions. Journal of Geophysical Research, 112(B7). doi:10.1029/2006jb004828

Götze, J. (2018). Editorial for Special Issue “Mineralogy of Quartz and Silica Minerals”. Minerals, 8.

Grelk, B., Goltermann, P., Schouenborg, B., Koch, A., & Alnaes, L. (2004). The laboratory testing of potential bowing and expansion of marble. In P. R (Ed.), Dimension stone (pp. 253-260). London: Taylor and Francis Group.

Griffith, A. A., & Taylor, G. I. (1921). VI. The phenomena of rupture and flow in solids. Philosophical Transactions of the Royal Society of London. Series A, Containing Papers of a Mathematical or Physical Character, 221(582-593), 163-198. doi:10.1098/rsta.1921.0006

Griffith, A. A., & Taylor, G. I. (1921). The phenomena of rupture and flow in solids. Philosophical Transactions of the Royal Society of London. Series A, Containing Papers of a Mathematical or Physical Character, 221(582-593), 163-198. doi:10.1098/rsta.1921.0006

Griffiths, L., Lengliné, O., Heap, M. J., Baud, P., & Schmittbuhl, J. (2018). Thermal Cracking in Westerly Granite Monitored Using Direct Wave Velocity, Coda Wave Interferometry, and

Acoustic Emissions. Journal of Geophysical Research: Solid Earth, 123(3), 2246-2261. doi:10.1002/2017JB015191

Groshong, R. H. J. (1988). Low-temperature deformation mechanisms and their interpretation. Geological Society of America Bulletin, 100(9), 1329-1360. doi:10.1130/0016-7606(1988)100<1329:LTDMAT>2.3.CO;2

Gu, Y. C., Jung, J., Yang, Q. D., & Chen, W. Q. (2015). An Inertia-Based Stabilizing Method for Quasi-Static Simulation of Unstable Crack Initiation and Propagation. Journal of Applied Mechanics, 82(10). doi:10.1115/1.4031010

Guardiola, M., Bernal, C., Martínez, R., & Cassanelli, A. (2004). The Use of an Alternative Method for Fracture Toughness Evaluation on Different Materials. Journal of Testing and Evaluation, 32, 404-411. doi:10.1520/JTE11977

Gui, Y., Bui, H. H., & Kodikara, J. (2015). An application of a cohesive fracture model combining compression, tension and shear in soft rocks. Computers and Geotechnics, 66, 142-157. doi:10.1016/j.compgeo.2015.01.018

Gulizzi, V., Rycroft, C. H., & Benedetti, I. (2018). Modelling intergranular and transgranular micro-cracking in polycrystalline materials. Computer Methods in Applied Mechanics and Engineering, 329, 168-194. doi:10.1016/j.cma.2017.10.005

Gunsallus, K. L., & Kulhawy, F. H. (1984). A comparative evaluation of rock strength measures. International Journal of Rock Mechanics and Mining Sciences & Geomechanics Abstracts, 21(5), 233-248. doi:10.1016/0148-9062(84)92680-9

Haberfield, C. M., & Johnston, I. W. (1989). Relationship between fracture toughness and tensile strength for geomaterials. Paper presented at the International Conference on Soil Mechanics and Foundation Engineering, 12th, Rio de Janiero, Brazil.

Hall, D. L., & Bodnar, R. J. (1989). Comparison of fluid inclusion decrepitation and acoustic emission profiles of Westerly granite and Sioux quartzite. Tectonophysics, 168, 283-296.

Hall, E. O. (1951). The deformation and ageing of mild steel: III discussion of results. Proceedings of the Physical Society, 64(9), 747-755.

Hall, S. A., Sanctis, F. d., & Viggiani, G. (2006). Monitoring Fracture Propagation in a Soft Rock (Neapolitan Tuff) Using Acoustic Emissions and Digital Images. Pure and Applied Geophysics, 163(10), 2171-2204. doi:10.1007/s00024-006-0117-z

Hamdi, P., Stead, D., & Elmo, D. (2015). Characterizing the influence of stress-induced microcracks on the laboratory strength and fracture development in brittle rocks using a finite-discrete element method-micro discrete fracture network FDEM-μDFN approach. Journal of Rock Mechanics and Geotechnical Engineering, 7(6), 609-625. doi:10.1016/j.jrmge.2015.07.005

Han, Z., Zhang, L., & Zhou, J. (2019). Numerical Investigation of Mineral Grain Shape Effects on Strength and Fracture Behaviors of Rock Material. Applied Sciences, 9(14), 2855. Retrieved from https://www.mdpi.com/2076-3417/9/14/2855

Hanson, J. A., Hardin, B. O., & Mahboub, K. (1994). Fracture Toughness of Compacted Cohesive Soils Using Ring Test. Journal of Geotechnical Engineering, 120(5), 872-891. doi:10.1061/(ASCE)0733-9410(1994)120:5(872)

Hartley, N. E. W., & Wilshaw, T. R. (1973). Deformation and fracture of synthetic α-quartz. Journal of Materials Science volume, 8, 265-278. doi:10.1007/BF00550676

Hatzor, Y. H., & Palchik, V. (1997). The influence of grain size and porosity on crack initiation stress and critical flaw length in dolomites. International Journal of Rock Mechanics and Mining Sciences, 34(5), 805-816. doi:10.1016/S1365-1609(96)00066-6

Haxby, W. F., & Turcotte, D. L. (1976). Stresses induced by the addition or removal of overburden and associated thermal effects. Geology, 4(3), 181-184. doi:10.1130/0091-7613(1976)4<181:SIBTAO>2.0.CO;2

Heard, H. C., & Carter, N. L. (1968). Experimentally induced 'natural' intragranular flow in quartz and quartzite. American Journal of Science, 266, 1-42. doi:10. 2475/ajs.266.1.1

Heard, H. C., & Page, L. (1982). Elastic moduli, thermal expansion, and inferred permeability of two granites to 350°C and 55 megapascals. Journal of Geophysical Research, 87(B11). doi:10.1029/JB087iB11p09340

Herwegh, M., Linckens, J., Ebert, A., Berger, A., & Brodhag, S. H. (2011). The role of second phases for controlling microstructural evolution in polymineralic rocks: A review. Journal of Structural Geology, 33(12), 1728-1750. doi:10.1016/j.jsg.2011.08.011

Heyliger, P., Ledbetter, H., & Kim, S. (2003). Elastic constants of natural quartz. Journal of the Acoustical Society of America, 114(2), 644-650. doi:10.1121/1.1593063

Hibbitt, Karlsson and Sorensen Inc.©, 2009. ABAQUS/Standard User's Manual, Version 6.9. (2009). Pawtucket, R. I.

Hibbitt, H. D., & Karlsson, B. I. (1979). Analysis of pipe whip. Retrieved from United States: http://inis.iaea.org/search/search.aspx?orig_q=RN:11538109

Hiraga, T., Nagase, T., & Akizuki, M. (1999). The structure of grain boundaries in granite-origin ultramylonite studied by high-resolution electron microscopy. Physics and Chemistry of Minerals 26, 617-623. doi:10.1007/s002690050226

Hiraga, T., Nishikawa, O., Nagase, T., & Akizuki, M. (2001). Morphology of intergranular pores and wetting angles in pelitic schists studied by transmission electron microscopy. Contributions to Mineralogy and Petrology, 141(5), 613-622. doi:10.1007/s004100100263

Hirth, G., & Tullis, J. (1989). The effects of pressure and porosity on the micromechanics of the brittle-ductile transition in quartzite. Journal of Geophysical Research, 94(B12). doi:10.1029/JB094iB12p17825

Hirth, G., & Tullis, J. (1991). The effect of porosity on the strength of quartz aggregates experimentally deformed in the dislocation creep regime. Tectonophysics, 200(1-3), 97-110. doi:10.1016/0040-1951(91)90008-G

Hofmann, H., Babadagli, T., & Zimmermann, G. (2015). A grain based modeling study of fracture branching during compression tests in granites. International Journal of Rock Mechanics and Mining Sciences, 77, 152-162. doi:10.1016/j.ijrmms.2015.04.008

Homand-Etienne, F., & Houpert, R. (1989). Thermally induced microcracking in granites: characterization and analysis. International Journal of Rock Mechanics and Mining Sciences & Geomechanics Abstracts, 26(2), 125-134. doi:10.1016/0148-9062(89)90001-6

Houseknecht, D. W. (1984). Influence of grain size and temperature on intergranular pressure solution, quartz cementation, and porosity in a quartzose sandstone. Journal of Sedimentary Research, 54(2), 348-361. doi:10.1306/212f8418-2b24-11d7-8648000102c1865d

Hutchinson, J. W. (1968). Singular behaviour at the end of a tensile crack in a hardening material. Journal of the Mechanics and Physics of Solids 16(1), 13-31. doi:10.1016/0022-5096(68)90014-8.

Isaka, B., Gamage, R., Rathnaweera, T., Perera, M., Chandrasekharam, D., & Kumari, W. (2018). An Influence of Thermally-Induced Micro-Cracking under Cooling Treatments: Mechanical Characteristics of Australian Granite. Energies, 11(6), 1338. doi:10.3390/en11061338

Jansen, D. P., Carlson, S. R., Young, R. P., & Hutchins, D. A. (1993). Ultrasonic imaging and acoustic emission monitoring of thermally induced microcracks in Lac du Bonnet granite. Journal of Geophysical Research: Solid Earth, 98(B12), 22231-22243. doi:10.1029/93jb01816

Jaumann, G. (1911). Geschlossenes System physikalischer und chemischer Differential- Gesetze, Sitzungsberichte der Akademie der Wissenschaften Wien. Abteilung 1(120), 385-530.

Jin, P., Hu, Y., Shao, J., Zhao, G., Zhu, X., & Li, C. (2019). Influence of different thermal cycling treatments on the physical, mechanical and transport properties of granite. Geothermics, 78, 118-128. doi:10.1016/j.geothermics.2018.12.008

Johnson, B., Gangi, A. F., & Handin, J. (1978). Thermal Cracking Of Rock Subjected To Slow, Uniform Temperature Changes.

Kanaori, Y., Yairi, K., & Ishida, T. (1991). Grain boundary microcracking of granitic rocks from the northeastern region of the Atotsugawa fault, central Japan: SEM back scattered electron images Engineering Geology, 30(2), 221-235. doi:10. 1016/0013-7952(91)90044-L

Karaca, Z., Hacımustafaoğlu, R., & Gökçe, M. V. (2015). Grain properties, grain-boundary interactions and their effects on the characteristics of marbles used as building stones. Construction and Building Materials, 93, 166-171. doi:10.1016/j.conbuildmat.2015.05.023

Khan, K., & Al-Shayea, N. A. (2000). Effect of Specimen Geometry and Testing Method on Mixed Mode I–II Fracture Toughness of a Limestone Rock from Saudi Arabia. Rock Mechanics and Rock Engineering, 33, 179–206. doi:10.1007/s006030070006

Kohyama, M. (2002). Computational studies of grain boundaries in covalent materials. Modelling and Simulation in Materials Science and Engineering, 10(3), R31-R59. doi:10.1088/0965-0393/10/3/202

Kolo, I., Abu Al-Rub, R. K., & Sousa, R. L. (2016). Computational Modelling of Fracture Propagation in Rocks Using a Coupled Elastic-Plasticity-Damage Model. Mathematical Problems in Engineering, 2016, 1-15. doi:10.1155/2016/3231092

Kong, M., Bhattacharya, R. N., James, C., & Basu, A. (2005). A statistical approach to estimate the 3D size distribution of spheres from 2D size distributions. Geological Society of America Bulletin, 117(1-2), 244-249. doi:10.1130/B25000.1

Korenaga, J. (2007). Thermal cracking and the deep hydration of oceanic lithosphere: A key to the generation of plate tectonics? Journal of Geophysical Research, 112(B5). doi:10.1029/2006jb004502

Kranz, R. L. (1979). Crack-Crack and Crack-Pore Interactions in Stressed Granite International Journal of Rock Mechanics and Mining Sciences & Geomechanics Abstracts, 16(1), 37-47. doi:10.1016/0148-9062(79)90773-3

Kranz, R. L. (1983). Microcracks in rocks: A review Tectonophysics 100(1-3), 449-480. doi:10.1016/0040-1951(83)90198-1

Kronenberg, A. K., & Tullis, J. (1984). Flow strengths of quartz aggregates: Grain size and pressure effects due to hydrolytic weakening. Journal of Geophysical Research: Solid Earth, 89(B6), 4281-4297. doi:10.1029/JB089iB06p04281

Kruhl, J. H., Wirth, R., & Morales, L. F. G. (2013). Quartz grain boundaries as fluid pathways in metamorphic rocks. Journal of Geophysical Research: Solid Earth, 118(5), 1957-1967. doi:10.1002/jgrb.50099

Kumari, W. G. P., Ranjith, P. G., Perera, M. S. A., Chen, B. K., & Abdulagatov, I. M. (2017). Temperature-dependent mechanical behaviour of Australian Strathbogie granite with different cooling treatments. Engineering Geology, 229, 31-44. doi:10.1016/j.enggeo.2017.09.012

Lan, H., Martin, C. D., & Hu, B. (2010). Effect of heterogeneity of brittle rock on micromechanical extensile behavior during compression loading. Journal of Geophysical Research: Solid Earth, 115(B1). doi:10.1029/2009JB006496

Lan, H., Martin, C. D., Qi, S., & Li, T. (2013). A 3D grain based model for characterizing the geometric heterogeneity of brittle rock. Paper presented at the 47th US Rock Mechanics / Geomechanics Symposium, San Francisco, CA, USA.

Li, J., Kaunda, R. B., Arora, S., Hartlieb, P., & Nelson, P. P. (2019). Fully-coupled simulations of thermally-induced cracking in pegmatite due to microwave irradiation. Journal of Rock Mechanics and Geotechnical Engineering, 11(2), 242-250. doi:10.1016/j.jrmge.2018.12.007

Li, J., Konietzky, H., & Frühwirt, T. (2017). Voronoi-Based DEM Simulation Approach for Sandstone Considering Grain Structure and Pore Size. Rock Mechanics and Rock Engineering, 50, 2749-2761. doi:10.1007/s00603-017-1257-4

Li, X. F., Li, H. B., & Zhao, J. (2017). 3D polycrystalline discrete element method (3PDEM) for simulation of crack initiation and propagation in granular rock. Computers and Geotechnics, 90, 96-112. doi:10.1016/j.compgeo.2017.05.023

Liu, G., Cai, M., & Huang, M. (2018). Mechanical properties of brittle rock governed by micro-geometric heterogeneity. Computers and Geotechnics, 104, 358-372. doi:10.1016/j.compgeo.2017.11.013

Liu, P. F., & Zheng, J. Y. (2010). Recent developments on damage modeling and finite element analysis for composite laminates: A review. Materials & Design, 31(8), 3825-3834. doi:10.1016/j.matdes.2010.03.031

Mancktelow, N. S., & Pennacchioni, G. (2004). The influence of grain boundary fluids on the microstructure of quartz-feldspar mylonites. Journal of Structural Geology, 26(1), 47-69. doi:10.1016/s0191-8141(03)00081-6

Meredith, P., Daoud, A., Browning, J., & Mitchell, T. (2019). Microstructural controls on thermal crack damage during temperature-cycling experiments on volcanic rocks. Paper presented at the 21st EGU General Assembly, Vienna, Austria.

Meredith, P. G., Knight, K. S., Boon, S. A., & Wood, I. G. (2001). The microscopic origin of thermal cracking in rocks: An investigation by simultaneous time-of-flight neutron diffraction and acoustic emission monitoring. Geophysical Research Letters, 28(10), 2105-2108. doi:10.1029/2000GL012470

Meyers, D. E., & Ardell, A. J. (1993). Mechanical properties of individual grain boundaries in Ni3Al using a miniaturized disk-bend test Acta Metallurgica et Materialia 41(9), 2601-2610. doi:10.1016/0956-7151(93)90129-G

Mikhailovskij, I. M., Mazilova, T. I., Voyevodin, V. N., & Mazilov, A. A. (2011). Inherent strength of grain boundaries in tungsten. Physical Review B, 83(13). doi:10.1103/PhysRevB.83.134115

Möller, J. J., & Bitzek, E. (2014). Fracture toughness and bond trapping of grain boundary cracks. Acta Materialia, 73, 1-11. doi:10.1016/j.actamat.2014.03.035

Mueller, M. G., Pejchal, V., Žagar, G., Singh, A., Cantoni, M., & Mortensen, A. (2015). Fracture toughness testing of nanocrystalline alumina and fused quartz using chevron-notched microbeams. Acta Materialia, 86, 385-395. doi:10.1016/j.actamat.2014.12.016

Müller, C., Frühwirt, T., Haase, D., Schlegel, R., & Konietzky, H. (2018). Modeling deformation and damage of rock salt using the discrete element method. International Journal of Rock Mechanics and Mining Sciences, 103, 230-241. doi:10.1016/j.ijrmms.2018.01.022

Nålsund, R., & Jensen, V. (2013). INFLUENCE OF MINERAL GRAIN SIZE, GRAIN SIZE DISTRIBUTION AND MICRO-CRACKS ON ROCKS' MECHANICAL STRENGTH. Paper presented at the 14th Euroseminar on Microscopy Applied to Building Materials, Helsingør, Denmark.

Nasseri, M. H. B., & Mohanty, B. (2008). Fracture toughness anisotropy in granitic rocks. International Journal of Rock Mechanics and Mining Sciences, 45(2), 167-193. doi:10.1016/j.ijrmms.2007.04.005

Nasseri, M. H. B., Mohanty, B., & Young, R. P. (2006). Fracture Toughness Measurements and Acoustic Emission Activity in Brittle Rocks. Pure and Applied Geophysics, 163(5-6), 917-945. doi:10.1007/s00024-006-0064-8

Nasseri, M. H. B., Schubnel, A., Benson, P. M., & Young, R. P. (2009b). Common Evolution of Mechanical and Transport Properties in Thermally Cracked Westerly Granite at Elevated Hydrostatic Pressure. Pure and Applied Geophysics, 166(5-7), 927-948. doi:10.1007/s00024-009-0485-2

Nasseri, M. H. B., Schubnel, A., & Young, R. P. (2007). Coupled evolutions of fracture toughness and elastic wave velocities at high crack density in thermally treated Westerly granite. International Journal of Rock Mechanics and Mining Sciences, 44(4), 601-616. doi:10.1016/j.ijrmms.2006.09.008

Nasseri, M. H. B., Tatone, B. S. A., Grasselli, G., & Young, R. P. (2009a). Fracture Toughness and Fracture Roughness Interrelationship in Thermally treated Westerly Granite. Pure and Applied Geophysics, 166(5-7), 801-822. doi:10.1007/s00024-009-0476-3

Needleman, A. (1988). Material rate dependence and mesh sensitivity in localization problems. Computer Methods in Applied Mechanics and Engineering, 67(1), 69-85. doi:10.1016/0045-7825(88)90069-2

Nicksiar, M., & Martin, C. D. (2014). Factors Affecting Crack Initiation in Low Porosity Crystalline Rocks. Rock Mechanics and Rock Engineering, 47(4), 1165-1181. doi:10.1007/s00603-013-0451-2

Nicolas, A., & Poirier, J. P. (1976). Crystalline plasticity and solid-state flow in metamorphic rocks. London, New York: Wiley.

Nordlund, E., Li, C., & Carlsson, B. (1999). Mechanical properties of the diorite in the prototype repository at Äspö. HRL-laboratory tests. International Progress Report, IPR-99-25, SKB.

Nur, A., & Simmons, G. (1970). The origin of small cracks in igneous rocks. International Journal of Rock Mechanics and Mining Sciences & Geomechanics Abstracts, 7, 307-314.

Ogolo, N. A., Akinboro, O. G., Inam, J. E., Akpokere, F. E., & Onyekonwu, M. O. (2015). Effect of Grain Size on Porosity Revisited. Paper presented at the SPE Nigeria Annual International Conference and Exhibition, Lagos, Nigeria. https://doi.org/10.2118/178296-MS

Olsson, W. A. (1974). Grain size dependence of yield stress in marble. Journal of Geophysical Research 79(32), 4859-4862. doi:10.1029/JB079i032p04859

Parks, G. A. (1984). Surface and interfacial free energies of quartz. Journal of Geophysical Research: Solid Earth, 89(B6), 3997-4008. doi:10.1029/JB089iB06p03997

Passchier, C. W., & Trouw, R. A. J. (2005). Microtectonics (2nd ed.). Berlin, Heidelberg, Germany: Springer.

Paterson, M. (2001). Relating experimental and geological rheology. International Journal of Earth Sciences, 90(1), 157-167. doi:10.1007/s005310000158

Pearson, C. F., Fehler, M. C., & Albright, J. N. (1983). Changes in compressional and shear wave velocities and dynamic moduli during operation of a hot dry rock geothermal system. Journal of Geophysical Research: Solid Earth, 88(B4), 3468-3475. doi:10.1029/JB088iB04p03468

Peck, L., & Gordon, R. B. (1982). The effect of compressive stress on the fracture energy of Sioux quartzite. geophysical research Letters, 9(3), 186-189. doi:10.1029/GL009i003p00186

Peng, J., Wong, L. N. Y., & Teh, C. I. (2017a). Influence of grain size heterogeneity on strength and microcracking behavior of crystalline rocks. Journal of Geophysical Research: Solid Earth, 122(2), 1054-1073. doi:10.1002/2016jb013469

Peng, J., Wong, L. N. Y., & Teh, C. I. (2017b). Effects of grain size-to-particle size ratio on micro-cracking behavior using a bonded-particle grain-based model. International Journal of Rock Mechanics and Mining Sciences, 100, 207-217. doi:10.1016/j.ijrmms.2017.10.004

Petch, N. J. (1953). The cleavage strength of polycrystals. The Journal of the Iron and Steel Institute, 174(1), 25-28.

Picu, C. R., & Gupta, V. (1997). Three-dimensional stress singularities at the tip of a grain triple junction line intersecting the free surface. Journal of the Mechanics and Physics of Solids, 45(9), 1495-1520. doi:10.1016/S0022-5096(97)00014-8

Pimienta, L., Klitzsch, N., & Clauser, C. (2018). Comparison of thermal and elastic properties of sandstones: Experiments and theoretical insights. Geothermics, 76, 60-73. doi:10.1016/j.geothermics.2018.06.005

Quey, R. (2020). Neper Reference Manual, version 3.5.2(pp. 110). Retrieved from http://neper.sourceforge.net

Quey, R., Dawson, P. R., & Barbe, F. (2011). Large-scale 3D random polycrystals for the finite element method: Generation, meshing and remeshing. Computer Methods in Applied Mechanics and Engineering, 200(17-20), 1729-1745. doi:10.1016/j.cma.2011.01.002

Raghami, E., Schrank, C., & Kruhl, J. H. (2020). 3D modelling of the effect of thermal-elastic stress on grain-boundary opening in quartz grain aggregates. Tectonophysics, 774, 228242. doi:10.1016/j.tecto.2019.228242

Raghami, E., Schrank, C., & Kruhl, J. H. (2021). An alternative approach to studying exhumation-induced grain-boundary openings in quartz grain aggregates: 3D modeling. In preparation.

Regenauer-Lieb, K., Karrech, A., Chua, H. T., Poulet, T., Veveakis, M., Wellmann, F., . . . Lester, D. (2014). Entropic Bounds for Multi-Scale and Multi-Physics Coupling in Earth Sciences. In R. C. Dewar, C. H. Lineweaver, R. K. Niven, & K. Regenauer-Lieb (Eds.), Beyond the second law (pp. 323-335.). Berlin, Heidelberg: Springer.

Regenauer-Lieb, K., & Yuen, D. (2004). Positive feedback of interacting ductile faults from coupling of equation of state, rheology and thermal-mechanics. Physics of the Earth and Planetary Interiors, 142(1-2), 113-135. doi:10.1016/j.pepi.2004.01.003

Regenauer-Lieb, K., & Yuen, D. A. (2003). Modeling shear zones in geological and planetary sciences: solid- and fluid-thermal–mechanical approaches. Earth-Science Reviews, 63(3), 295-349. doi:10.1016/S0012-8252(03)00038-2

Richter, D., & Simmons, G. (1974). Thermal expansion behavior of igneous rocks. International Journal of Rock Mechanics and Mining Sciences & Geomechanics Abstracts, 11(10), 403-411. doi:10.1016/0148-9062(74)91111-5

Riks, E. (1979). An incremental approach to the solution of snapping and buckling problems. International Journal of Solids and Structures, 15(7), 529-551. doi:10.1016/0020-7683(79)90081-7

Ronchin, E., Masterlark, T., Molist, J. M., Saunders, S., & Tao, W. (2013). Solid modeling techniques to build 3D finite element models of volcanic systems: An example from the Rabaul Caldera system, Papua New Guinea. Computers & Geosciences, 52, 325-333. doi:10.1016/j.cageo.2012.09.025

Rong, G., Peng, J., Cai, M., Yao, M., Zhou, C., & Sha, S. (2018). Experimental investigation of thermal cycling effect on physical and mechanical properties of bedrocks in geothermal fields. Applied Thermal Engineering, 141, 174-185. doi:10.1016/j.applthermaleng.2018.05.126

Rosenfeld, J. L., & Chase, A. B. (1961). Pressure and temperature of crystallization from elastic effects around solid inclusions in minerals? American Journal of Science, 259(7), 519-541. doi:10.2475/ajs.259.7.519

Rosengren, K. J., & Jaeger, J. C. (1968). The Mechanical Properties of an Interlocked Low-Porosity Aggregate. Géotechnique 18(3), 317-326. doi:10.1680/geot. 1968.18.3.317

Saadat, M., & Taheri, A. (2019). A numerical approach to investigate the effects of rock texture on the damage and crack propagation of a pre-cracked granite. Computers and Geotechnics, 111, 89-111. doi:10.1016/j.compgeo.2019.03.009

Savanick, G. A., & Johnson, D. I. (1974). Measurements of the strength of grain boundaries in rock International Journal of Rock Mechanics and Mining Sciences, 11(5), 173-180. doi:10.1016/0148-9062(74)90884-5

Sayers, C. M., & Kachanov, M. (1995). Microcrack-induced elastic wave anisotropy of brittle rocks. Journal of Geophysical Research: Solid Earth, 100(B3), 4149-4156. doi:10.1029/94jb03134

Schrank, C. E., Fusseis, F., Karrech, A., & Regenauer-Lieb, K. (2012). Thermal-elastic stresses and the criticality of the continental crust. Geochemistry, Geophysics, Geosystems, 13(9). doi:10.1029/2012gc004085

Schrank, C. E., Gioseffi, K., Blach, T., Gaede, O., Hawley, A., Milsch, H., . . . Radlinski, A. P. (2019). Tracking metamorphic dehydration reactions in real time with transmission small- and wide-angle synchrotron X-ray scattering: the case of gypsum dehydration. Journal of Petrology. doi:10.1093/petrology/egaa041

Shewmon, P., & Anderson, P. (1998). Void nucleation and cracking at grain boundaries. Acta Materialia, 46(14), 4861-4872. doi:10.1016/S1359-6454(98)00194-3

Shushakova, V., Fuller, E. R., & Siegesmund, S. (2011). Influence of shape fabric and crystal texture on marble degradation phenomena: simulations. Environmental Earth Sciences, 63(7), 1587-1601. doi:10.1007/s12665-010-0744-7

Shushakova, V., Fuller, E. R., & Siegesmund, S. (2013). Microcracking in calcite and dolomite marble: microstructural influences and effects on properties. Environmental Earth Sciences, 69(4), 1263-1279. doi:10.1007/s12665-012-1995-2

Siegesmund, S., Ullemeyer, K., Weiss, T., & Tschegg, E. K. (2000). Physical weathering of marbles caused by anisotropic thermal expansion. International Journal of Earth Sciences, 89(1), 170-182. doi:10.1007/s005310050324

Simmons, G., & Cooper, H. W. (1978). Thermal cycling cracks in three igneous rocks International Journal of Rock Mechanics, Mineral Science and Geomechanics abstract, 15(4), 145-148. doi:10.1016/0148-9062(78)91220-2

Simpson, D. R., & Fergus Jr., J. H. (1968). The effect of water on the compressive strength of diabase. Journal of Geophysical Research, 73(20), 6591-6594. doi:10.1029/JB073i020p06591

Skinner, B. J. (1966). Thermal expansion. In S. P. J. Clark (Ed.), Handbook of physical constants (pp. 75-96). Boulder, Colorado: Geological Society of America.

Stanchits, S., Vinciguerra, S., & Dresen, G. (2006). Ultrasonic Velocities, Acoustic Emission Characteristics and Crack Damage of Basalt and Granite. Pure and Applied Geophysics, 163(5-6), 975-994. doi:10.1007/s00024-006-0059-5

Stipp, M., Stünitz, H., Heilbronner, R., & Schmid, S. M. (2002). The eastern Tonale fault zone: A 'natural laboratory' for crystal plastic deformation of quartz over a temperature range from 250 to 700 °C. Structural Geology, 24(12), 1861-1884. doi:10.1016/S0191-8141(02)00035-4

Stöckhert, B., Brix, M. R., Kleinschrodt, R., Hurford, A. J., & Wirth, R. (1999). Thermochronometry and microstructures of quartz-a comparison with experimental flow laws and predictions on the temperature of the brittle-plastic transition. Journal of Structural Geology 21(3), 351-369. doi:10.1016/S0191-8141(98)00114-X

Stretton, I. (1996). An experimental investigation of the deformation properties of gypsum. University of Manchester, United Kingdom.

Tada, R., & Siever, R. (1989). Pressure Solution During Diagenesis. Annual Review of Earth and Planetary Sciences, 17(1), 89-118. doi:10.1146/annurev.ea.17.050189.000513

Tang, C. A., Liu, H., Lee, P. K. K., Tsui, Y., & Tham, L. G. (2000). Numerical studies of the influence of microstructure on rock failure in uniaxial compression — Part I: effect of heterogeneity. International Journal of Rock Mechanics and Mining Sciences, 37(4), 555-569. doi:10.1016/S1365-1609(99)00121-5

Tang, S. B., Zhang, H., Tang, C. A., & Liu, H. Y. (2016). Numerical model for the cracking behavior of heterogeneous brittle solids subjected to thermal shock. International Journal of Solids and Structures, 80, 520-531. doi:10.1016/j.ijsolstr.2015.10.012

Tapponnier, P., & Brace, W. F. (1976). Development of stress-induced microcracks in Westerly Granite. International Journal of Rock Mechanics and Mining Sciences & Geomechanics Abstracts, 13(4), 103-112. doi:10.1016/0148-9062(76)91937-9

Thompson, B. D., Young, R. P., & Lockner, D. A. (2009). Premonitory acoustic emissions and stick-slip in natural and smooth-faulted Westerly granite. Journal of Geophysical Research B: Solid Earth, 114(B2), 1-14. doi:10.1029/2008jb005753

Tomac, I., & Gutierrez, M. (2017). Coupled hydro-thermo-mechanical modeling of hydraulic fracturing in quasi-brittle rocks using BPM-DEM. Journal of Rock Mechanics and Geotechnical Engineering, 9(1), 92-104. doi:10.1016/j.jrmge.2016.10.001

Tromans, D., & Meech, J. A. (2004). Fracture toughness and surface energies of covalent minerals: theoretical estimates. Minerals Engineering, 17(1), 1-15. doi:10.1016/j.mineng.2003.09.006

Turcotte, D. L., & Oxburgh, E. R. (1976). Stress accumulation in the lithosphere. Tectonophysics, 35(1-3), 183-199. doi:10.1016/0040-1951(76) 90037-8

Valiev, R. Z., Gertsman, V. Y., & Kaibyshev, O. A. (1986). Grain boundary structure and properties under external influences. physica status solidi (a), 97, 11-56. doi:10.1002/pssa.2210970102

Vasarhelyi, B., & Van, P. (2006). Influence of water content on the strength of rock. Engineering Geology, 84, 70-74.

Vázquez, P., Shushakova, V., & Gómez-Heras, M. (2015). Influence of mineralogy on granite decay induced by temperature increase: Experimental observations and stress simulation. Engineering Geology, 189, 58-67. doi:10.1016/j.enggeo.2015.01.026

Vernon, R. H. (2004). A Practical Guide to Rock Microstructure. Cambridge: Cambridge University Press.

Voll, G. (1976). Recrystallization of quartz, biotite and feldspars from Erstfeld to the Leventina Nappe, Swiss Alps, and its geological significance. Schweiz. Schweizerische mineralogische und petrographische Mitteilungen = Bulletin suisse de minéralogie et petrographie, 56(3), 641-647. doi:10.5169/seals-43709.

Walsh, J. B. (1973). Theoretical bounds for thermal expansion, specific heat, and strain energy due to internal stress. Journal of Geophysical Research, 78(32), 7637-7646. doi:10.1029/JB078i032p07637

Wang, H. F., Bonner, B. P., Carlson, S. R., Kowallis, B. J., & Heard, H. C. (1989). Thermal stress cracking in granite. Journal of Geophysical Research, 94(B2). doi:10.1029/JB094iB02p01745

Wang, J. S. Y., Tsang, C. F., Cook, N. G. W., & Witherspoon, P. A. (1981). A study of regional temperature and thermohydrologic effects of an underground repository for nuclear wastes in

hard rock. Journal of Geophysical Research: Solid Earth, 86(B5), 3759-3770. doi:10.1029/JB086iB05p03759

Wang, Q., Huang, J., Wang, Z., He, G., Lei, D., Gong, J., & Wu, L. (2018). Anisotropic Three-Dimensional Thermal Stress Modeling and Simulation of Homoepitaxial AlN Single Crystal Growth by the Physical Vapor Transport Method. Crystal Growth & Design, 18(5), 2998-3007. doi:10.1021/acs.cgd.8b00118

Wang, W. M., Sluys, L. J., & de Borst, R. (1997). Viscoplasticity for instabilities due to strain softening and strain-rate softening. International Journal for Numerical Methods in Engineering, 40(20), 3839-3864. doi:10.1002/(sici)1097-0207(19971030)40:20<3839::Aid-nme245>3.0.Co;2-6

Wang, X.-e., Yang, J., Liu, Q.-f., Zhang, Y.-m., & Zhao, C. (2017). A comparative study of numerical modelling techniques for the fracture of brittle materials with specific reference to glass. Engineering Structures, 152, 493-505. doi:10.1016/j.engstruct.2017.08.050

Watkins, T. L., Hetherington, C. J., Annasiwatta, C., & Berg, J. M. (2012). Thermal conductivity in deformed quartzites: the role of mineral preferred orientation. https://ui.adsabs.harvard.edu/abs/2012AGUFMED23B0763W

Weiss, T., Siegesmund, S., & Fuller, E. R. (2003). Thermal degradation of marble: indications from finite-element modelling. Building and Environment, 38(9-10), 1251-1260. doi:10.1016/s0360-1323(03)00082-9

Weng, L., Wu, Z., & Liu, Q. (2019). Influence of heating/cooling cycles on the micro/macrocracking characteristics of Rucheng granite under unconfined compression. Bulletin of Engineering Geology and the Environment, 79, 1289-1309. doi:10.1007/s10064-019-01638-4

White, J. C., & White, S. H. (1981). On the structure of grain boundaries in tectonites. Tectonophysics, 78(1), 613-628. doi:10.1016/0040-1951(81)90032-9

Whitney, D. L., Broz, M., & Cook, R. F. (2007). Hardness, toughness, and modulus of some common metamorphic minerals. American Mineralogist, 92, 281-288. doi:10.2138/am.2007.2212

Whittaker, B. N., Singh, R. N., & Sun, G. (1992). Rock fracture mechanics: principles, design, and applications: Elsevier.

Wirth, R., Kruhl, J. H., Morales, L. F. G., & Schreiber, A. (2020). Partially open grain and phase boundaries as fluid pathways in magmatic and metamorphic rocks. Metamorphic Geology.

Wong, L., Maruvanchery, V., & Liu, G. (2016). Water effects on rock strength and stiffness degradation. Acta Geotechnica, 11, 713-737.

Wong, R. H. C., Chau, K. T., & Wang, P. (1996). Microcracking and grain size effect in Yuen Long marbles. International Journal of Rock Mechanics and Mining Sciences & Geomechanics Abstracts, 33(5), 479-485. doi:10.1016/0148-9062(96)00007-1

Wood, M. M., & Weidlich, J. E. (1982). Empirical evaluation of fracture toughness: the toughness of quartz. American Mineralogist, 67(9-10), 1065-1068.

Wu, Q., Weng, L., Zhao, Y., Guo, B., & Luo, T. (2019). On the tensile mechanical characteristics of fine-grained granite after heating/cooling treatments with different cooling rates. Engineering Geology, 253, 94-110. doi:10.1016/j.enggeo.2019.03.014

Yoon, Y.-G., Car, R., Srolovitz, D. J., & Scandolo, S. (2004). Thermal conductivity of crystalline quartz from classical simulations. Physical Review B, 70(1). doi:10.1103/PhysRevB.70.012302

Yu, H., Olsen, J. S., Olden, V., Alvaro, A., He, J., & Zhang, Z. (2016). Viscous regularization for cohesive zone modeling under constant displacement: An application to hydrogen embrittlement simulation. Engineering Fracture Mechanics, 166, 23-42. doi:10.1016/j.engfracmech.2016.08.019

Yu, Q., Zhu, W., Ranjith, P. G., & Shao, S. (2018). Numerical simulation and interpretation of the grain size effect on rock strength. Geomechanics and Geophysics for Geo-Energy and Geo-Resources, 4(2), 157-173. doi:10.1007/s40948-018-0080-z

Yu, Q. L., Ranjith, P. G., Liu, H. Y., Yang, T. H., Tang, S. B., Tang, C. A., & Yang, S. Q. (2015). A Mesostructure-based Damage Model for Thermal Cracking Analysis and Application in Granite at Elevated Temperatures. Rock Mechanics and Rock Engineering, 48(6), 2263-2282. doi:10.1007/s00603-014-0679-5

Zhang, F., Zhao, J., Hu, D., Skoczylas, F., & Shao, J. (2018). Laboratory Investigation on Physical and Mechanical Properties of Granite After Heating and Water-Cooling Treatment. Rock Mechanics and Rock Engineering, 51(3), 677-694. doi:10.1007/s00603-017-1350-8

Zhang, Z. X. (2002). An empirical relation between mode I fracture toughness and the tensile strength of rock. International Journal of Rock Mechanics and Mining Sciences, 39(3), 401-406. doi:10.1016/s1365-1609(02)00032-1

Zhang, Z. X., Kou, S. Q., Lindqvist, P. A., & Yu, Y. (1998). Relationship Between the Fracture Toughness and Tensile Strength of Rock. Paper presented at the Strength theories: applications, development & prospects for 21st century, Beijing/NewYork.

Zhu, D., Jing, H., Yin, Q., Ding, S., & Zhang, J. (2019a). Mechanical Characteristics of Granite After Heating and Water-Cooling Cycles. Rock Mechanics and Rock Engineering. doi:10.1007/s00603-019-01991-6

Zhu, Z., Tian, H., Chen, J., Jiang, G., Dou, B., Xiao, P., & Mei, G. (2019b). Experimental investigation of thermal cycling effect on physical and mechanical properties of heated granite after water cooling. Bulletin of Engineering Geology and the Environment. doi:10.1007/s10064-019-01705-w

Zimmerman, R. W. (1985). The effect of microcracks on the elastic moduli of brittle materials. Journal of Materials Science Letters, 4(12), 1457-1460. doi:10.1007/bf00721363

Acknowledgments

I highly acknowledge my supervisory team Prof. Dr Jörn Kruhl and Dr. Christoph Schrank for their trust, patience, guidance and mentoring. Thank you! You are both remarkable as scientists. I have been extremely lucky to work with Dr. Christoph Schrank, from whom I learned a lot. His immense knowledge, motivation and patience have given me more power and spirit to continue this difficult and complicated topic.

Besides my supervisors, my sincere thanks also go to Prof. Dr. Wolfgang Schmahl, who gave me encouragements, insightful suggestions and endless guidance.

Thank you so much Dr. Maryam Azarnoosh (my mum) for your 24 hours guidance and support.

I would like to thank the German Research Foundation (DFG) [grant number KR691/36-1 / SCHM930/17-1] for financial support for this project and High-Performance Computing Centre (HPC) of Queensland University of Technology (QUT) for access to computational facilities and valuable software support.

I am also pleased to say thank you to Prof. Dr. Soraya Heuss-Aßbichler for her kind help and sharing her experiences in many aspects.

I would like to thank to my colleagues, Mrs. Karin Kleinstück and Mrs. Barbara Jaeger for their support during this time.

I would also like to thank to my best friend in Australia, Marjory cooper Davie and my friends at LMU, Martina Greiner and Maria Simonet for their positive energy and encouragement when I was disappointed.

Finally, and most importantly, I would like to express my special thanks to my family. I consider myself nothing without them. They gave me enough moral support, encouragement and motivation to accomplish the personal goals. This dissertation would not have been possible without their warm love, continued patience, and endless support.

In particular, I will give my deepest gratitude to my husband for his unconditional and constant support and love during my work on the thesis.

List of Peer-Reviewed Publications

Raghami, E., Schrank, C., & Kruhl, J. H. (2020). 3D modeling of the effect of thermal-elastic stress on grain-boundary opening in quartz grain aggregates. Tectonophysics, 774, 228242. doi:10.1016/j.tecto.2019.228242.

Raghami, E., Schrank, C., & Kruhl, J. H. An alternative approach to studying exhumation-induced grain-boundary openings in quartz grain aggregates: 3D modeling. (Ready to submission)

Raghami, E., Schrank, C., & Kruhl, J. H. Numerical analysis of the effect of grain size on exhumation-induced grain-boundary cracking in quartz grain aggregates. (In preparation)

Conference Contributions

Oral Presentations

"Grain and phase boundaries in rocks of the upper crust and at the earth's surface". **Raghami, E.**, Schrank, C., & Kruhl, J. H.
GeoMünster, Münster / Germany, 2019.

"Opening of quartz grain boundaries during cooling and decompression: 3D modelling."
Raghami, E., Schrank, C., & Kruhl, J. H.
22nd International Conference on Deformation Mechanisms, Rheology and Tectonics, Tübingen, Germany, 2019.

"3D modelling of the effect of thermal-elastic stress on grain-boundary opening in quartz grain aggregates".
Raghami, E., Schrank, C., & Kruhl, J. H.
GeoBonn Conference, Bonn, Germany, 2018.